Pericontusional Ischaemia Following Head Injury: Imaging Correlates

Peter Graham Bradley

University of London

This dissertation is submitted for the degree of Doctor of Medicine (M.D.)

ProQuest LLC
789 East Eisenhower Parkway
P.O. Box 1346
Ann Arbor, MI 48106-1346

ABSTRACT

It has been well established that ischaemia can result in secondary injury to the brain following trauma. While such ischaemia has been imaged, it has been difficult demonstrate its physiological significance.

The aim of this research was to use diffusion weighted magnetic resonance imaging (DWI) to characterise the patterns of cytotoxic and vasogenic oedema early after head injury and correlate changes with regional physiology, imaged using ^{15}O positron emission tomography (^{15}O-PET).

Data from methodological developments carried out in the course of this research are presented. These include the testing of MR compatibility of infusion pumps, optimisation of image processing routines, assessment of the validity of commonly used MR measures of tissue injury in the context of head injury, and an assessment of the test-retest reproducibility of DWI.

Early DWI imaging in 30 patients with significant head injury (range 8 - 134 hours) revealed a characteristic contusional morphology, with a haemorrhagic core and concentric rings of vasogenic and cytotoxic oedema. In the regions studied, the integrated volume of pericontusional oedema was over three times the volume of the central core. An analysis across patients, although confounded by interindividual variation, suggested that this pericontusional oedema increased in size with time from injury. Correlation with electron microscopy suggested microvascular ischaemia as a mechanism for these changes

The physiological correlates of the ADC changes described above were investigated in a subset of nine patients with ^{15}O-PET. The contusion core showed significant reductions in cerebral blood flow (CBF), oxygen extraction fraction (OEF) and cerebral oxygen metabolism (CMRO2), while the region of vasogenic oedema only showed significantly reductions in CMRO2. Other studies explored the use of dynamic DWI to assess the impact of hyperventilation on ADC changes around contusions.

The implications of these findings are discussed and further research directions explored.

ACKNOWLEDGEMENTS

Most importantly I would like to thank the patients and relatives who kindly agreed to participate in this research. Their consent to these studies was given at a time of great personal upset and this work is dedicated to them.

I would like to thank my supervisors: Professor David Menon from the University of Cambridge and Dr. Martin Smith from the University of London. I am very grateful for their expert advice and patience which has enabled me to complete this research.

I would also like to thank my colleagues in the University Division of Anaesthesia and the Wolfson Brain Imaging Centre for their help and support in this research. In particular Sally Harding, Dot Chatfield, Jonathan Coles, Jurgens Nortje, Guy Williams, Hadrian Green, Andy Johnston, Adrian Carpenter, Alonso Peña and Raymond Salvador.

Finally to Amanda, who has throughout this work sustained me with her love and tolerance I am truly grateful.

LIST OF ABBREVIATIONS

ADC	Apparent diffusion coefficient
ASL	Arterial spin labelling
CBF	Cerebral blood flow
CBV	Cerebral blood volume
CI	Confidence interval
$CMRO_2$	Cerebral metabolic rate for oxygen
CPP	Cerebral perfusion pressure
CSF	Cerebrospinal fluid
CT	X-ray computed tomography
DTI	Diffusion tensor imaging
DWI	Diffusion weighted imaging
FA	Fractional Anisotropy
FLAIR	Fluid attenuated inversion recovery
GCS	Glasgow coma scale
GOS	Glasgow outcome scale
Hb	Haemoglobin
ICP	Intracranial pressure
MAP	Mean arterial pressure
MR	Magnetic resonance
MRI	Magnetic resonance imaging
NCCU	Neurosciences critical care unit
OEF	Oxygen extraction fraction
^{15}O PET	Oxygen-15 positron emission tomography
$PaCO_2$	Arterial partial pressure of carbon dioxide
PaO_2	Arterial partial pressure of oxygen
PWI	Perfusion weighted imaging
ROI	Region of interest
SaO_2	Arterial oxygen saturation
SD	Standard deviation
SjO_2	Jugular bulb oxygen saturation
TBI	Traumatic brain injury
WBIC	Wolfson brain imaging centre
Xenon CT	Xenon enhanced computed tomography

Table of Contents

Table of Figures

1 Introduction

1.1 The Problem

1.1.1 Ischaemia After Head Injury

Every year there are around 2,500 cases of severe traumatic brain injury in the UK of these approximately one-quarter will die and another quarter will be left with severe and permanent disability. Unlike injury to many other tissues, the severity of disability is not well predicted by the volume of injured brain tissue. Damage to small areas in the brain stem or diffuse white matter tracts may lead to severe disability, while damage to a greater volume elsewhere may have little effect on function. The degree of disability is not simply a reflection of the severity or distribution of the primary injuries but also the effect of secondary injuries produced by factors including ischaemia, raised intracranial pressure, seizures, infection, brain swelling and metabolic abnormalities. Many of these secondary injuries can be minimised by timely medical and surgical interventions. The brain is particularly vulnerable to secondary injury due to ischaemia because of its high metabolic rate and limited intrinsic energy stores. Indeed, post-mortem evidence after head injury suggests that ischaemia is a frequent cause of secondary injury,[1] and it is known that secondary ischemic insults such as hypotension and hypoxia can worsen both mortality and outcome after head injury.[2 3]

1.1.2 Imaging Evidence of Ischaemia

Imaging studies have demonstrated antemortem evidence of cerebral ischaemia in humans, particularly in the first few hours after injury. Studies using Xenon CT have revealed significantly reduced cerebral blood flow (CBF) in the first few hours after head injury,[4-6] and studies using ^{15}O-PET have shown reductions in CBF after head injury, associated with high regional oxygen extraction fraction, suggesting true ischaemia rather than hypoperfusion coupled to hypometabolism.[7] Comparison of imaging findings to pericontusional ultrastructure suggests that at least a proportion of ischaemia in this setting may be the consequence of microvascular collapse due to extracellular oedema rather than simple hypoperfusion.[5 8 9] Taken together, these studies demonstrate that the brain is at high risk of ischaemic damage after head injury. However, evidence that ischemic damage has occurred is less complete. Imaging studies using diffusion weighted imaging (DWI) have reported regions of reduced diffusion around cerebral contusions, early after head injury. These findings are typical of cytotoxic oedema and therefore suggest that ischemic secondary damage has occurred.[10] [11] However, the associated physiology, the relationship to simple hypoperfusion and

microvascular dysfunction, and the reversibility of these apparent diffusion coefficient (ADC) changes are unknown.

1.1.3 Defining Ischaemia

Chamber's dictionary defines ischaemia as 'an inadequate flow of blood to a part of the body, caused by blockage or constriction of a blood vessel'. The essential part of this definition is the word inadequate. Although the simultaneous measurement of CBF can identify hypoperfusion, ischaemia can only be defined in the context of a blood flow that is inadequately low for tissue metabolism. The imaging of physiology associated with cerebral ischaemia must therefore include measurement of metabolism and CBF.

1.1.4 Imaging Options Available

The aim of this research is to characterise the patterns of cytotoxic and vasogenic oedema early after head injury, correlate these changes with physiology and structure, and explore the dynamic nature of the changes in response to therapeutic intervention. The imaging of cytotoxic and vasogenic oedema requires the use of diffusion weighted magnetic resonance imaging (DW MRI; DWI). However there are several techniques described for measuring regional CBF. These include ^{133}Xe wash out,[12] Xenon-CT,[13] MRI techniques of dynamic susceptibility contrast and arterial spin labelling,[14] and ^{15}O positron emission tomography (^{15}O-PET). Adequate characterisation of regional ischaemia requires the simultaneous measurement of both regional cerebral metabolism and cerebral blood flow, which is only possible with ^{15}O-PET.

1.2 Overview of the Thesis

This thesis is composed of nine chapters which outline the background, methods, results and conclusions of this work.

Collaborations

I was fully involved in all the studies included in this manuscript and in the overwhelming majority of the studies the work is entirely my own. However, this research was carried out in a department with an active and ongoing research interest in neurological injury often involving collaboration with other research groups, where such collaboration has occurred; I would like to describe the extent of my involvement and that of the other groups. In Chapters 4, 5, 6, 7 and 9 I was assisted in obtaining the imaging studies by a team including radiographers, radio-chemists, physicists, nurses and other researchers within our research group. However for each patient included in

the imaging studies I was directly responsible for some or all of the preparation and imaging. I was the sole researcher conducting the image processing and analysis in these studies. In Chapter 5 I was the sole individual responsible for conducting these studies however equipment and advice was obtained from collaborators in the Department of Medical Physics, Addenbrooke's Hospital, Cambridge. In Chapter 8 the electron microscopy studies were conducted Dr Martin Skepper in the Department of Anatomy I was not involved in the conduct of these EM studies. I was however involved in obtaining consent to research and tissue samples at the time of surgery in some of the patients.

Chapter 2. This chapter describes the physical principles involved in the imaging techniques of MRI, with particular emphasis on DWI, and ^{15}O-PET techniques

Chapter 3. This chapter reviews the literature pertinent to this thesis. It is presented in three parts which consider: the pathophysiology of head injury and secondary ischaemic injury, the literature on MRI (including diffusion weighted imaging) after head injury in experimental and clinical settings and the clinical management of head injury.

Chapter 4. This chapter describes the methods used in these research studies, with particular reference to the clinical protocols used for patient management. Details of the MRI and PET image acquisition and image processing and analysis are presented.

Collaborations: I was assisted in obtaining these imaging sequences by a team including radiographers, radio-chemists, nurses and other researchers within the group. However for each patient included studied I was directly responsible for some or all of the preparation and imaging. In the overwhelming majority of patients I was involved at every step of the studies as the main researcher responsible for the patients. In all patients I was the sole person responsible for the off-line image processing and analysis.

Chapter 5. Methodological developments carried out in the course of this research are presented. The testing of the infusion pumps required for patient care in MRI is described. The test-retest reproducibility of the ADC values obtained in DWI is described. Finally this chapter underlines the importance of ADC quantification of diffusion by describing T2* shade back effects on DWI and ADC variability in pericontusional areas seen on fluid attenuated inversion recovery (FLAIR) imaging.

Collaborations: I was the sole individual responsible for conducting these studies however equipment and advice was obtained from a collaborator in the department of medical physics.

Chapter 6. This chapter is concerned with the characterisation of ADC changes which occur early after head injury. The analysis describes the focal ADC changes around contusions and the ADC changes in regions of grey and white matter away from contusions.

Collaborations: None

Chapter 7. The physiological correlates of the focal ADC changes described in Chapter 5 are presented in this chapter. The values of regional CBF, oxygen extraction fraction (OEF), cerebral blood volume (CBV) and cerebral metabolic rate for oxygen ($CMRO_2$) used in these analyses were derived from ^{15}O-PET.

Collaborations: None

Chapter 8. Describes the ultrastructural findings in pericontusional tissue. These electron microscopy images are related to the other imaging findings. In the discussion microvascular ischaemia is suggested as a mechanism which may connect these results.

Chapter 9. This chapter describes the dynamic nature of the ADC changes around contusions. The effect of hyperventilation on the pericontusional ADC changes is explored.

Collaborations: None

Chapter 10. The conduct of the research, data analysis and results of the thesis are summarised.

Chapter 11. Future directions of research are discussed.

2 Physical Principles of the Imaging Techniques

2.1 MRI Physics

2.1.1 Basis of the MRI Signal

Magnetic resonance uses the signal obtained from atomic nuclei subjected to a magnetic field. Hydrogen nuclei are used in clinical MRI because of their abundance in human tissues. The property of hydrogen nuclei which produces a magnetic resonance signal is termed spin, and explanations of MRI often describe the nuclei as spinning bar magnets or gyroscopes. However, for individual nuclei, these models do not adequately describe the behaviour of individual spins. These spins are much better described by quantum mechanics. This review will use the simple "spinning magnet" models while acknowledging that quantum models of MRI are superior. If the reader is interested detailed explanations exist.[15]

When the hydrogen nucleus (proton) is placed in a static magnetic field, the spin vector of the particle (the principle axis of rotation) aligns itself with this field, this is similar to a compass needle aligning with the magnetic field of the Earth. These spins however behave like compass needles that are undamped and mounted on frictionless bearings. These compass needles therefore never come fully to rest but continuously oscillate around the direction of the magnetic field. In magnetic resonance the oscillation is termed precession and the frequency of the oscillation termed the precessional frequency. The precession means that there is a component of the spin magnetisation parallel to the static field and a component which is 90 degrees (transverse) to the field. The parallel component of the spin magnetisation vector is termed the longitudinal magnetisation and the transverse component is termed the transverse magnetisation (figure 1)

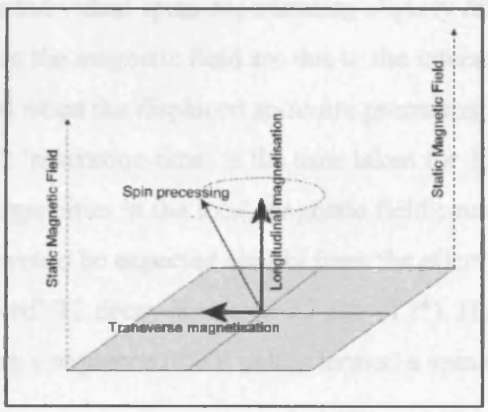

Figure 1. The figure shows a spin precessing about the axis of the static field. The dotted circle shows the precessional path. The vector of the magnetisation has components longitudinal and transverse to the static field.

The precessional frequency is proportional to the strength of the magnetic field and this can be calculated by the Larmor equation (equation 1). Energy can be imparted to the hydrogen nucleus if it is delivered at this precessional frequency.

$$\omega = \gamma B$$

Equation 1. The Larmor equation where ω = precessional frequency (Hz), B = strength of the static magnetic field (Tesla) and γ = gyromagnetic ratio (Hz/Tesla). The gyromagnetic ratio for hydrogen nuclei is 42.58 MHz/T giving precessional frequencies in the radio frequency range.

To generate a signal from the spins energy is delivered to the hydrogen nuclei as a electromagnetic pulse at the precessional frequency. This is termed a radiofrequency (RF) pulse since it is in the radiofrequency range. The RF pulse displaces the spins from their orientation in the static magnetic field. A pulse is termed a 90 degree pulse if it displaces the spin vector 90 degrees from the static magnetic field. When the RF pulse is switched off the spin vectors begin to realign with the static magnetic field. This realignment is associated with the recovery of longitudinal magnetisation and is termed T1 relaxation. Since T1 relaxation is an exponential process the T1 'relaxation time' for a tissue is the time taken for 63% (1 – 1/e) of the T1 signal to re-develop. The initial RF pulse not only displaces the spins away from the static magnetic field but also causes all the spins to precess in-phase (in synchrony). The spins then precess about the static field giving rise to a RF signal, which can be detected by receiver coils in the scanner. While initially the spins precess in-phase, the signal begins fade. This process is termed T2 relaxation and is due to the loss of synchrony in the spins (dephasing). The loss of synchrony occurs due to individual spins experiencing slightly different local magnetic fields. These variations in the magnetic field are due to the interaction with neighbouring spins. The signal emitted when the displaced spins are precessing in-phase decreases exponentially and the T2 'relaxation time' is the time taken for 37% (1/e) of the T2 signal to be lost. Inhomogeneities in the local magnetic field cause the T2 signal to decay much faster than would be expected simply from the effect of interactions with other spins. This 'observed' T2 decay is termed T2 star (T2*). However the true T2 can be calculated by applying a sequence of RF pulses termed a spin-echo sequence.

The values of the T1 and T2 (relaxation) time vary between tissues and these differences produce tissue contrast in MRI. The timing of the RF pulses and acquisition of the

emitted signal can emphasise the T1 or T2 properties of the tissues, the images thus obtained are termed T1 or T2 weighted images respectively. However it is important to note that these images will contain a degree of contrast from both T1 and T2 effects (as well as other more subtle MRI effects). When images are produced which are weighted for a particular signal they are simply termed 'images' while when quantitative images of an MRI signal are created they are termed maps. For example a T1 *weighted* image is simply termed a T1 image while a *quantitative map* of T1 relaxation times across the brain is termed a T1 map.

2.1.2 FLAIR Images

FLAIR images are obtained using an inversion recovery sequence. An inversion recovery sequences begin with an inversion pulse (a RF pulse which inverts the longitudinal magnetisation of the spins by 180 degrees). Following the inversion pulse the inverted spins begin to realign with the static field. The time taken for the spins to realign depends on the T1 time of the tissue. Tissues with short T1 times, such as fat, recover their longitudinal magnetisation fastest and tissues with long T1 times, such as cerebrospinal fluid (CSF), recover slowly. FLAIR is able to exploit this difference in recovery times to suppress signal from CSF. The FLAIR image is acquired from a spin echo sequence that is timed to excite the spins when the longitudinal magnetisation of the CSF spins are passing through zero as they realign after inversion. On FLAIR images therefore CSF appears black, irrespective of the contrast in other tissues. The exact contrast weighting of the FLAIR depends on the timing of the sequence. The FLAIR images used in this thesis are largely T2 weighted. FLAIR sequences are widely used in clinical imaging because pathology near the cortical surface or ventricles can be seen more easily if the signal from CSF is absent.

2.1.3 Diffusion Weighted MRI

Diffusion refers to the random, microscopic motion that water molecules undergo and which is usually called Brownian motion. During MRI this diffusion of water molecules causes an irreversible signal loss. While diffusion effects are present in all MRI they normally cause only a very little loss of signal. In diffusion weighted imaging however, the scan sequences are made sensitive to the signal loss due to diffusion effects. This is achieved by the application of paired, pulsed magnetic gradients. These magnetic gradients sensitise the sequence to the effect of diffusion and allow the diffusion to be quantified.

The extent of diffusion is not uniform in all brain tissue, it is restricted in some tissues and free (unrestricted) in others, and it is this that produces tissue contrast on DWI. Since diffusion causes signal loss in MRI, increased diffusion produces a dark area on the image. Conversely areas of reduced (restricted) diffusion cause less attenuation of the magnetic resonance signal leading to a brighter area. (Figure 2). The process by which the scan sequence quantifies diffusion involves some mathematics but is briefly outlined below and more fully explained in the appendix.

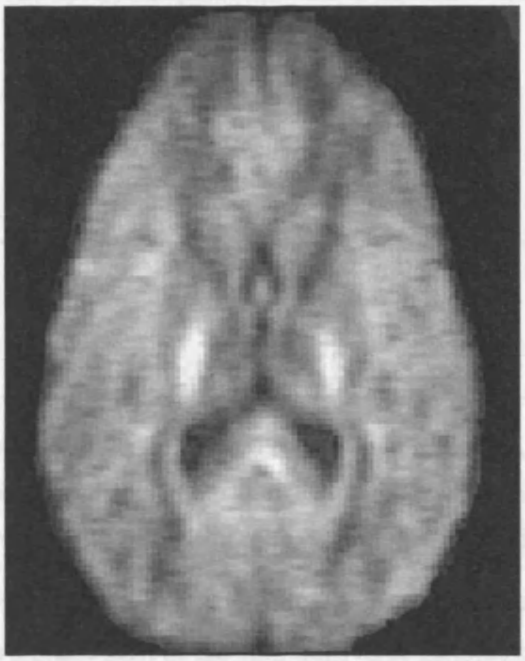

Figure 2. DWI shows areas of unrestricted diffusion, such as CSF filled ventricles, as dark.

2.1.4 Principles of Diffusion Weighted MRI Sequences

If we consider the case where the diffusion gradients are applied in one direction only the basic principles of diffusion imaging can be understood from a simple bipolar pulsed gradient experiment (Figure 3). In this sequence a 90 degree excitation pulse is followed at time TE/2 by a 180 degree refocusing pulse. This basic spin-echo sequence is altered by the application of paired gradients either side of the 180 degree pulse. These paired 'diffusion' gradients allow the re-phasing of signal from stationary spins whilst signal from moving spins (diffusion) is not rephased and the signal is therefore greatly reduced.

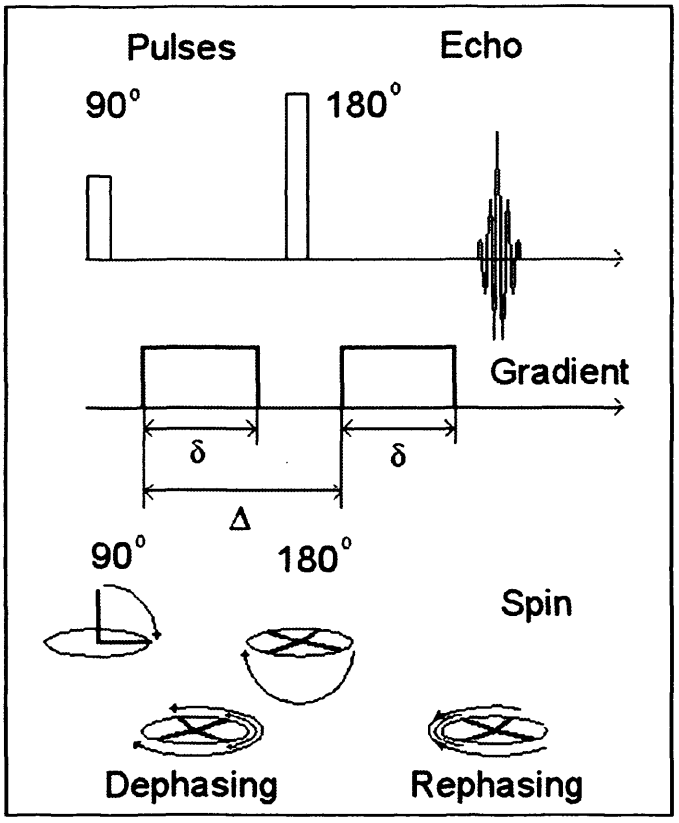

Figure 3. Basic diffusion sensitised sequence. Top is a basic spin-echo, readout sequence, middle shows the diffusion gradients of duration δ either side of the refocusing 180° pulse and separated by interval Δ. The behaviour of the spins is illustrated in the lower images.

Mathematically it is possible to use this signal loss to quantify diffusion. The first gradient pulse induces a phase shift of the spin transverse magnetization (T2), which depends on the spin position. A second gradient pulse is then applied after the 180 degree pulse which rephases the spins. If the spins move during the interval between these two gradients a net dephasing will remain and this results in loss of signal. For static spins, (molecules which do not diffuse) the net dephasing is zero, and there is no signal loss. For moving spins there is a net dephasing with associated signal loss.
The diffusion can be calculated from the degree of signal loss according to the Stejskal-Tanner equation. This is based on the work of EO Stejskal and JE Tanner and forms the basis of diffusion imaging.[16] The derivation of the equation is covered in the appendix.

$$S = S_0 e^{-bD}$$

Equation 2. The Stejskal-Tanner equation. S denotes the signal from a voxel, S_0 the signal without diffusion gradients, b is a constant which summarises the duration and strength of the diffusion gradients, D is the diffusion coefficient (which has dimensions of length^2.time^{-1}, usually given as mm^2/sec)

The b value for a particular sequence summarises the strength and duration of the diffusion gradients. It is given by equation 3.

$$b = \gamma^2 G^2 \delta^2 \Delta$$

Equation 3. γ denotes the gyromagnetic ratio, G the gradient strength, δ the gradient duration, Δ the time interval between the pulses.

The total distance covered by water molecules taking the "random walk" of diffusion is greater than the apparent distance that they have moved in a given time. To emphasise this point the maps of mean diffusion (D) are termed apparent diffusion coefficient (ADC) maps. It is important to understand the difference between DWI and ADC maps. Firstly image contrast seen on DWI images are typically reversed on ADC maps. Thus restricted diffusion is seen as dark regions on ADC maps and areas of higher diffusion (such as vasogenic oedema) are seen as bright regions. Secondly the signal on DWI represents several magnetic resonance effects, for example T2, T2* and T1 effects, in addition to the effect of diffusion. ADC maps however are specific to the effects of diffusion. Therefore to quantify diffusion and eliminate other MRI effects it is useful to construct ADC maps. ADC maps are created by solving the Stejskal-Tanner equation (Equation 2) for D at each image voxel.

'Normal' ADC Values in the Brain after Head Injury imaged at Three Tesla

The diffusion of water in the brain varies according to the type of brain tissue, CSF has a high ADC value (around 25 x 10^{-4} mm^2/sec), highly structured white matter such as the corpus callosum has low ADC values (around 3 x 10^{-4} mm^2/sec) and grey matter has intermediate ADC values (around 6-9 x 10^{-4} mm^2/sec). ADC values in brain tissues are similar in both hemispheres, and between men and women. They do not vary significantly with age in adult life however young children are known to have higher ADC values.

Typical adult ADC values in a range of brain tissues are shown in the table below.

Tissue	Average ADC (mm^2/sec)
Cortical grey matter	7 – 9 x 10^{-4}
Deep grey matter	6 – 7 x 10^{-4}
Mixed white matter	4 – 6 x 10^{-4}
Corpus callosum	3 – 4 x 10^{-4}

The diffusion of water within a tissue type also varies according to proportion of intracellular and extracellular fluid. Water molecules in the intracellular fluid are relatively restricted in their diffusion due to interaction with intracellular proteins and other structures. Conversely, when water is in the extracellular fluid compartment its diffusion is relatively free. This difference in the diffusivity of water within different physiological compartments provides insight in to the relative amounts of fluid in these two tissue compartments. This allows ADC changes to demonstrate the formation of intracellular (cytotoxic) oedema and extracellular (vasogenic) oedema after CNS injury.

Anisotropy

The diffusion within tissues may not be equal in all directions (isotropic); this preference for diffusion in one direction is termed anisotropy. Anisotropy arises from the presence of cellular and extracellular structures. This is most clearly illustrated in white matter where myelinated fibre tracts allow more diffusion parallel to the fibre tracts than across them (as shown in figure 4).

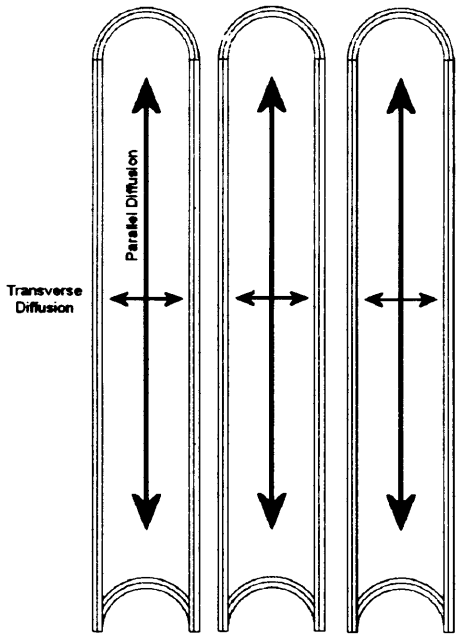

Figure 4. Directionality of diffusion. The figure shows three parallel myelinated nerve fibres and the effect of the fibre orientation on the directionality of diffusion. The fibres allow relatively free diffusion parallel to their main axis, however transverse diffusion is restricted by the fibre tracts.

This directionality of diffusion can be measured during diffusion MRI by applying the diffusion gradients in a number of directions. The directional anisotropy in a tissue cannot be adequately described by a scalar measure such as ADC but is better described

by a 3x3 tensor matrix. Where each element represents the diffusion in a particular direction. The 3x3 tensor can be visualised as a three dimensional ellipsoid shape, termed a diffusion tensor (figure 5).

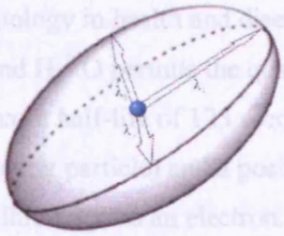

Figure 5. A diffusion tensor ellipsoid. Arrows represent the three principal Eigen vectors (λ1, λ2, and λ3)

The diffusion along the three principal axes of the tensor are termed the Eigen values of diffusion; which can be used to summarize the degree of anisotropy. The fractional anisotropy (FA) is a summary measure of the degree to which the three Eigen values differ. An FA of 0 describes isotropy (a spherical tensor) and an FA of 1 describes complete anisotropy (an infinitely long tube). Biological tissue has FA values between 0 and 1 which can be represented as ellipsoids of various shapes. FA maps show areas of highly directional diffusion as high intensity (figure 6). The equation for FA is given in the appendix.

Figure 6. FA map showing areas of high anisotropy (directional diffusion), such as white matter tracts, as hyperintense.

These FA maps were only used in this research to identify areas of grey and white matter during image analysis.

2.2 PET Physics

The use of positron emitting isotopes, incorporated into biological tracers, has enabled in-vivo studies of human physiology in health and disease. In the case of ^{15}O-PET the administration of $^{15}O_2$, $C^{15}O$ and $H_2{}^{15}O$ permits the quantification of regional CBF, CBV, $CMRO_2$ and OEF. ^{15}O has a half-life of 123 seconds and in its decay emits a neutrino (a very weakly interacting particle) and a positron. The positron travels a short distance in tissue before it annihilates with an electron. The energy of annihilation produces two photons, each with an energy of 511 keV at 180° to each other.
The paired photons can be detected by the cylindrical array of detectors in the PET scanner and converted into an electrical signal. Tomographic image reconstruction is then used to recover the three-dimensional tracer distribution. The in-plane resolution of the technique, on our scanning system, is 6.7 mm, but the low signal to noise ratio of the images necessitates the application of a degree of spatial smoothing such that the effective in plane resolution is 7.8 mm.

CEREBRAL BLOOD VOLUME

The avid binding of carbon monoxide to haemoglobin allows $C^{15}O$ to be used as a tracer for the measurement of CBV. The patient inhales a small quantity of $C^{15}O$ and 60 seconds later, after carboxyhaemoglobin has equilibrated throughout the blood volume, emission data are collected for five minutes. During this time blood samples are taken to quantify the activity in the peripheral blood. rCBV is calculated according to equation 4:

$$rCBV = \frac{C_{tissue}}{C_{blood} \times R}$$

Equation 4. C_{tissue} is the tissue radioactivity measured by the scanner, C_{blood} is the radioactivity measured in the peripheral blood, R is the ratio of the cerebral to peripheral blood haematocrit. This value is usually assumed to be 0.85 ml/100g of brain tissue,[17 18] but it should be noted that this assumed value of R is unlikely to hold true for all tissues. It may, in particular, cause underestimates of CBV where blood flow is high, this is discussed below (Section 2.2.1).

CEREBRAL BLOOD FLOW

The steady state method of determining CBF is best suited to studying CBF after head injury since it is accurate in the low CBF range. $H_2{}^{15}O$ is administered as a constant intravenous infusion, and after a build up period of 10 minutes a stable level of activity

is achieved, during which two five minute emission frames are obtained. rCBF is calculated from the following equation:[19]

$$rCBF = \frac{\alpha}{C_{blood}/C_{tissue} - 1/\lambda}$$

Equation 5. C_{tissue} is the tissue radioactivity measured by the scanner, C_{blood} is the radioactivity measured in the peripheral blood, α is the decay constant for ^{15}O ($\ln 2/T_{1/2}$=0.00564 seconds^{-1}), λ is the blood-brain partition coefficient for water.

The model assumes a linear relationship between tissue radioactivity and rCBF. However this relationship does not hold at high CBF values and high CBF values (even in some areas of normal grey matter) may be underestimates. The model assumes a value for λ of 0.95 across the whole brain, yet values for λ differ in white and grey matter. These two problems mean that rCBF values in mixed grey-white matter may be underestimated by up to 20%.[20]

CEREBRAL OXYGEN METABOLISM

Regional measurements of OEF and $CMRO_2$ are obtained following a steady-state inhalation of $^{15}O_2$. Trace amounts of labelled $^{15}O_2$ are inhaled in air for 10 minutes and emission data are collected while the inhalation is continued for a further 10 minutes. In essence the calculation relies upon the equation

$$OEF = \frac{^{15}O \text{ metabolised by the tissue}}{^{15}O \text{ delivered to the tissue}}$$

Equation 6

However there are three sources of ^{15}O activity during the scan: $^{15}O_2$ metabolised by the tissue and converted to $H_2{}^{15}O$, $^{15}O_2$ in arterial blood, and $H_2{}^{15}O$ produced in the tissues, which re-circulates during the scan. In addition, a significant amount of unextracted $^{15}O_2$ is present in the venous blood and a correction for rCBV must be made.

Therefore data from three scans must be available to determine rOEF, along with arterial and plasma samples which are required to measure $^{15}O_2$ bound to haemoglobin and $H_2{}^{15}O$ in plasma and blood. The equation for rOEF' (OEF uncorrected for CBV) is shown (equation 7):[19 21]

$$r'OEF = \frac{\left(\frac{C_{tissue}O_2}{C_{tissue}H_2O} \times \frac{C_{arterial}H_2O}{C_{plasma}O_2}\right) - \left(\frac{C_{arterial}H_2O}{C_{plasma}H_2O}\right)}{\frac{C_{arterial}O_2}{C_{plasma}O_2} - \frac{C_{arterial}H_2O}{C_{plasma}H_2O}}$$

Equation 7. $C_{tissue}O_2$ is the tissue activity during the steady state $^{15}O_2$ inhalation, $C_{tissue}H_2O$ is the tissue activity during the steady state $H_2{}^{15}O$ infusion, $C_{arterial}H_2O$ is the whole blood activity during the steady state $H_2{}^{15}O$ infusion, $C_{plasma}O_2$ is the plasma activity during the steady state $^{15}O_2$ inhalation, $C_{plasma}H_2O$ is the plasma activity during the steady state $H_2{}^{15}O$ infusion, $C_{arterial}O_2$ is the whole blood activity during the steady state $^{15}O_2$ inhalation

As a significant component of the measured tissue radioactivity is related to the intravascular $^{15}O_2$ that has not been extracted and to avoid overestimating OEF it is necessary to correct for this using an independent measurement of the CBV. The corrected value for OEF is calculated using equation 8.[22]

$$rOEF = \frac{rOEF' - X}{1 - X}$$

Equation 8

where X is given by:

$$X = \frac{\text{rCBF}/100 + 60\lambda}{\text{rCBF}(r\text{CBV}) + 60\lambda}$$

Equation 9. λ is the blood-brain partition coefficient for water.

CEREBRAL OXYGEN METABOLISM

Finally, $CMRO_2$ can be derived from the following relationship:

$$rCMRO_2 = rOEF \times rCBF \times C_aO_2$$

Equation 10. CaO_2 is the blood oxygen content in μmol/100ml

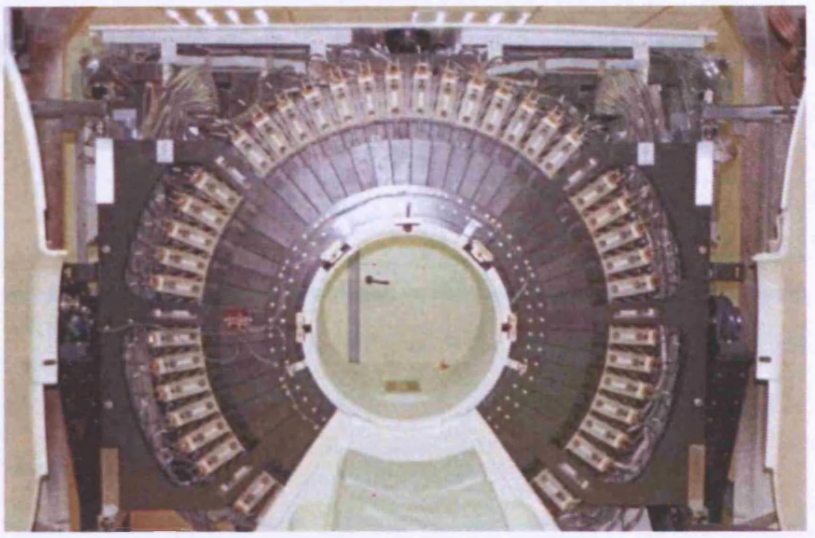

Figure 7. PET scanner with the cover removed to demonstrate the cylindrical array of detectors and photomultipliers. The patient couch (seen at the bottom of the picture) is moved into the bore during scanning however all other parts are static.

2.2.1 Assumptions and limitations of the oxygen-15 steady-state model

The steady-state ^{15}O PET technique is considered the optimum clinical method for measurement of rCBF. However it has some limitations, which are important to consider.

1. The model assumes uniform values for the partition coefficient of water (λ) and for the cerebral to peripheral haematocrit ratio (R); assumptions which may be especially invalid in the injured brain and which produce underestimates of high CBF values.

2. A complete PET dataset of the three scans ($^{15}O_2$, $H_2{}^{15}O$ and $C^{15}O$) requires approximately 60 to 90 minutes to obtain; during which time, even with careful clinical care, physiological parameters such as intracranial pressure (ICP), cerebral perfusion pressure (CPP), $PaCO_2$ may change.

3. Whilst better than some other techniques, the spatial resolution of PET scans is such that small areas of damage may be difficult to perceive.

3 Review of the Literature

3.1 Cerebrovascular Physiology & Pathophysiology

3.1.1 Cerebral Ischaemia - Cerebral Energy Requirements

Overall, the brain receives a blood flow of around 50ml/100g/min. More metabolically active tissue such as grey matter receives around 70ml/100g/min, while white matter receives around 20ml/100g/min. This large cerebral blood flow is necessary because the brain is the most metabolically active tissue in the body. While it makes up only 2% of body weight, the brain's energy consumption accounts for 25% of the total body glucose utilisation. This glucose is metabolised in the brain to produce ATP which provides energy to support the structure of the cells, drive axonal flow, and synthesise, package, release and reuptake neurotransmitters. However the process with the greatest energy consumption is the maintenance of the transmembrane ionic gradients by ionic pumps (accounting for around 70% of the brains ATP usage). Without this essential process the propagation of nerve action potentials within the brain would fail.[23]

3.1.2 Insights into Ischaemia from Stroke Research

Before discussing the literature relevant to ischaemia after head injury it is worth reviewing the data from stroke. In acute stroke there is an abrupt cessation of arterial supply, typically due to arterial thrombosis or embolism, to a region of metabolically normal brain. It is therefore the simplest example of cerebral ischaemia, and it has been extensively studied in animals and humans. The process of secondary ischaemia after head injury differs from acute stroke. For example, there is significant suppression of cerebral metabolism after head injury, and the mechanisms by which perfusion is compromised often occur more gradually, which may allow the brain to tolerate ischaemia better. Despite these differences the mechanisms of ischaemia are likely to have some commonality. Stroke therefore provides a useful background against which ischaemia after head injury may be considered.

The high metabolic demand and limited energy reserves of the brain mean that when ischaemia occurs, tissue energy demands cannot be met and cellular ATP levels fall. This is typified by acute ischemic stroke, where the reduction in ATP results in decreased function of ion pumps, such as Na-K-ATPase, which uses ATP to maintain high intracellular concentrations of K^+ and low intracellular concentrations of Na^+. Efflux of K^+ from neurons results in prolonged elevations in extracellular K^+ and massive cellular depolarization.[24] Other cellular ion gradients are also lost; intracellular Na^+ and Ca^{2+} rise and intracellular Mg^{2+} falls. Extracellular concentrations of many

neurotransmitters are increased during ischemic stroke. Entry of Ca^{2+} via voltage sensitive Ca^{2+} channels stimulates release of vesicular neurotransmitter pools, including the excitatory amino acid neurotransmitter glutamate. At the same time, Na^{+} dependent reuptake of glutamate is impaired by the loss of transmembrane ion gradients. Thus, both impaired glutamate uptake and enhanced glutamate release contribute to sustained elevations of extracellular glutamate in the ischemic brain.[25] This excess glutamate leads to further damaging ionic and biochemical changes, a process known as excitotoxicity. In addition to the changes at the cell membrane, the fall in pO_2 during ischaemia leads to a lactic acidosis as cells undergo a shift from aerobic metabolism to anaerobic glycolysis, which decreases the pH of the ischemic tissue from the normal 7.3 to around 6.5.

These data from ischemic stroke research provide insights into how physiology and biochemistry interact to modify ischemic brain injury. While ischaemia arises from an inadequate supply of oxygenated blood to the tissue (or an inability of the tissues to use the available blood supply) there are different tissue susceptibilities to ischaemia. Even cells of the same type lying side by side in the brain, can display different vulnerabilities to equivalent degrees of ischaemia. This variable vulnerability to ischaemia coupled with the ability of tissue near the periphery of the ischemic region to maintain some blood supply from neighbouring vascular territories, lead to the concepts of stroke 'core' and 'penumbra'.[26] The core of the ischemic area of brain undergoes rapid and irreversible ischemic damage, while the penumbra, which is either less susceptible to ischaemia or is able to maintain some blood supply, is functionally impaired but remains viable. The exact physiological and radiological definitions of these two regions after stroke remain a subject of debate.[27-34]

CLINICAL RELEVANCE OF THE PENUMBRA

Clinically, the penumbra can be thought of as the tissue which is threatened but which can be salvaged by therapeutic intervention. Imaging such as computed tomography (CT), PET and MRI have been used both as research techniques and clinical tools to assess the extent of damaged and hypoperfused brain following stroke and to select patients for thrombolysis.[35] Conventional CT cannot reliably distinguish the ischemic penumbra.[36 37] However, CT techniques, such as perfusion contrast CT contrast and Xe-CT, are able to define the tissue at risk and hold clinical promise.[38 39] O^{15}-PET can quantify regional CBF, $CMRO_2$, OEF and CBV, and by relating blood flow and metabolism, is able to define ischemic tissue based on physiological thresholds.[40] However, O^{15}-PET is an expensive, specialised technique, and is not widely available,

and therefore generally remains a research technique. MRI techniques, particularly DWI and perfusion weighted MRI (PWI) are widely used imaging techniques after ischemic stroke. The acute DWI changes following stroke are temporally related to run down of ATP,[41 42] and reflect the development of cytotoxic oedema, as the transmembrane ionic gradients are lost and the cells swell.[43] While the early DWI changes following stroke have been shown to be reversible in some studies,[44 45] increased intensity on DWI is generally thought to be an early and useful marker of local cytotoxic oedema. These changes after stroke usually evolve over a characteristic time course.[46 47]

Even when these changes are reversible, it is clear that they represent tissue which is under a significant ischaemic burden, and selective neuronal loss or secondary imaging changes occur even if the initial DWI abnormality is reversible.[33 48] The DWI-PWI mismatch is the area of reduced perfusion seen on PWI which lies outside the DWI abnormality. This represents the hypoperfused penumbral tissue following stroke; this tissue is the main target of thrombolysis and the paired techniques of DWI-PWI are still of great practical use when selecting patients for thrombolysis.[28 49]

In summary, there are differences in the pathophysiology of head injury and ischemic stroke, which mean that the process of ischemic damage after stroke may not be a fully acceptable paradigm for ischaemia after head injury. However, both stroke and ischemic damage following head injury share some commonality in their pathophysiology[50-52] and MRI imaging findings.[53] This has lead to the concept of a traumatic penumbra following head injury which is similar to the ischemic penumbra after stroke.[54 55] A better understanding of the MR imaging appearances following head injury may be facilitated by a description the mechanics and pathophysiology of head injury. This is therefore reviewed below.

3.2 Mechanics and Pathophysiology of Head Injury

The severity and type of impact occurring during head injury will substantially influence the structural lesions that ensue (Figure 8).

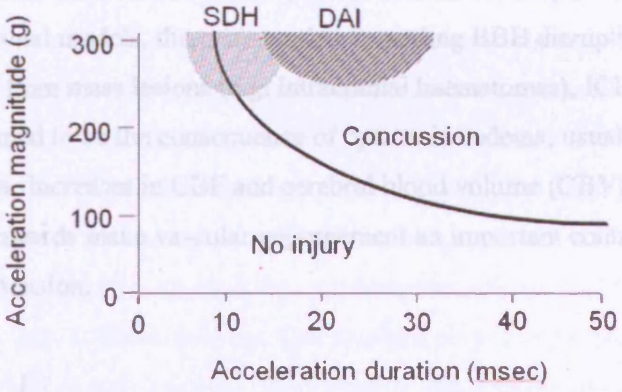

Figure 8. Biomechanics of head injury. Diagrammatic representation of the duration and intensity of acceleration-deceleration insult on the type of injury produced. (Redrawn from Bullock, 1997).

The acceleration-deceleration forces that ensue from impact during falls and motor vehicle accidents can produce axonal dysfunction and injury, brain contusions, and axial and extra-axial haematomas. The generation of such macroscopic injury is associated with microscopic and ultramicroscopic changes, including ischaemic cytotoxic oedema, astrocyte swelling with microvascular effacement and dysfunction, microglial activation and recruitment, blood brain barrier disruption with vasogenic oedema, and phasic inflammatory cell recruitment.[56]

These varied pathophysiological consequences of a single structural pathology are well reflected by sequential changes in cerebrovascular physiology that are observed following head injury. Classically, cerebral blood flow (CBF) is thought to show triphasic behaviour[57 58] (Figure 9). Early after head injury (within 12 hours), global CBF is reduced, sometimes to ischaemic levels. Between 12 and 24 hours post injury, gradually CBF increases towards baseline levels, and the brain may exhibit supranormal CBF two to five days post injury. While many reports refer to this phenomenon as hyperaemia, the absence of consistent reductions in cerebral oxygen extraction suggest that metabolism and blood flow often remain coupled, and a more appropriate label is coupled hyperperfusion. CBF values begin to fall several days following head injury, and in some patients these reductions in CBF may be associated with marked increases in large vessel flow velocity on transcranial Doppler ultrasound that suggest vasospasm.

These time-varying haemodynamic responses also define the vascular contribution to ICP elevation in time. Immediately after head injury there is no vascular engorgement,

and though a transient blood brain barrier (BBB) leak has been reported in the first hour after impact in animal models, there are no data regarding BBB disruption at this stage in humans. Apart from mass lesions (e.g. intracranial haematomas), ICP elevation during this phase is assumed to be the consequence of cytotoxic oedema, usually secondary to cerebral ischaemia. Increases in CBF and cerebral blood volume (CBV) from the second day post-injury onwards make vascular engorgement an important contributor to intracranial hypertension.

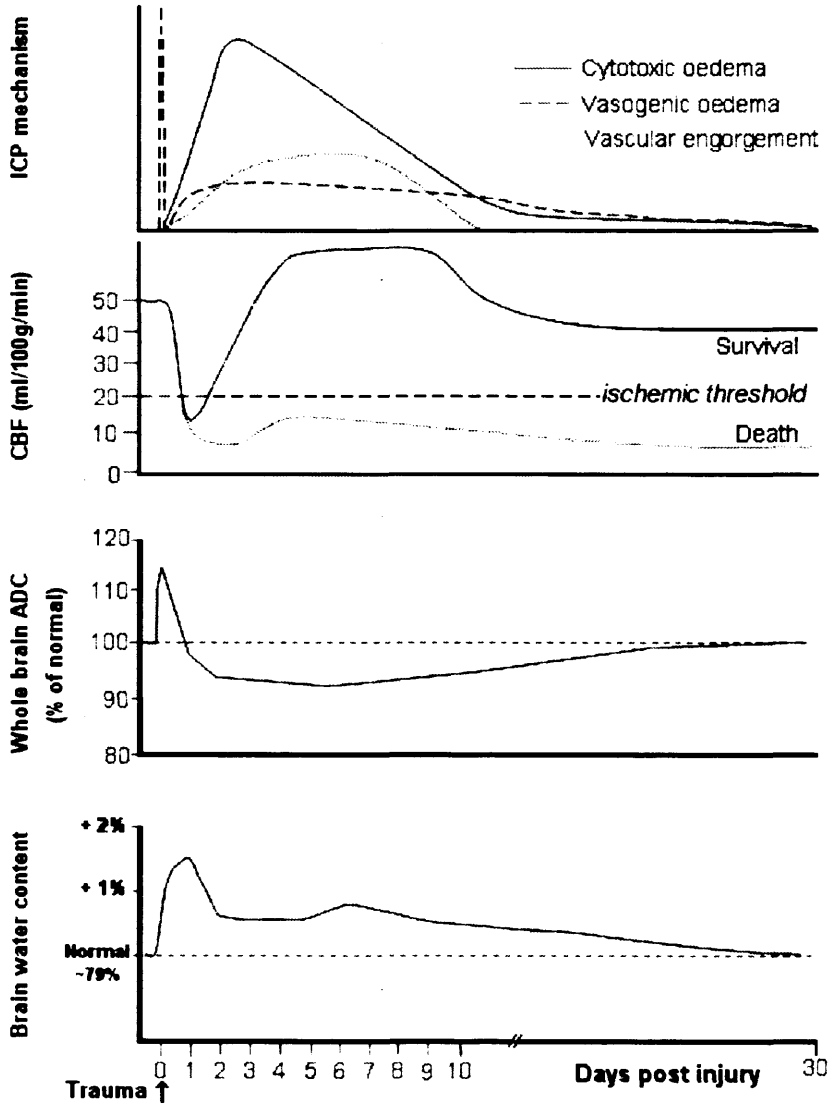

Figure 9. Pathophysiology of brain water and CBF. Diagrammatic representation of changes in brain water, average ADC, and CBF, and the associated physiological processes responsible for intracranial hypertension at various points following head injury. The temporal patterns of the various processes depicted are based on a consensus for both clinical and experimental literature cited in this chapter.

Following a transient initial dysfunction, the BBB appears to become leaky between the second and fifth days post-trauma, and vasogenic oedema then contributes more to brain swelling. It is important to recognise that brain water is increased within the first hour following injury, and remains high for up to two weeks (Figure 9). Over this period the excess brain water probably redistributes to varying extents between the intra- and extra-cellular compartment. In the setting of ischaemic stroke, early intracellular oedema is usually referred to as "cytotoxic", and often attributed to neuronal ischaemia. The situation in head injury is more complex. Cell swelling may involve astrocytes and be the consequence of glutamate reuptake rather than the direct consequence of ischaemia. Alternatively, the extracellular oedema that accumulates following brain trauma may be protein rich and restrict the diffusion of extracellular water,[58] endowing it with attributes that result in MR appearances that are conventionally associated with intracellular oedema. Finally, the cell swelling and extracellular oedema may result in microvascular injury and collapse,[59 60] and be the cause, rather than the consequence of ischaemia (figure 10).

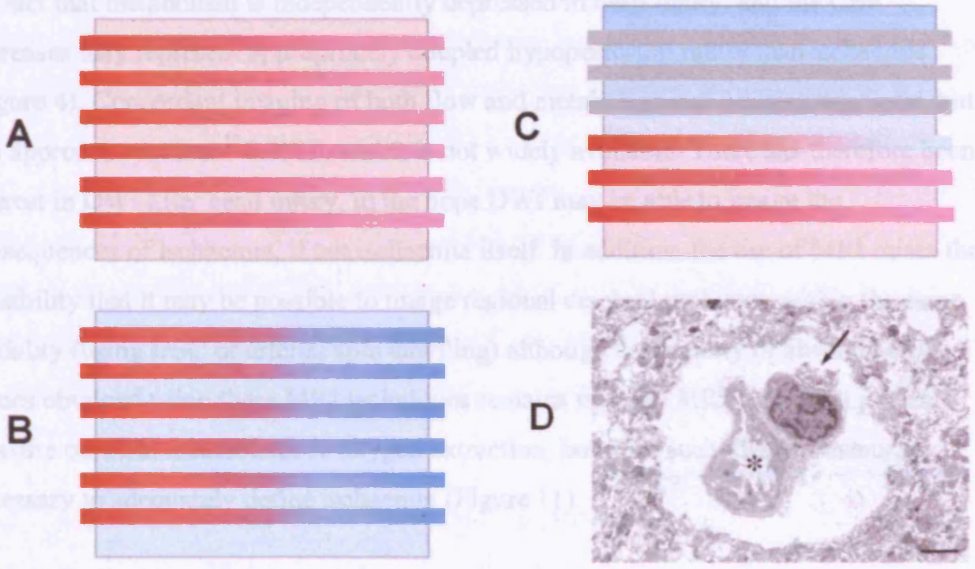

Figure 10. Macrovascular and microvascular ischaemia. Conventionally, reductions in cerebral perfusion are due to reductions in cerebral perfusion pressure or obstruction of proximal conductance vessels. This results in relatively uniform ischaemia in the territory of the vessel involved, and greater oxygen extraction (B) when compared to the normal setting (A). However, microvascular injury associated with head trauma can cause astrocyte swelling, perivascular oedema, endothelial swelling, and microvascular collapse (D). This results in tissue hypoxia with heterogeneous patterns of ischaemia and oxygen extraction (C).

While ischaemia is common at postmortem in fatal head injury,[1] CBF reductions are generally modest in the first few days following injury. Two different factors may provide explanations for this discordance. First, ischaemia may be an ultra-early event (<12 hours),[61] and may be missed by many clinical studies, which are commonly undertaken at later time points. Second, there may be substantial pathophysiological heterogeneity in the injured brain, and the impact of regional critical ischaemia at later time points may be diluted by surrounding normal tissue, with no significant net effect on global measures of CBF.[62] Since structural changes, as detected by CT or conventional MRI, are likely to be relatively late and irreversible, these considerations have lead to the conclusion that there is a need to image physiology and metabolism in such patients.

The best established technique for physiological imaging is the use of stable Xenon CT studies for measurement of rCBF. While perfusion imaging confirms the presence of regional hypoperfusion in head injury, interpretation of these findings is confounded by the fact that metabolism is independently depressed in head injury, and the CBF decreases may represent appropriately coupled hypoperfusion rather than ischaemia (Figure 4). Concordant imaging of both flow and metabolism can address this issue, but this approach requires ^{15}O-PET, which is not widely available. There has therefore been interest in DWI after head injury, in the hope DWI may be able to image the consequences of ischaemia, if not ischaemia itself. In addition, the use of MRI raises the possibility that it may be possible to image regional cerebral perfusion within the same modality (using DSC or arterial spin labelling) although the validity of absolute CBF values obtained using these MRI techniques remains unclear. MRI cannot (at present) measure cerebral metabolism or oxygen extraction, however such measurements are necessary to adequately define ischaemia (Figure 11).

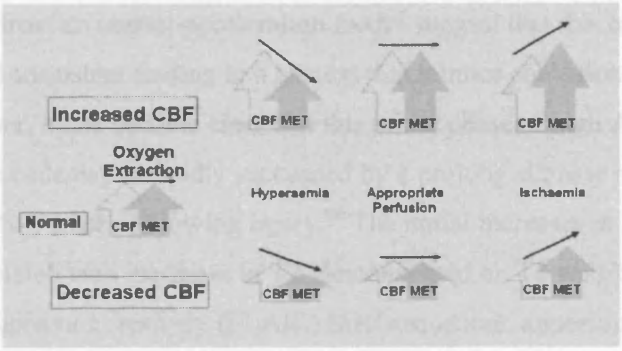

Figure 11. Conceptual paradigms in cerebral ischaemia. Conventionally, hypoperfusion is thought to represent ischaemia, and hyperperfusion, hyperaemia. However, these definitions are no longer valid when there are independent changes in cerebral metabolic rate (MET), as have been shown in head injury. In these settings, ischaemia can only be defined by documenting an increase in oxygen extraction fraction (OEF), or by showing that CBF reductions produce cytotoxic oedema.

3.2.1 Insights from MRI in Experimental Models of Head Injury

A variety of animal models have been used to mimic human head injury. While the details of these models are covered in other publications, it is important to recognise that none of these covers the entire spectrum of pathology observed in humans. Broadly speaking, the controlled cortical impact model primarily produces a focal cortical contusion with some deeper injury, while the impact acceleration model is similar but produces a greater degree of acceleration-deceleration insult, and may produce more axonal shearing. The lateral fluid percussion injury produces a more widespread and diffuse injury over the injured hemisphere, and also results in transmitted pressure wave through the brain. Other models mimic subdural and epidural haematomas, but DWI studies of these models are limited.

3.2.2 DWI Changes after Experimental Head Injury

Despite the important role ascribed to cerebral ischaemia in the context of head injury, early MRI studies with diffusion-weighted imaging suggested that the pathophysiology in animal models of head trauma was significantly different from that seen in simple ischaemia. Hanstock et al[63] showed that within the first four hours post injury, rats subjected to a moderate fluid percussion injury showed increases, rather than decreases in ADC, contrary to the findings in acute ischaemic stroke. These data suggested early vasogenic oedema, and were concordant with previous studies that had demonstrated early opening of the blood brain barrier using a variety of techniques, including Evans blue extravasation[64] and Gd-DTPA enhancement on MR imaging.[65]

More recent data from an impact-acceleration model suggest that this early increase in ADC is a real and consistent finding in a context that mimics contusion in human head injury.[65 66] However, it has become clear that this initial phase of high ADC (which implies vasogenic oedema) is rapidly succeeded by a prolonged phase of low ADC, which lasts up to two weeks following injury.[66] The initial increases in ADC are consistently associated with increases in T2, demonstrated on T2 weighted spin echo or fluid attenuation inversion recovery (FLAIR) MRI sequences, appearances which characterise vasogenic oedema. At least at early stages, the ADC increases are also temporally concordant with increased BBB leak as demonstrated by local enhancement following administration of Gd-DTPA.[65] Interestingly, both the early increases in ADC, and the subsequent reductions in ADC occur against a background of increased brain water content, which may only be small (a rise from 79% to 81%), but is clearly associated with disruption of normal physiology and characteristic imaging findings.[66] The severity of ADC reduction in such models may be substantially enhanced by hypotension and hypoxia, which add physiological insults to the picture produced by traumatic injury.[67] The detection and temporal patterns of the high and low ADC phases is also crucially dependent on the precise model used, the severity of insult, and the time points at which imaging is undertaken. Consequently, departures from this pattern have been reported by other authors,[68-70] who have used somewhat different methodology. ADC reductions, which are usually interpreted as signifying ischaemic cytotoxic oedema, are not confined to contusion models. Other studies, in models of experimental subdural haematoma, show reductions in ADC values in underlying cortex by one hour post insult, which become more extensive over the following two hours.[71]

3.2.3 PWI Changes in Experimental Head Injury

Perfusion weighted imaging in experimental models of head injury has employed both susceptibility contrast agents[69 72] and arterial spin labelling (ASL) techniques.[73] In summary, these studies show significant reductions in relative CBF (rCBF) and CBV (rCBV). Significantly, early PWI (performed one to three hours post injury) showed far more severe and widespread perfusion deficits when compared to imaging studies that were undertaken 24 hours post head injury.[73] These studies also confirm the perfusion heterogeneity in the injured brain, both at early and late time points, and demonstrate pericontusional hypoperfusion,[69 73] the severity of which correlates with early reductions in regional ADC. However, the extent of subsequent histological injury is better reflected by the extent of ADC change, rather than the perfusion deficit, which is typically much larger.[69] One important methodological finding is the observed

heterogeneity in T1 values across the injured brain,[73] which results in marked inaccuracies in calculated CBF with ASL techniques, if normal T1 values are used.

3.2.4 Interpretation of Experimental MRI Data

While these data provide important pointers to understanding the imaging findings on diffusion weighted MRI in humans, they possess two major shortcomings. First, no data are available from animal studies that clearly delineate DWI responses in diffuse axonal injury, since experimental models of this pathology are less well developed and characterised. This is a major failing since axonal shearing is an important pathological finding and prognostically relevant lesion in human head injury. Second, human head injury often combines several lesions including contusions, extra-axial haematomas, and axonal shearing injury, and although some MR studies have attempted to address this issue,[74] the models used may not be representative, and the effect of interaction of these varying pathologies on imaging appearances remains unclear.

3.2.5 Acute MRI in Clinical Head Injury – DWI Detection of Cytotoxic Oedema

Early MR studies of head injured humans used conventional sequences to demonstrate the sensitivity of the technique for detecting axonal injury, with demonstration of patterns of pathology that had major prognostic significance.[75] Subsequently several authors showed that DWI revealed lesions that were in keeping with axonal shearing injury, days to months following head injury.[76-80] In some of these instances, conventional MRI was entirely normal.[79] Several of these studies showed major reductions in regional anisotropy on diffusion tensor images (DTI), particularly in subcortical white matter in the frontal and temporal regions, and in the splenium of the corpus callosum, all of which are classical sites of diffuse axonal injury. The sensitivity of DWI and DTI in demonstrating these lesions was significant, and they were thought to represent loss of water anisotropy in sheared white matter tracts. However, increases in signal intensity on DWI images were seen as early as one day post injury[77 81] and were seen to be transient in other studies,[78 81] this pattern of DWI hyperintensity may represent cytotoxic oedema. Clearly the interpretation of some early studies remains difficult as ADC values were not reported, and the coexistence of T2 changes made it difficult to exclude the presence of T2 "shine through" in DWI images with significant T2 weighting.

3.2.6 MRI in Acute Head Injury – DWI Detection of Vasogenic Oedema

A framework for classifying changes on DWI images has been suggested by Hergan et al,[82] who classified lesions based on DWI and ADC appearances:

Type 1	Lesions are DWI and ADC hyperintense. Representing vasogenic oedema, with the DWI hyperintensity arising from T2 shine through effects.
Type 2	Lesions are DWI hyperintense and ADC hypointense Representing cytotoxic oedema
Type 3	Lesions have a haemorrhagic core surrounded ADC hyperintensity. Representing core and pericontusional vasogenic oedema

In addition, all scans were classified into three groups based on the size and extent of lesions, with group A consisting of focal injury, group B consisting of regional or confluent focal injuries and group C representing diffuse or extensive injury.

3.2.7 MRI in Acute Head Injury – Complex DWI Changes

While the classification suggested by Hergan may be useful, it is not yet widely used and may represent an oversimplification. For example, a narrow rim of low ADC just outside regions of pericontusional vasogenic oedema has been reported by some authors.[10 11] These findings are reminiscent of low ADC cuffs seen around intracerebral haemorrhage in some patients.[83] ADC reductions are typical of tissue ischaemia and whether this rim of reduced ADC around the contusions represents tissue ischaemia is unknown.

3.2.8 MRI in Acute Head Injury – DWI Detection of Axonal Injury

As described in section 3.2.4 the techniques of DWI and DTI possess great sensitivity in detecting axonal injury.[84] The burden of axonal injury is often best appreciated on fractional anisotropy (FA) maps, which provide a quantitative measure of the anisotropy within an imaging voxel (figure 12). The presence of intact myelinated white matter tracts results in marked anisotropy, and FA maps clearly show the white matter pathways in the brain. While T2* weighted gradient echo images may be more sensitive at detecting the microhaemorrhages associated with axonal injury,[85 86] there seems to be little doubt that DWI is better at detecting axonal shearing. In one study, DWI identified 30% more shearing injuries than conventional MRI within 48 hours of head injury, with most of these seen as an increase in ADC.[84]

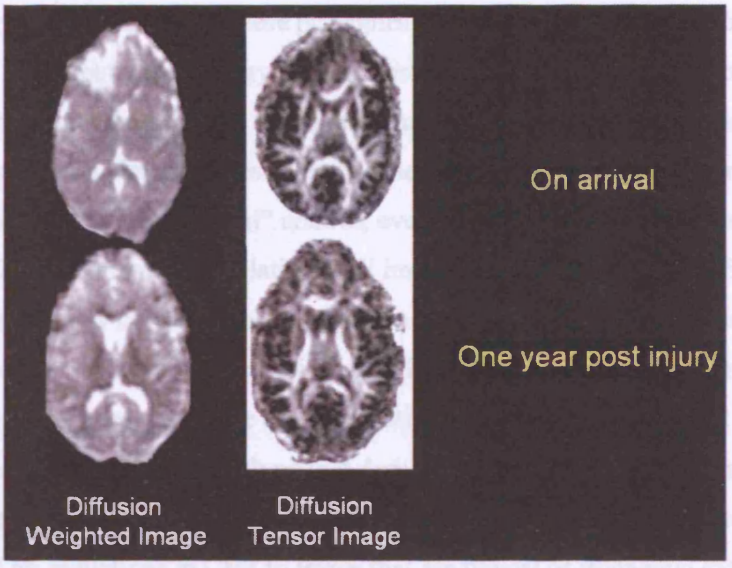

Figure 12. DTI images from one of our patients imaged acutely and at one year after head injury. Diffusion weighted images (left), and DTI, FA map (right), obtained within 24 hours of head injury demonstrate the value of DTI imaging in demonstrating axonal injury. The loss of white matter anisotropy in the right frontal region is evident on the FA map, and coincides with a hyperintense lesion on the DWI frame. Follow up DTI at one year (lower image pair) show that the white matter tracts have, in the main, survived intact.

MRI in acute head injury – perfusion weighted imaging

While some experimental studies have reported on the use of PWI, there are no published clinical studies using the technique in head injury (although BOLD fMRI techniques have been used for functional imaging in the follow up of patients after head injury).[87]

3.2.9 Interpretation of findings

The data presented in this chapter show the prominent and growing role of diffusion and perfusion MR in defining, diagnosing and understanding traumatic brain injury. However, while several experimental and clinical studies have revealed intriguing findings, their interpretation is not straightforward. Our understanding of the pathophysiology underlying acute CNS insults is based on a conceptual framework generated in the setting of stroke. While several questions remain to be answered in the setting of stroke, the large clinical database and a substantial experimental literature have allowed us to at least define the boundaries of our understanding and provide an integrated (if incomplete) picture of how clinical DWI and PWI changes may be interpreted.

Unfortunately, it is unlikely that these principles can be directly translated to traumatic brain injury, where pathophysiology is more complex, and the sequence of processes that affect brain water content and distribution may be different. For example, the widespread perfusion abnormalities in early head injury[7] may make it inappropriate to use contralateral brain as a "normal" control, even when this seems structurally normal. This makes the interpretation of relative CBF images much more complex. Similarly, the coexistence of low cerebral blood volume and cerebral blood flow in many patients suggests abnormal microvascular physiology, while the presence of vascular engorgement in the subacute phase can substantially increase cerebral blood volume and confound the application of algorithms that derive absolute or relative CBF maps. Finally, the experimental data suggest that ADC reductions in head injury are not always accompanied by reductions in CBF to levels that are typical of ischaemic cytotoxic oedema, and that other mechanisms may be responsible for these imaging findings.

3.3 Management of Head Injury

The emphasis of current head injury management guidelines is focused on the prevention of secondary injury.[88 89] These guidelines aim to optimise cerebral perfusion and the control of intracranial pressure.

INTRACRANIAL PRESSURE AND HYPERVENTILATION

Intracranial hypertension is traditionally defined as an ICP greater than 20 mmHg. Increased ICP will reduce CPP, unless MAP rises in parallel, and if severe, carries the risk of cerebral herniation. Above an ICP of 20 mmHg the compliance of the intracranial space rapidly decreases, such that small increases in intracranial volume produce large increases is intracranial pressure.

While ICP monitoring has never been subjected to a prospective randomized clinical trial to establish its efficacy in improving outcome from severe head injury, it provides a major target for most modern therapies in head injury management and is recommended in expert guidelines.[90] Improvements in outcome following traumatic brain injury (TBI) have been associated with management protocols incorporating ICP monitoring[91 92] and support a strong relationship between increased mortality and morbidity and raised ICP or poor ICP control.[93 94] In particular, data from the Traumatic Coma Data Bank suggest that an ICP greater than 20 mmHg is strongly predictive of a poor outcome following head injury.[94]

General measures for ICP control include control of body temperature, seizure prophylaxis, elevation of the head of the bed, avoidance of jugular venous outflow obstruction, sedation and muscular paralysis, maintenance of adequate arterial oxygenation, cerebrospinal fluid drainage, and fluid resuscitation and vasopressor support to maintain a CPP > 70 mmHg.[95] During the period of research expert guidelines were revised and recommended a lower CPP target of 60 mmHg,[96] however the hospital protocol for CPP management did not change to reflect this until after these experiments were complete. When intracranial hypertension was refractory to conventional therapy, 'second tier' therapies including hypertensive therapy to increase CPP and hyperventilation should be considered. Hyperventilation, via a reduction in $PaCO_2$, results in cerebral vasoconstriction and a reduction in CBV; a reduction of $PaCO_2$ of 1 kPa producing around a 20% reduction in CBV (figure 13).[97]

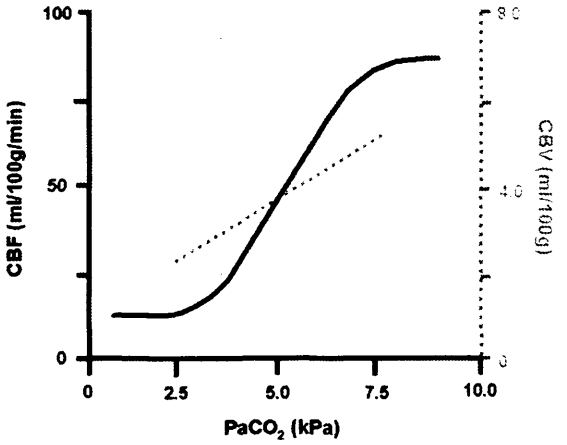

Figure 13. The effect of $PaCO_2$ on CBF and CBV. CBF and CBV change linearly with $PaCO_2$ within the physiological range. This CO_2 reactivity is affected by the duration of hyperventilation, injury and the effect of drugs; however, as an approximation, CBF falls by 10-15 ml/100g/min for every 1 kPa fall in $PaCO_2$.

Consequently, hyperventilation has been extensively used in the past for the control of intracranial hypertension in patients with TBI.[98-100] However, hyperventilation produces reductions in CBF (Fig 9).[97 101] Increasing evidence suggests the presence of early cerebral hypoperfusion (and possibly ischaemia) in patients with TBI,[4 61 102] and there are concerns that hyperventilation induced reductions in CBF may precipitate or worsen ischaemia[98 101 103] and affect outcome.[104] Such concerns have led to recommendations regarding the use of hyperventilation therapy in head injury.[105] These advocate the avoidance of hyperventilation within the first 24 hours of injury, when blood flow is commonly reduced.[4] However, they still include hyperventilation as a therapeutic option in those patients with intractable intracranial pressure during the later phases of injury.

Recent ^{15}O-PET imaging studies demonstrating no acute fall in $CMRO_2$ with hyperventilation,[106 107] contrast with others studies suggesting that hyperventilation produces acute ischaemia, seen as an increase in oxygen extraction.[101] Bedside measurement of the adequacy of CBF would allow rational use of hyperventilation. However, available methods, such as jugular bulb oximetry and TCD, are unable to reliably distinguish whether such interventions result in or worsen regional ischaemia. While hyperventilation is known to reduce cerebral perfusion, it may not result in true ischaemia.[106 107] Consequently, $PaCO_2$ levels as low as 4.0 kPa are commonly employed to treat intracranial hypertension, and this practice falls within accepted guidelines.[98] However, the safety of such therapy remains unproven.

CEREBRAL PERFUSION PRESSURE

Following head injury, cerebral autoregulation is frequently impaired (figure 14)[108 109] In addition, the autoregulatory curve may be shifted to the right.[110]

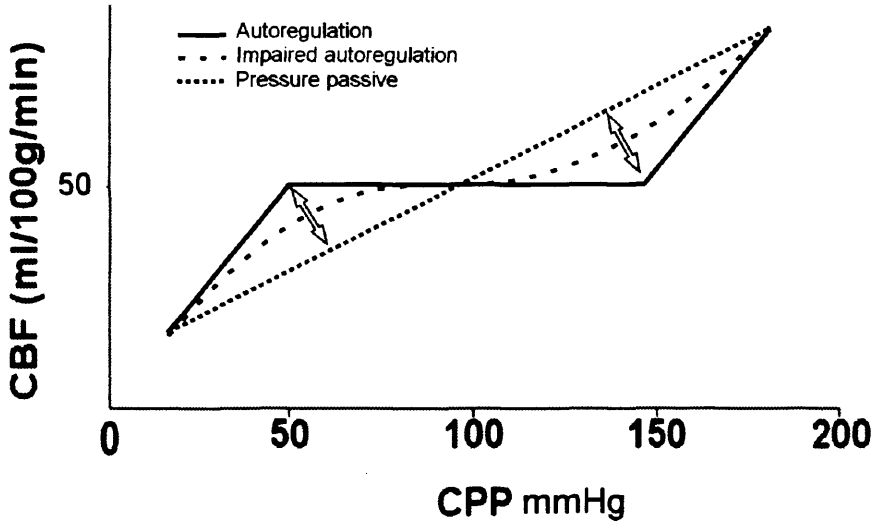

Figure 14. Autoregulation. The curves illustrating partial or complete autoregulatory impairment. The arrows show how inflection points of the curve move as autoregulation changes.

If autoregulatory mechanisms within the injured brain are impaired, then moderate reductions in CPP will reduce CBF and may lead to ischemic injury. Indeed, intact autoregulation is associated with improved outcome in head injury.[108 110-112]

Evidence of early cerebral hypoperfusion (and possibly ischaemia) in patients with TBI,[61 102] have lead some institutions to implement CPP oriented management,[113] however there is little consensus on the target level of CPP, with suggested thresholds ranging from 50 to 85 mmHg.[113 114] To achieve a sustainable increase in CPP, aggressive fluid resuscitation and hypertensive therapy such as systemic vasopressors are usually required. These treatments carry risks, including cardiac and respiratory complications.[93] Indeed, the while guidelines for the management of severe head injury published by the Brain Trauma Foundation in 2000[115] state that a CPP above 70 mmHg is a treatment option, a more recent update from the BTF suggests that CPP should be maintained above 60 mm Hg, and attempts to elevate CPP above 70 mmHg with aggressive volume supplementation and vasopressor therapy should be avoided.[96] An alternative management approach based on reducing cerebral oedema has been suggested by the Lund group in Sweden,[116] and accepts a lower minimum CPP. This approach is based on the premise that high CPP results in vasogenic oedema and intracranial hypertension. Treatment is based on the use of low dose barbiturate, metoprolol, clonidine and

dihydroergotamine. Outcome data using this approach are comparable to those from trials of CPP directed head injury management.[114] The 'Lund protocol' has not been universally accepted as a management strategy and its position requires confirmation by further controlled studies, and direct comparison with conventional therapy.

4 Methods

4.1 Clinical Protocols

All patients admitted to the neurosciences critical care unit (NCCU), Addenbrooke's Hospital, Cambridge following head injury which was significant enough to require mechanical ventilation either for airway protection because of a decreased level of consciousness (GCS<9) or for the control of raised intracranial pressure were eligible for recruitment.

All studies were approved by the Local Research Ethics Committee at Addenbrooke's Hospital, Cambridge, UK. and by the Administration of Radioactive Substances Advisory Committee of the UK.

Patients were managed with protocol driven therapy aimed at maintaining ICP below 20 mmHg and CPP greater than 70 mmHg, as previously described,[117] and detailed in the NCCU management protocol (Figure 15). Interventions included sedation (propofol up to 8 mg/kg/hr and fentanyl 1 – 2 μg/kg/hr) and neuromuscular blockade, surgery for space-occupying lesions, drainage of cerebrospinal fluid (CSF), volume supplementation and vasoactive agents (dopamine and/or norepinephrine) for CPP augmentation, osmotherapy (mannitol and hypertonic saline), and mild hyperventilation (to ~4.5 kPa). Hyperthermia was treated vigorously, and mild hypothermia (~36 °C) was commonly employed to assist ICP control.

In patients, a fibreoptic right jugular bulb catheter (Baxter, Newbury, UK) was inserted and its position confirmed radiologically. Samples of arterial and jugular venous blood were drawn for simultaneous measurement of arterial blood gases and SjO_2 and calculation of $AJDO_2$.

During imaging studies intensive care therapy and haemodynamic targets were maintained by titrating fluids and vasoactive agents, sedative infusions were left unchanged.

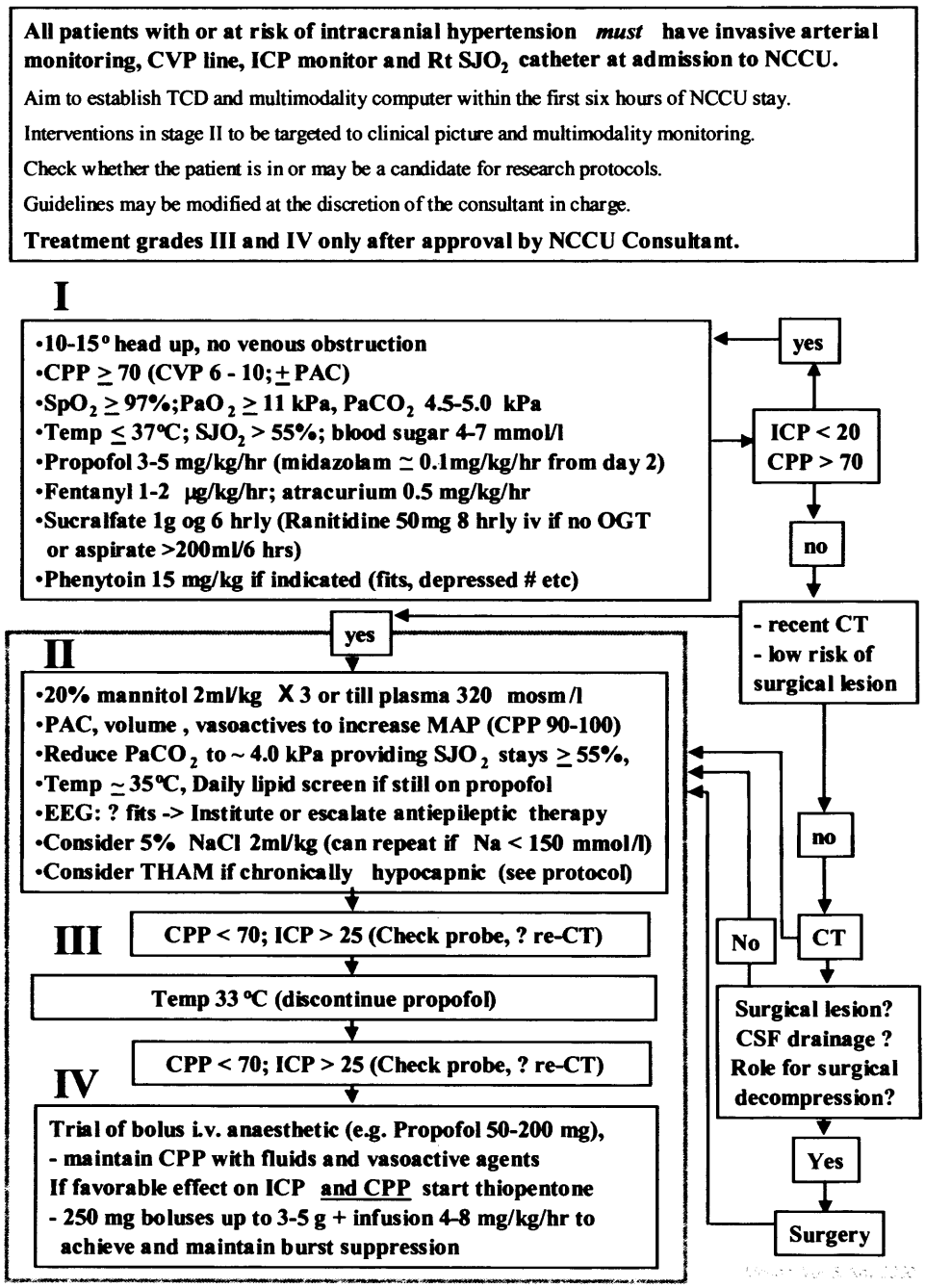

Figure 15. Addenbrooke's NCCU ICP/CPP management algorithm. NCCU: Neurosciences Critical Care Unit; CVP: central venous pressure; ICP: intracranial pressure; Rt: right; SJO_2: jugular bulb oxygen saturation; TCD: transcranial Doppler; CPP: cerebral perfusion pressure; PAC: pulmonary artery catheter; PaO_2: arterial partial pressure of O_2; $PaCO_2$: arterial partial pressure of CO_2; OGT: oral gastric tube; MAP: mean arterial pressure; CSF: cerebrospinal fluid; Rx: therapy; SpO_2 peripheral oxygen saturation; CT: computed tomography; Temp: temperature; EEG: electroencephalogram; THAM: Tris-Hydroxy-Methyl-Amino-Methane.

4.2 Three Tesla MRI Sequence Details

This section outlines the Wolfson Brain Imaging Centre (WBIC) clinical DTI sequence used for the DTI studies in this thesis and the structural images which were used for comparison and coregistration.

Three Tesla MRI All scans were performed at the WBIC on a Bruker Medspec 3 Tesla actively shielded MRI scanner (Bruker Biospin MRI, Germany). It should be noted that 3 Tesla MRI scanners are not currently in widespread use; however the higher field strength has several advantages (including importantly improved DTI resolution).

4.2.1 DTI

The DTI sequence uses an EPI acquisition to reduce scanning time and minimise motion artifact. The strength of the gradients was modulated from 0 to 30mT/m to generate the 5 b-values of 318, 637, 955, 1274, 1541s/mm^2. These b-values take into account that the gradient profile deviates from a delta shape due to the finite rise time of the diffusion gradients. The gradients were applied at all five b-values in each of the 12 directions, calculated using an electrostatic repulsion algorithm designed to maximise the separation of the individual gradients. The imaging parameters were as follows
Matrix size: 100 x 100 [reconstructed to 128x128]
Field of view: 190 x 190mm
In-plane pixel dimension: 1.9 x 1.9mm
Slice thickness: 5mm
Echo time (TE): 100ms
Repetition time (TR): 6000ms.

4.2.2 Fluid Attenuation Inversion Recovery (FLAIR) Sequence

The imaging parameters were as follows:
Matrix size: 256x512
Field of View: 168 x 358mm
Inversion Time (TI): 2213ms
Echo time (TE): 20ms
Effective echo time (ETE): 135ms
Recovery time (TR): 11190ms

4.2.3 Gradient Echo (GRE) Sequence

The GRE sequence uses paired gradients rather than spin-echo to refocus the T2 MRI signal. However T2* effects, such as those from blood, are not refocused by the gradients. Therefore tissue which contains blood appears very dark on GRE images. While in some respects this is a limitation of GRE sequences, if signal loss is seen around a contusion it implies the presence of blood. It is also therefore a useful technique for detecting small-haemorrhages associated with diffuse axonal injury. The imaging parameters were as follows:

Matrix size: 256x256

Field of view: 165 x 220mm

Recovery time (TR): 2009ms

Echo time (TE): 30ms

Flip angle: 90 degrees

4.3 PET Imaging Protocols and Image Analysis

All studies were undertaken using a General Electric Advance scanner (GE Medical Systems, Milwaulkee, USA). The standard data acquisition sequence used at the WBIC was as follows: A transmission scan for attenuation correction was performed in each patient. This was followed by a 90 second inhalation of 750 MBq of $C^{15}O$ and a single five minute frame was acquired. For calculation of CBV, blood samples were taken from an arterial line at 60 and 360 seconds. This was followed by a 20 minute inhalation of 7200 MBq of $^{15}O_2$. Two five minute emission frames were acquired during the last ten minutes of this steady state inhalation and the two frames averaged. For calculation of oxygen metabolism arterial blood samples were taken at 10, 15, and 20 minutes. Finally a 20 minute infusion of 800MBq of $H_2{}^{15}O$ was delivered intravenously. Two five minute frames of emission data were acquired in the last ten minutes of the infusion and the frames averaged. Arterial blood samples were taken at 10, 15 and 20 minutes to allow calculation of CBF.

Images were reconstructed using the PROMIS 3D filtered back projection algorithm[118] with corrections applied for attenuation, scatter, dead time and randoms. Maps of regional CBF, CBV, $CMRO_2$ and OEF were constructed using the emission data and the arterial tracer activity, as discussed in section 2.2. The maps were constructed using "in-house" PETAN software (written by Dr P. Smielewski).

4.4 Image Processing

4.4.1 Coregistration

Simply put, coregistration is the process of making the structures in a pair of images match up. However the details of this process are conceptually and mathematically complex. My research did not contain any development of these techniques. However since coregistration was used as a tool in image analysis, the principles involved will be briefly outlined.

An example of coregistration would be to take a pair of images from the same patient, for instance two MRI scans taken on different days, and align one of the image pairs so that the brain and other structures on the two images line up. The pairs of images may come from the same imaging modality or from two different imaging modalities, for instance MRI and PET. Coregistration can be used to correct for patient movement or differences in image scaling. Mathematically coregistration tries to transform voxels in the two images in order to minimise a numerical measure of mis-match (this is termed a cost function). The voxels in one of the images are then transformed such that the image rotates, changes size, stretches or tilts (or a combination of these) so that the images are a similar size and the brain structures match up. For coregistration between similar image types the image transformation is a matter of scaling, rotating, shearing, and tilting one of the images until the pairs match; this type of coregistration is called an affine transformation, an example is shown in figure 16.

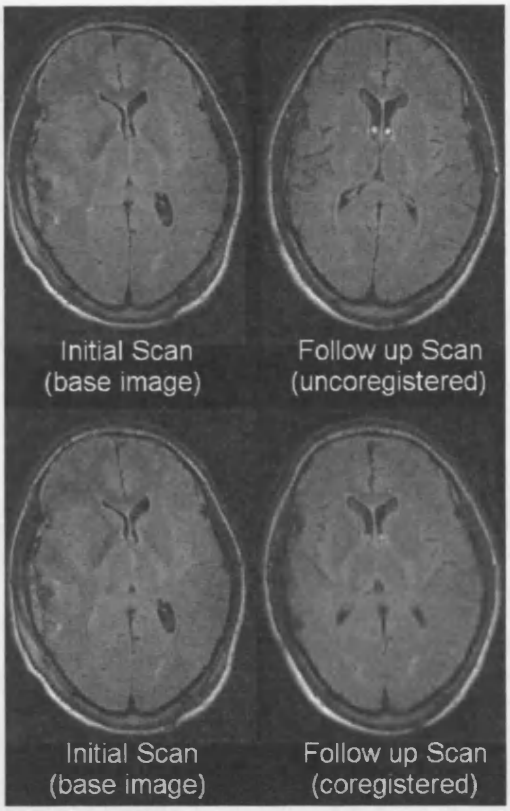

Figure 16. Affine coregistration. Top image pair showing initial and follow up MRI scans from a patient, these images are not aligned. The bottom image pair are the same images except the follow up scan is has now undergone a rigid body coregistration and the images are now aligned.

A more complex type of coregistration is termed a non-linear transformation, it is used when there are marked distortions in one of the images. Here the coregistration allows individual voxels to be moved or scaled so that different regions may undergo independent transformation. This may allow distorted regions in the image to be pulled back towards the reference image. An example is shown in Figure 17.

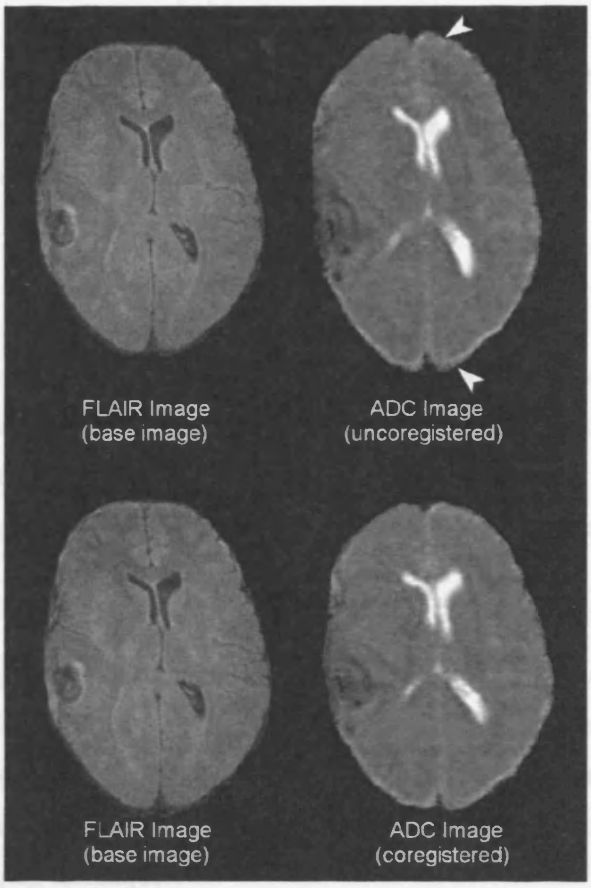

Figure 17. Top image pair show FLAIR and ADC image which are unaligned, the ADC image has different contrast and has distortions particularly in the frontal and occipital regions (arrowheads). These distortions make the brain appear elongated in the antero-posterior direction. The distortions are common in EPI sequences and are due to field inhomogeneities caused by the air tissue interface around the air sinuses. The lower image pair shows the effect of a non-rigid coregistration on the ADC Image. The images are aligned and the distortions greatly reduced.

If the image pairs have different tissue contrast but reflect the same underlying structures, a cost function such as mutual information or normalised mutual information (NMI) can be used. These cost functions minimise the error in the amount of information about underlying structure which the images share even though the contrast may differ. As an everyday example of this it would be fairly easy to pair up a photographic negative and the photo itself because the images share structural information even though they have quite different contrast.

After transformation of the image the values of the voxels require recalculation. This process is termed interpolation, and there are different algorithms which can be used for this purpose. Three commonly used interpolation algorithms are nearest neighbour, trilinear and sinc.

Nearest neighbour interpolation

This applies the value from the voxel in the original image which is nearest to the new voxel in the new image. It is the simplest method as does not alter the original values and does not smooth the image in any way, but it may result in a voxel value being duplicated if the image is enlarged during transformation.

Trilinear interpolation

This applies a weighted average value to the new voxel based on the value of the surrounding voxels in the original image. Trilinear refers to the three dimensions (x, y and z) over which the interpolation must obtain the weighted average. This type of interpolation changes the values of the voxels and smoothes the image somewhat.

Sinc interpolation

Like trilinear interpolation, this method this gives a value to the new voxel based on the surrounding voxels, but uses a sinc function to weight the various surrounding values rather than the linear weighted average. Sinc interpolation is computationally much slower than trilinear interpolation but theoretically may better relate to the underlying physics of the imaging techniques.

4.4.2 Implementation of Coregistration in Practice

For comparison between images of different types images were coregistered to the same space using the FLAIR image as a the reference image (the image to which other images were registered) with NMI as a cost function and trilinear interpolation. Since coregistration works best with images which have a high signal to noise ratio (SNR) DWI images (such as the b=0 DWI) were used for coregisteration and the transformation file created in the coregistration was then applied to coregister other images from the same data with lower SNR (such as the ADC map). An example of the contrasting SNR in images from the same acquisition are shown (Figure 18). Similarly for coregistration between PET and FLAIR the (high SNR) CBF map was coregistered and the same transformation applied to the (low SNR) CBV, OEF and $CMRO_2$ PET maps. For comparison between images of the same type (e.g. the test-retest and pre- and post-hyperventilation ADC images) the image pairs were coregistered to each other using an affine, rigid body transformation using NMI and nearest neighbour interpolation (to avoid smoothing).

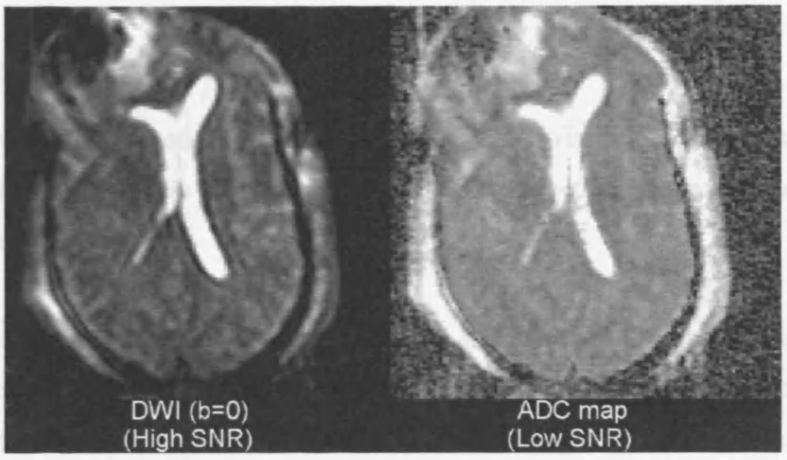

Figure 18. Image signal to noise ratio. The b=0 DWI image has the same structure as the ADC map but the high SNR makes it preferable for coregistration.

While automated image coregistration is an objective method of coregistration between pairs of images whether the registration is "good enough" remains a subjective judgment and therefore difficult to quantify. For comparison of image pairs of different types which were not distorted (e.g. PET to FLAIR) an affine, rigid body coregistration produced the best results. For comparison between images with distortions due to echo-planar acquisition (e.g. ADC images to FLAIR) it was generally necessary to use a non-rigid coregistration to achieve acceptable results, however there were some ADC images where a rigid coregistration produced a superior result to a non-rigid coregistration and in these cases the rigid coregistration was used. In all cases the decision regarding the type of coregistration used was not influenced by the results of subsequent image analysis.

4.5 Statistical Methods

Some aspects of the statistical methods used are specific to individual chapters, and are discussed in those chapters separately. This section deals with the general principles of the statistical analysis used.

Statistical analysis was performed using SPSS 11.5 (SPSS Inc., Chicago, Illinois, USA). Non-parametric data comparisons were performed using a Mann-Whitney U test and parametric comparisons were performed using an unpaired t-test or one way ANOVA with Bonferroni correction of multiple comparisons where appropriate. Linear correlations between non-parametric data were performed using the Spearman correlation coefficient.

P-values of less than 0.05 were considered significant. In the test-retest data confidence intervals of 99% were used to minimise the chance of a type 1 statistical error.
The statistical tests used in the individual studies are described in more detail in the respective sections.

5 Methodological Developments

5.1 Infusion Pump Testing at 3 Tesla

5.1.1 Introduction

Critically ill patients who are undergoing MRI often require the delivery of intravenous infusions by infusion pump, however there are concerns about the safety of such equipment in a magnetic resonance (MR) environment[119 120] Many pumps are partly or substantially constructed of ferromagnetic components and represent a projectile risk in the high strength magnetic field used for MRI, in addition some components of these devices such as the electric motor, strain gauges, micro-switches and electronic sensors could have their performance affected by the strong static magnetic field, switching magnetic gradient fields or radio frequency (RF) fields. The term 'MR safe' indicates that a device used in the MR suite it does not present any additional risk to the patient and the term 'MR compatible' indicates that a device will not affect the diagnostic quality of the imaging procedure, or have its operations affected by the MR scanning system. Such terms apply up to the limits at which the equipment was tested.[121-123] While the MR compatibility of a previous generation of infusion pumps had been documented,[124] it became likely that, over the course of these studies, these would be replaced by a newer generation of pumps. These studies were therefore undertaken to ensure that the new pumps could be used during MR studies on critically ill patients.

5.1.2 Methods

The performance of two infusion pumps, the Alaris P6000 (Part number: 6001FA3UUN2) and Alaris Asena-GH (Part number: 80023GB00) (ALARIS Medical UK Ltd.) as shown in Figure 19, were tested within the MR environment of the Wolfson Brain Imaging Centre, as part of our research programme. These pumps were chosen because they are the main pumps used on NCCU and since they are primarily constructed of foam filled plastic casing and most major mechanical components are constructed from non-magnetic aluminium alloy we believed they would present a low projectile risk.

Figure 19. Alaris infusion pumps P6000 (left) and Asena-GH (right)

All studies were performed in an MR imaging system comprising a Bruker Medspec 3 Tesla actively shielded scanner (Bruker Biospin MRI, Germany). Pump flow rate was tested using a gravimetric system, as shown in Figure 20, that has been previously described[124] and a BD 50ml disposable syringe (Becton Dickinson, NJ, USA).

The gravimetric system calculates the mean flow rate from the mass of water, of known density, collected over time. To reduce the error at the start of each measurement, while driving pressure developed in the syringe and flow rate stabilised, the pumps were operated for between five and ten minutes before the start of each gravimetric measurement. Evaporative loss from the collecting flask was reduced by a rubber bung, placed in the neck of the flask, containing an inlet tube and a narrow air vent. Pump flow rate function was tested at two static field strengths, five Gauss (the limit of fringe field) and 100 Gauss (well within the usual site of our pumps for imaging). All static magnetic field strengths were obtained from the Gauss lines map and in order to control for possible effects of magnetic field orientation all flow rate experiments were conducted with the infusion pump aligned both parallel and transverse to the direction of the main static magnetic field. Each flow rate measurement was conducted once at each field strength and orientation, the mass of water was recorded every 30 seconds and the mean flow and mean error were calculated. The tests were conducted at static field strengths of five Gauss with an infusion rate of 10ml/h (over one hour) and at 100 Gauss with infusion rates of 1ml/h (over one hour), 10 ml/hr (over one hour) and 100ml/h (over 30 minutes). In order to assess the effects of gradient and RF fields on pump performance, the accuracy of the device was tested at 100 Gauss with an infusion rate of 10ml/h (over one hour) whilst a T2 sequence using large RF frequency field pulses was run (spin-echo sequence parameters: TE - 80ms, TR - 6056ms). In order to assess the effects of long-term exposure to magnetic fields the pumps were tested at the 100 Gauss with an infusion rate of 10ml/h whilst the sequence described above was operated continuously for five hours. In all flow rate experiments a mean error of less than five percent was considered acceptable and this is in line with our hospital policy. Occlusion pressure limit alarm function was measured using a digital pressure gauge (DPI 705, Druck plc, UK). The infusion pumps have an adjustable occlusion pressure alarm, graduated from L1 to L8, and this was tested at three pressure limit levels L2 (low), L4 (medium) and L6 (high). The pressure at these levels was measured outside the field and then at two field strengths (50 and 100 Gauss), each measurement was repeated ten times to obtain a mean occlusion pressure. The gravimetric balance system and pressure gauge were sited outside the scanning room, beyond the five Gauss line. All other remaining sensors were tested at the highest field strength (100 Gauss). To assess the effect of the pumps on

image acquisition a MR phantom was imaged using a proton density/T2 weighted dual-echo sequence (sequence parameters: matrix size - 512 x 256mm, field of view - 36 x 17mm, slices - 27, TE - 20 & 80ms, TR - 6056ms). Images were obtained under three conditions, baseline with no pump present and then with the each pump operating whilst positioned by the side of the imaging couch at a static field of 100 Gauss. The images obtained with the pumps present were inspected for evidence of artifact and compared to the baseline image. The gravimetric and pressure occlusion tests were repeated away from the scanner at the end of these experiments. Finally the projectile risk was assessed by suspending the pumps from a rope at the entrance to the bore of the scanner. The horizontal force due to the magnetic field was calculated from the angle of deflection of the pumps.

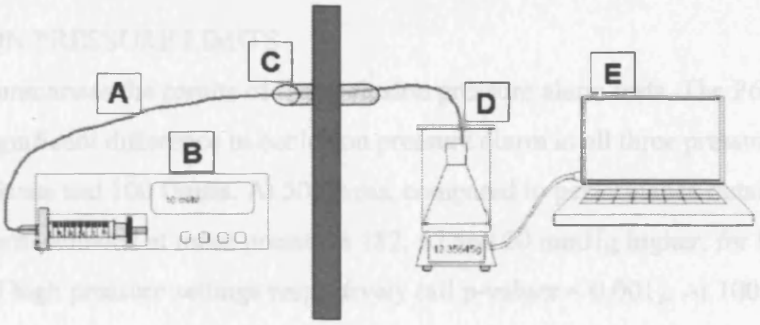

Figure 20. Diagram of the gravimetric system used to evaluate pump flow rate. Showing: A - infusion pump within the MR scanning room, B - manometer line, C - wave guide passing through the wall of the scanning room, acting as conduit for the manometer line, D - receiving flask and scientific balance, outside the scanning room and beyond the five Gauss line and E -personal computer recording the output of the balance.

Statistical Analysis

All statistical calculations were carried out using StatView 5.0 statistical software (SAS Institute Inc., Cary, NC, USA). A mean flow rate error of less than five percent was considered acceptable and this is in line with our hospitals policy for pump testing. Continuous parametric data (pressure alarm limits) were compared with paired two tailed t-tests. A p-value of less than 0.05 was considered to represent a significant difference.

5.1.3 Results

FLOW RATE

Table 5.1 and table 5.2 summarise the results of the gravimetric flow rate tests. Both infusion pumps were found to perform within acceptable limits for the gravimetric flow rate tests. The maximum mean error recorded for the Alaris P6000 was 2.18% of the set flow and for the Asena-GH was 1.42%, both well within our set limits. The variation in instantaneous error during the pump testing at 100 Gauss and 5 Gauss was no greater than the variation away from the scanner. The alignment of the pump relative to the main magnetic field did not affect flow rate performance at any field strength. The presence of switching gradient and RF fields used during the imaging sequence did not produce any additional effect on pump flow rate performance.

OCCLUSION PRESSURE LIMITS

Table 5.3 summarises the results of the occlusion pressure alarm tests. The P6000 pump showed a significant difference in occlusion pressure alarm at all three pressure settings at both 50 Gauss and 100 Gauss. At 50 Gauss, compared to performance outside the field, the alarm sounded at mean pressures 182, 62 and 20 mmHg higher, for low, medium and high pressure settings respectively (all p-values < 0.001). At 100 Gauss, compared to performance outside the field, the alarm sounded at a mean pressure of 204 and 98 mmHg higher and 24 mmHg lower, for low, medium and high pressure settings respectively (all p-values < 0.001). For the Asena-GH pump at 50 Gauss, compared to performance outside the field, the alarm sounded at a mean of 61, 12 and 8 mmHg lower, for low, medium and high pressure settings respectively (p-values <0.001, 0.002 and 0.058). At 100 Gauss, compared to performance outside the field, the alarm sounded at a mean pressure of 99, 4 and 2 mmHg lower, for low, medium and high pressure settings respectively (p-values <0.001, 0.088 and 0.619).

OTHER EFFECTS

All other safety mechanisms worked as expected up to 100 Gauss on both pumps, including the audible alarm. The sensor mechanisms fitted to the pumps were tested by enforcing an error to occur (e.g. end of travel) and did not appear susceptible to magnetic interference. The pumps were not found to cause any appreciable artifact on the proton density/T2 weighted images and no other effect on scan quality was found. Pump performance was unchanged in tests conducted after magnetic field exposure. There was no deflection of the pumps at 100 Gauss field strength. However, when suspended at the entrance to the scanner (in excess of 500 Gauss static field and one

Tesla per metre field gradient) the P6000 pump (weight 3.275kg) was deflected from vertical by 65 degrees; the horizontal force was therefore 72.1N and the Asena-GH (weight 2.466kg) was deflected by 59 degrees; the horizontal force was therefore 37.7N.

Alaris P6000

	Beyond 5 Gauss		5 Gauss		100 Gauss	
Rate (direction to field)	Mean Flow	Mean Error %	Mean Flow	Mean Error %	Mean Flow	Mean Error %
1ml per hour (parallel)					1.02	2.01
1ml per hour (transverse)					1.004	0.41
10ml per hour (parallel)	9.9	-1	10.11	1.07	10.21	2.18
10ml per hour (transverse)			9.84	-1.57	9.86	-1.38
100ml per hour (parallel)	100.57	0.58			100.5	0.52
100ml per hour (transverse)					99.87	-0.13
10ml per hour T2 sequence					10.07	0.73

Table 5.1. The results of the flow rate tests for the Alaris P6000 pump at different infusion rates, directions and static field strengths. The last row shows the results for the pump whilst a T2 weighted sequence was running for five hours to assess the effect of RF interference.

Alaris Asena-GH

	Beyond 5 Gauss		5 Gauss		100 Gauss	
Rate (direction to field)	Mean Flow	Mean Error %	Mean Flow	Mean Error %	Mean Flow	Mean Error %
1ml per hour (parallel)					0.98	-1.7
1ml per hour (transverse)					0.99	-1.3
10ml per hour (parallel)	9.99	-0.03	9.93	-0.68	10.11	1.07
10ml per hour (transverse)			10	0.05	10.14	1.42
100ml per hour (parallel)	100.5	0.53			100.7	0.65
100ml per hour (transverse)					100.5	0.53
10ml per hour T2 sequence					10.08	0.84

Table 5.2. The results of the flow rate tests for the Alaris Asena-GH pump at different infusion rates, directions and static field strengths. The last row shows the results for the pump whilst a T2 weighted sequence was running for five hours to assess the effect of RF field interference.

	P6000		Asena-GH	
	Mean Difference	p-Value	Mean Difference	p-Value
Low pressure limit (0-50 Gauss)	-182 mmHg	<0.001*	61 mmHg	<0.001*
Medium pressure limit (0-50 Gauss)	-62 mmHg	<0.001*	12 mmHg	0.002*
High pressure limit (0-50 Gauss)	-20 mmHg	<0.001*	8 mmHg	0.058
Low pressure limit (0-100 Gauss)	-204 mmHg	<0.001*	99 mmHg	<0.001*
Medium pressure limit (0-100 Gauss)	-98 mmHg	<0.001*	4 mmHg	0.088
High pressure limit (0-100 Gauss)	24 mmHg	<0.001*	2 mmHg	0.619

Table 5.3. The mean difference in the occlusion pressure limit, between 0 and 50 Gauss and between 0 and 100 Gauss for each pump. The p-values are shown. Significant differences are highlighted with an asterisk.

5.1.4 Conclusion

We have shown that the mean infusion rates and mean errors of the Alaris P6000 and Alaris Asena-GH pumps are unchanged in an MR environment up to 100 Gauss. Neither pump was affected by the RF or gradient fields used in imaging and neither pump affected image quality. The effect of the MR environment upon the occlusion pressure alarm of the P6000 pump may have safety implications since, if the set pressure limit is exceeded, a larger bolus volume could be delivered when the occlusion is released. Whilst the MR environment affected the pressure limit alarm of the Asena-GH, the occlusion pressure differences were small and their main consequence would be the alarm sounding prematurely. This is unlikely to have patient safety implications. Both pumps were deflected by the magnetic field at the entrance to the scanner and were subjected to a significant attractive force, which was greater than the force exerted on the device by gravity. However, this attractive force was only manifest close to the opening of the magnet, at a static field of over 500 Gauss and a field gradient exceeding one Tesla per metre. We have shown that the Asena-GH can function accurately and safely provided the pump is kept no closer than 100 Gauss and secured to an immovable object. However neither pump can strictly be classified as either MR safe or MR

compatible; the pumps are only likely to be able to fulfil such definitions if ferromagnetic components were reduced so that the overall translational force on the device became negligible. If such modifications are made, or the pump is used with the caveats outlined above, pump function may be affected by prolonged exposure to strong magnetic fields, and careful testing of any pump used within a MRI setting must take place regularly to ensure continued reliability.

5.2 Determination of the Test-Retest Reproducibility of DWI

5.2.1 Introduction

If ADC maps are obtained twice in an individual patient the ADC values obtained will often differ. This variability of ADC measurement is termed the test-retest variability. The reasons for non identical results are partly real changes in diffusion between the two scans, but also results from to noise in the scanning system. The limits of the test-retest reproducibility need to be defined to make judgements about the significance of ADC changes in patients. It is also needed to determine the significance of any ADC change in a group of patients undergoing a therapeutic intervention. The test-retest reproducibility of ADC values in head injured patients is as yet unreported.

5.2.2 Patients and Methods

The test-retest reproducibility was determined in a group of six head injured patients. The patients underwent two identical DTI sequences, separated by an average interval of 28 minutes, with every effort made to maintain stable physiology across the two scans. In particular, the mean change in $PaCO_2$ was 0.07kPa, and in no patient did the $PaCO_2$ change by more than 0.2 kPa. The mean change in CPP was 0 mmHg, and in no patient did the ICP or CPP change by more than ±3 mmHg. Patient characteristics are given in Table 5.4.

No.	Age (yrs)	Sex	Mechanism of Injury	Hrs. from Injury	GCS	Marshall Score	ApacheII Score	ISS	Interval (min)
1	52	F	RTA	8	4	EML	24	49	17
2	41	F	RTA	27	5	DI 2	19	21	51
3	19	M	RTA	54	8	EML	19	25	25
4	30	M	RTA	62	6	DI 3	19	30	19
5	41	M	Fall	71	6	DI 3	16	43	15
6	36	M	RTA	71	8	EML	15	16	39

Table 5.4. Patient characteristics for the test-retest reproducibility of ADC study. Marshall score[125] EML: evacuated mass lesion. The last column 'Interval' refers to the time (in minutes) between the first and second

DTI sequences and image analysis

The ADC maps were calculated, coregistered to one another and non-brain structures were excluded, The brain was manually outlined and the edge eroded by two pixels to reduce edge artifact and to ensure that the analysis was restricted to brain voxels.

Since the ADC maps are generally similar the small changes in ADC between the two can best be perceived and quantified by subtracting one map from the other. This map of the changes in ADC between the two scans was termed the delta ADC (ΔADC) map. The ΔADC map was created by subtracting the first ADC map from the second ADC map (figure 21). The ΔADC map, therefore, has negative values in areas where diffusion has decreased on the second scan and positive values in areas where diffusion has increased on the second scan.

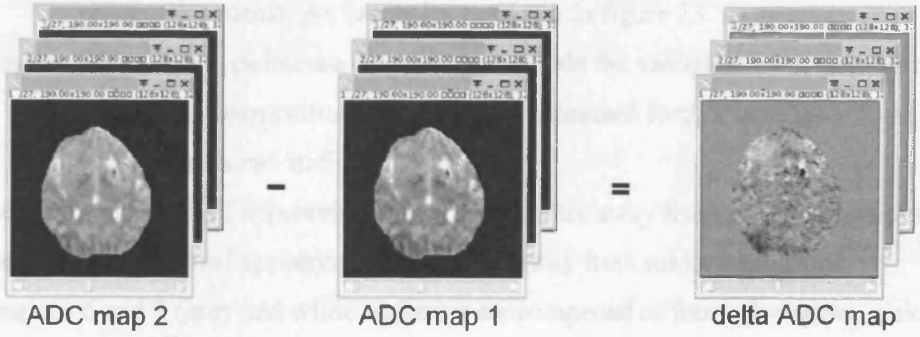

Figure 21. The calculation of ΔADC maps. The two ADC maps are coregistered and brain structures are excluded the first ADC map is subtracted from the second to create the ΔADC map.

The changes in ADC can also be standardised as a fractional change in ADC. This fractional change in ADC, relative to the ADC values in the first scan, was calculated by dividing the ΔADC map by the first ADC map to create the fractional ΔADC (fΔADC) map (figure 22).

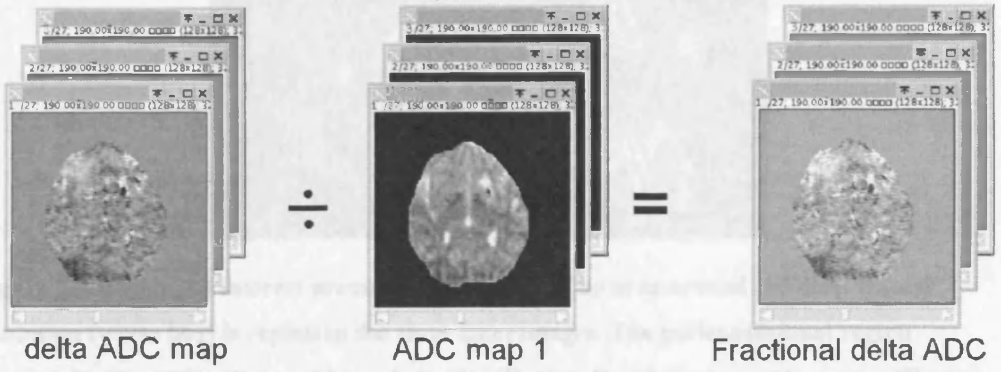

Figure 22. The calculation of fΔADC maps. The ΔADC map is divided by the ADC map from the first scan to create the fΔADC map.

ΔADC may vary between tissue types within the brain and therefore regions of interest were developed which allow the analysis of ΔADC within specific tissue types.
Seven regions of interest were developed using the first ADC map and FA maps. In all regions non-brain structures were excluded from the image analysis. The regions were:

Region 1. The whole volume (i.e. all slices).
Region 2. The two or three slices which showed the contusions most clearly.
Region 3. The pericontusional region including the core, oedema and an area of tissue approximately 3-4mm thick around the contusion. An examples is shown in figure 23
Region 4. The hyperintense region around the core of the contusion which represents vasogenic oedema. An examples is shown in figure 23
Region 5. The thin hypointense rim of tissue outside the vasogenic oedema, this region, its possible composition and origin are discussed further in chapter 5. An example is shown in figure 23.
Region 6. The normal appearing cortical grey matter away from major contusions.
Region 7. The normal appearing white matter away from major contusions.
Regions 6 and 7 (grey and white matter) were composed of four sub-regions which showed no contusions. These were defined using the FA map rather than the ADC map, since this provided better discrimination of grey from white matter (as shown in figure 24).

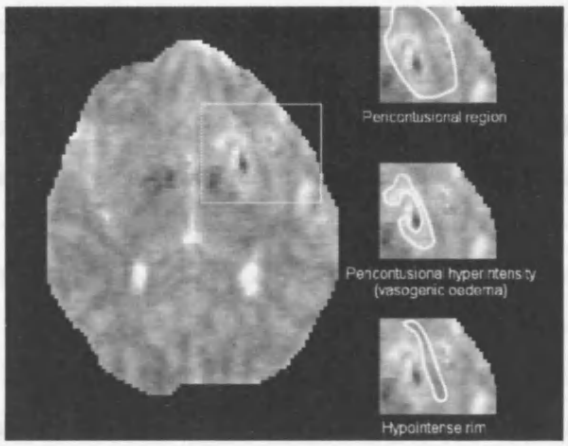

Figure 23. Regions of interest around the contusion. The area around the deep frontal contusion (white box) is copied in the three inset images. The pericontusional region (Region 3), the pericontusional hyperintensity (Region 4) and the hypointense rim (Region 5) are outlined on the insets.

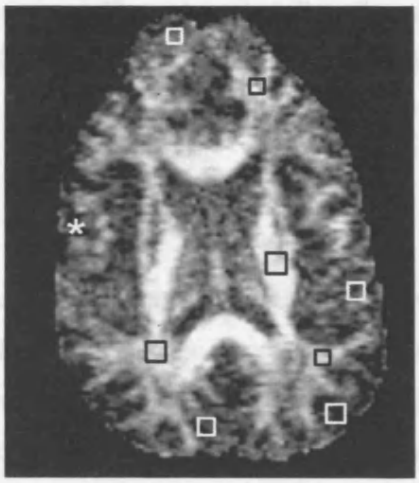

Figure 24. The FA map was used to develop the cortical grey and white matter regions of interest. Each region of interest was composed of four sub-regions of normal appearing grey and white matter respectively. Example regions of white matter (open black squares) and cortical grey matter (open white squares). Areas of contusion (white asterisk) were not included.

The seven regions were applied to the ΔADC maps and the median (50th centile), 2.5 and 97.5 centile of ΔADC values in the seven regions were calculated for each patient. The 50th centile is defined as the ΔADC value below which 50% of the ΔADC values fell. This 50th centile is therefore a useful summary measure of the overall ADC change in the regions. The 2.5 and 97.5 centiles define the ΔADC value below which 2.5% and 97.5% of the ΔADC values fell respectively. These were chosen as a measure of the more extreme ADC changes. It is important to emphasise that the 50th, 2.5 and 97.5

centiles are absolute centiles for ADC changes in an individual patient. These centiles therefore are measures of ADC change in an individual in the absence of any intervention. Summary measures of these variables would therefore define the limits of change expected in a population of patients in the absence of any intervention.

These summary measurements were calculated as follows: For each region of interest the group mean and SD for the 50th, 2.5 and 97.5 centile ΔADC values were calculated. From the mean and SD the 99% confidence intervals of the mean 50th, 2.5 and 97.5 centiles were calculated. These confidence intervals were calculated from the mean ± 2.58 standard deviations. These confidence intervals describe the likely changes that can be attributed to test-retest variability in a population of head injured patients in the absence of any intervention. The 99% confidence intervals were chosen since the small sample size increases the risk of a type 1 statistical error (i.e. incorrectly concluding that a new individual differs significantly from the group) and wide confidence intervals help to reduce the risk of such an error. These data also allow the assessment of whether a ΔADC change due to an intervention is likely to be in excess of that attributed to test-retest variability.

5.2.3 Results

The spread of ΔADC value in each of the defined the regions are shown in the histograms below which plot the percentage of voxels in each region (on the y axis) that show values within a range of ΔADC bins (plotted on the x axis). Each set of figures shows a family of histograms from individual patients. The tables beside each figure show the cut off ΔADC values, that define the 2.5, 50 and 97.5 centiles for the data, as the mean for the group as a whole, and the upper and lower 99% CI for this mean (figures 25 - 31). When assessed across the whole brain the 2.5% and 97.5% cut off values of ΔADC represented changes from baseline ADC of 20-30%.

Absolute ΔADC - All slices (region 1)

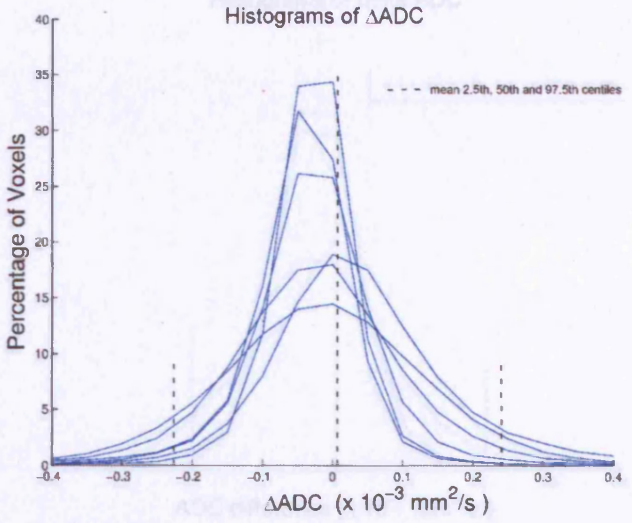

ΔADC Centile	Mean (n=6)	SD	Upper 99% CI	Lower 99% CI
2.5	-0.218	0.067	-0.044	-0.392
50	0.009	0.024	0.071	-0.053
97.5	0.239	0.123	0.556	-0.078

Figure 25. The histogram plots of ΔADC values for all slices (region 1). Individual patient histograms (left) and the combined group histogram (right). The position of the mean 2.5th, 50th and 97.5th centiles are shown. The histogram plots of are normalised for region volume such that the area under each curve is the same. The table shows the mean, SD, upper and lower 99% confidence intervals for the ΔADC centiles across all slices (region 1).

Absolute ADC changes - Contused Slices (region 2)

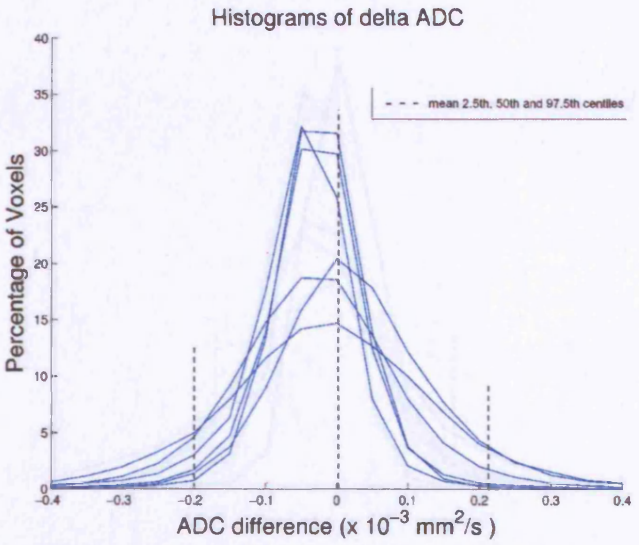

ΔADC Centile	Mean (n=6)	SD	Upper 99% CI	Lower 99% CI
2.5	-0.206	0.072	-0.02	-0.392
50	0.006	0.023	0.064	-0.053
97.5	0.222	0.113	0.513	-0.069

Figure 26. The histogram plots of ΔADC values for contused slices (region 2). Individual patient histograms (left) and the combined group histogram (right). The position of the mean 2.5th, 50th and 97.5th centiles are shown. The histogram plots of are normalised for region volume such that the area under each curve is the same. The table shows the mean, SD, upper and lower 99% confidence intervals for the ΔADC centiles across the slices most clearly showing the contusions (region 2).

Absolute ADC changes - Pericontusional Region (region 3)

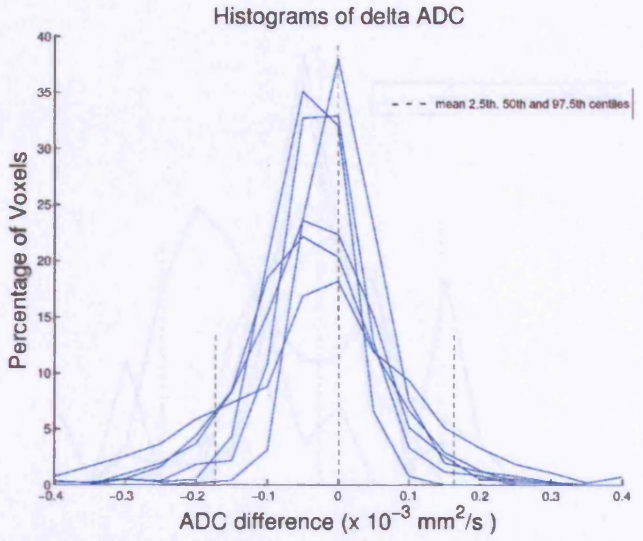

ΔADC Centile	Mean (n=6)	SD	Upper 99% CI	Lower 99% CI
2.5	-0.183	0.087	0.041	-0.407
50	0.001	0.017	0.044	-0.043
97.5	0.174	0.071	0.358	-0.01

Figure 27. The histogram plots of ΔADC values for the pericontusional region, as a whole (region 3). Individual patient histograms (left) and the combined group histogram (right). The position of the mean 2.5th, 50th and 97.5th centiles are shown. The histogram plots of are normalised for region volume such that the area under each curve is the same. The table shows the mean, SD, upper and lower 99% confidence intervals for the ΔADC centiles across the pericontusional region (region 3).

Absolute ADC changes - Vasogenic Oedema (region 4)

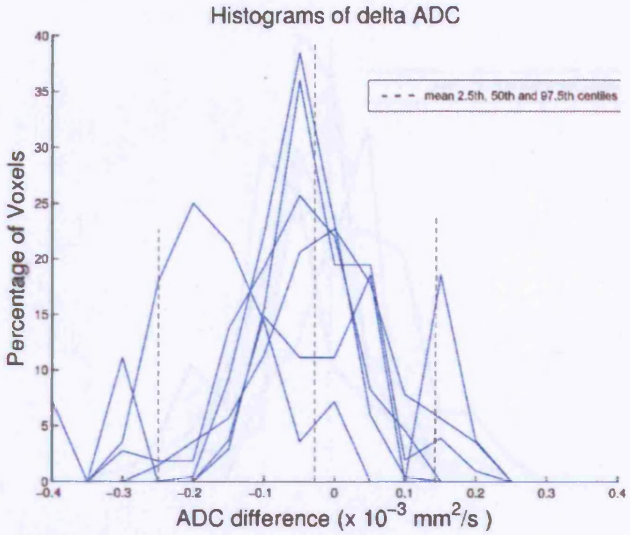

ΔADC Centile	Mean (n=6)	SD	Upper 99% CI	Lower 99% CI
2.5	-0.249	0.141	0.115	-0.612
50	-0.03	0.062	0.13	-0.19
97.5	0.138	0.074	0.328	-0.052

Figure 28. The histogram plots of ΔADC values for the pericontusional vasogenic oedema seen as ADC hyperintensity (region 4). Individual patient histograms (left) and the combined group histogram (right). The position of the mean 2.5th, 50th and 97.5th centiles are shown. The histogram plots of are normalised for region volume such that the area under each curve is the same. The table shows the mean, SD, upper and lower 99% confidence intervals for the ΔADC centiles in the pericontusional vasogenic oedema (region 4).

Absolute ADC changes - Hypointense Rim (region 5)

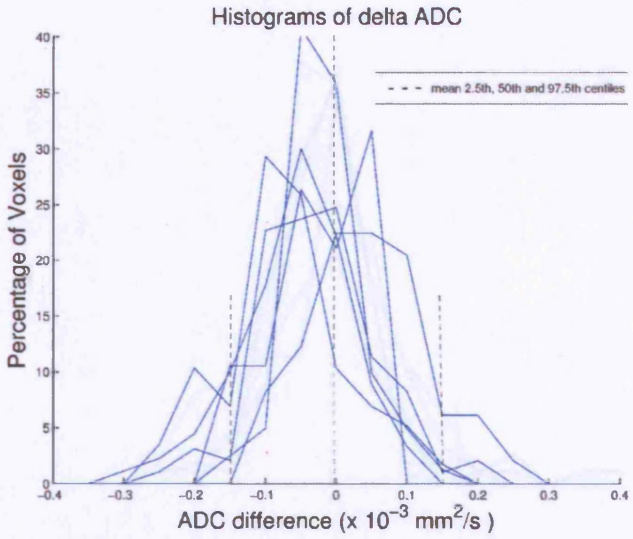

ΔADC Centile	Mean (n=6)	SD	Upper 99% CI	Lower 99% CI
2.5	-0.155	0.062	0.005	-0.315
50	-0.001	0.039	0.098	-0.101
97.5	0.151	0.06	0.305	-0.002

Figure 29. The histogram plots of ΔADC values for the pericontusional hypointense rim of tissue (region 5). Individual patient histograms (left) and the combined group histogram (right). The position of the mean 2.5th, 50th and 97.5th centiles are shown. The histogram plots of are normalised for region volume such that the area under each curve is the same. The table shows the mean, SD, upper and lower 99% confidence intervals for the ΔADC centiles in the pericontusional hypointense rim (region 5).

Absolute ADC changes - Normal Appearing Grey Matter (region 6)

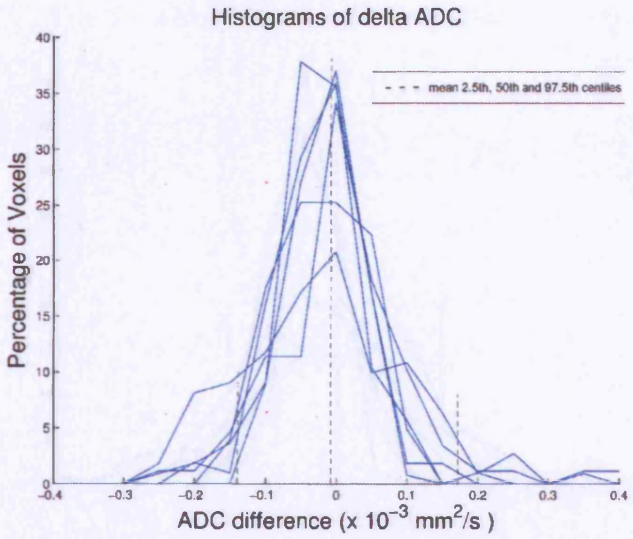

ΔADC Centile	Mean (n=6)	SD	Upper 99% CI	Lower 99% CI
2.5	-0.129	0.046	-0.01	-0.248
50)	0.012	0.012	0.043	-0.019
97.5	0.171	0.087	0.396	-0.053

Figure 30. The histogram plots of ΔADC values for the normal appearing grey matter (region 6). Individual patient histograms (left) and the combined group histogram (right). The position of the mean 2.5th, 50th and 97.5th centiles are shown. The histogram plots of are normalised for region volume such that the area under each curve is the same. The table shows the mean, SD, upper and lower 99% confidence intervals for the ΔADC centiles across the normal appearing grey matter (region 6).

Absolute ADC changes - Normal Appearing White Matter (region 7)

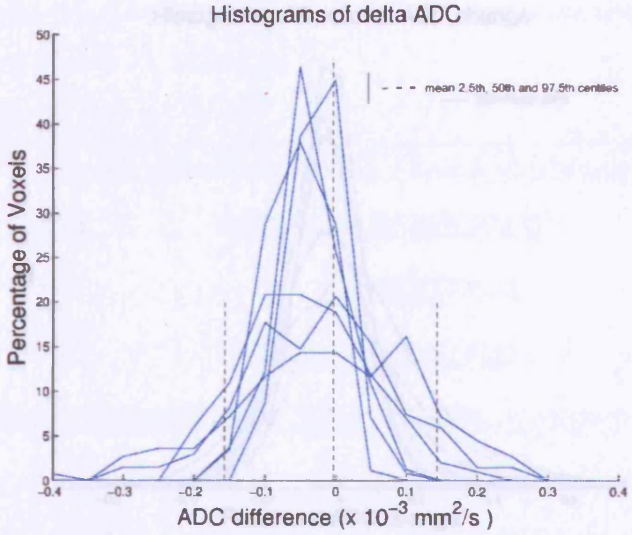

ΔADC Centile	Mean (n=6)	SD	Upper 99% CI	Lower 99% CI
2.5	-0.164	0.074	0.028	-0.355
50	-0.004	0.02	0.047	-0.055
97.5	0.142	0.086	0.364	-0.08

Figure 31. The histogram plots of ΔADC values for normal appearing white matter (region 7). Individual patient histograms (left) and the combined group histogram (right). The position of the mean 2.5th, 50th and 97.5th centiles are shown. The histogram plots of are normalised for region volume such that the area under each curve is the same. The table shows the mean, SD, upper and lower 99% confidence intervals for the ΔADC centiles in the normal appearing white matter (region 7).

Finally it is useful to provide some idea of the magnitude of ADC change in relation to baseline values. In order to do this the fractional ΔADC (fΔADC) was calculated for the whole volume of brain region1 (figure 32).

Fractional ADC changes - All slices (Region 1)

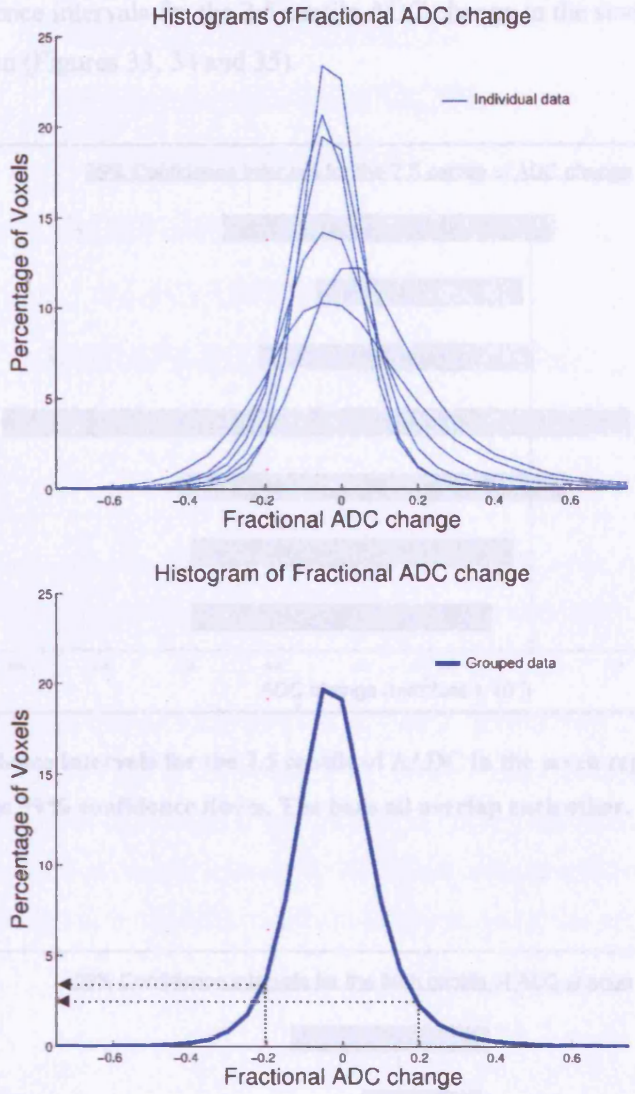

Figure 32. Individual (upper) and group (lower) histograms of fractional ADC change. The individual histograms are normalised for brain volume. The mean histogram for the patient group provides an idea of the changes in ADC relative to baseline for the study population as a whole. The dotted lines on the grouped histogram (lower) show that approximately three or four percent of voxels change by more that 0.2 (20%) of the baseline ADC value.

HETROGENEITY BETWEEN REGIONS

The 99% confidence intervals for the 2.5 centile ADC change in the seven regions of interest are shown (Figures 33, 34 and 35).

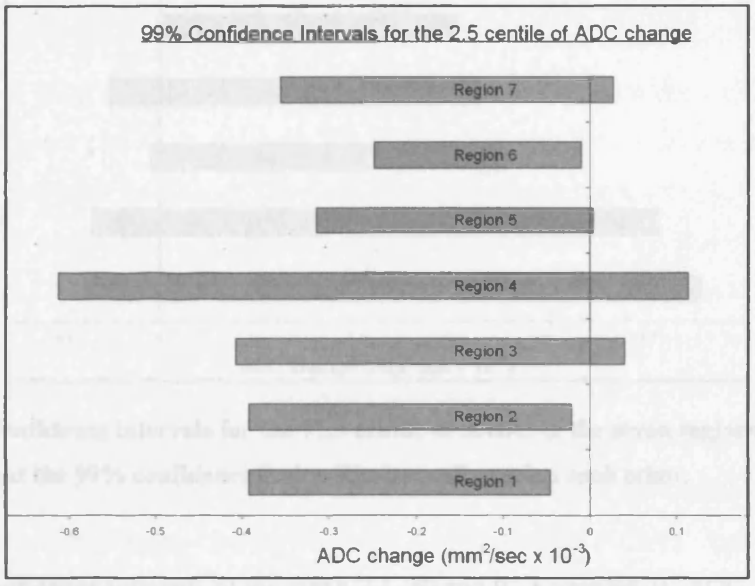

Figure 33. Confidence intervals for the 2.5 centile of ΔADC in the seven regions. The bar ends represent the 99% confidence limits. The bars all overlap each other.

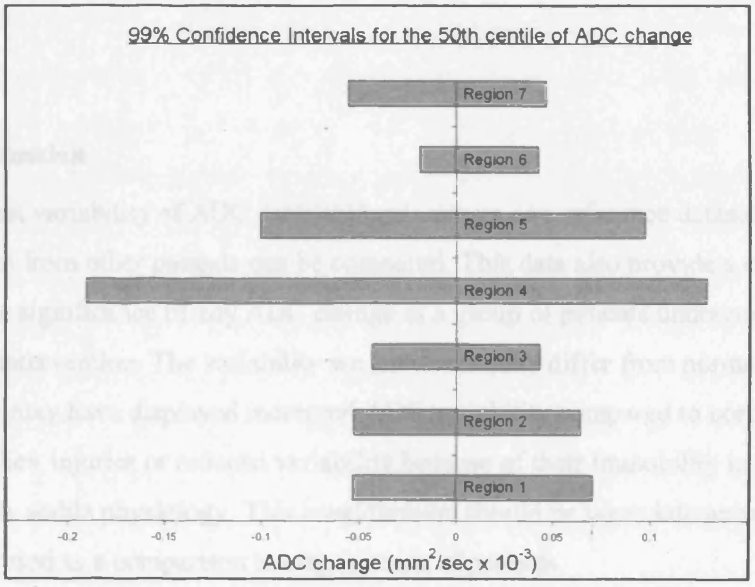

Figure 34. Confidence intervals for the 50th centile of ΔADC in the seven regions. The bar ends represent the 99% confidence limits. The bars all overlap each other.

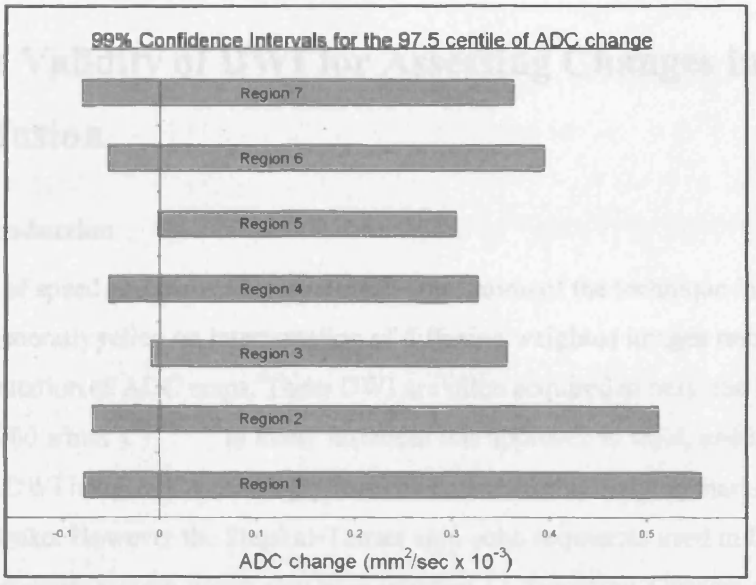

Figure 35. Confidence intervals for the 97.5 centile of ΔADC in the seven regions. The bar ends represent the 99% confidence limits. The bars all overlap each other.

The 99% confidence intervals of the mean 2.5, 50 and 97.5 centiles of ADC change (shown in figures 33, 34 and 35) all overlap. This demonstrates that the ADC variability was similar in all regions and supports the assumption that the test-retest reproducibility is broadly similar in the seven tissue regions. These data also provide limits for changes in the various percentiles of the ADC distribution that can be attributed to interscan variability.

5.2.4 Discussion

The test-retest variability of ADC measurements serves as a reference dataset against which results from other patients can be compared. This data also provide a context for assessing the significance of any ADC change in a group of patients undergoing a therapeutic intervention. The variability we have seen may differ from normal controls. The patients may have displayed increased ADC variability compared to normal controls because of their injuries or reduced variability because of their immobility in the scanner and relatively stable physiology. This consideration should be taken into account when if the data are used as a comparison to other groups of patients.

5.3 The Validity of DWI for Assessing Changes in Diffusion.

5.3.1 Introduction

For reasons of speed and convenience, clinical application of the technique in acute stroke has generally relied on interpretation of diffusion weighted images rather than actual computation of ADC maps. These DWI are often acquired at only one b value (typically 1000 s/mm^2).[32 126 127] In many instances this approach is valid, and high signal intensity on DWI images is increasingly recognised as a useful imaging marker of acute ischaemic stroke. However the Stejskal-Tanner spin-echo sequences used in DWI sequences produces images which also have intrinsic T2 weighting. Consequently the interpretation of high signal intensity on DWI can be confounded by tissue with a long T2 (as occurs in subacute stroke due to vasogenic oedema). DWI in this situation shows high signal intensity which is not the consequence of restricted diffusion associated with cytotoxic oedema. This confounding effect may result in tissue with a high T2 (classically resulting from late vasogenic oedema) to be misdiagnosed as showing cytotoxic oedema (classically resulting from early ischaemic cell swelling). This phenomenon is commonly termed "T2 shine through".[128-130] Calculation of the ADC map can avoid this confound. However, there is little recognition of the fact that changes in T2* properties of tissue may also be a significant confounder in this setting. Acquisition schemes for DWI typically utilize echo-planar imaging (EPI) and may inherently elicit substantial T2* contrast.[85] Reductions in T2*, which may be the consequence of local haemoglobin desaturation or microhaemorrhages, reduce signal intensity on DWI and leads to the underdetection of cytotoxic oedema on DWI images. As with T2 shine through, this confound can be avoided by formal calculation of ADC. There are good physiological arguments to suggest that this phenomenon is important. Haemoglobin desaturation is commonly observed in ischaemic tissue, as oxygen extraction fraction increases to compensate for reductions in blood flow.[131] When the infarction process is complete, oxygen extraction fraction falls, but during the process of evolving infarction, or in the presence of physiological heterogeneity, where small islands of compensated and decompensated tissue contribute to an imaged voxel.

5.3.2 Results

We have termed this phenomenon "T2* shade back" and have observed it following head injury, where there may be reductions in ADC in regions that show little or no increase in intensity on raw DWI images (Figure 36 and 37). Perfusion imaging with PET shows perilesional hypoperfusion in these regions (Figure 38) suggestive of ischaemia.

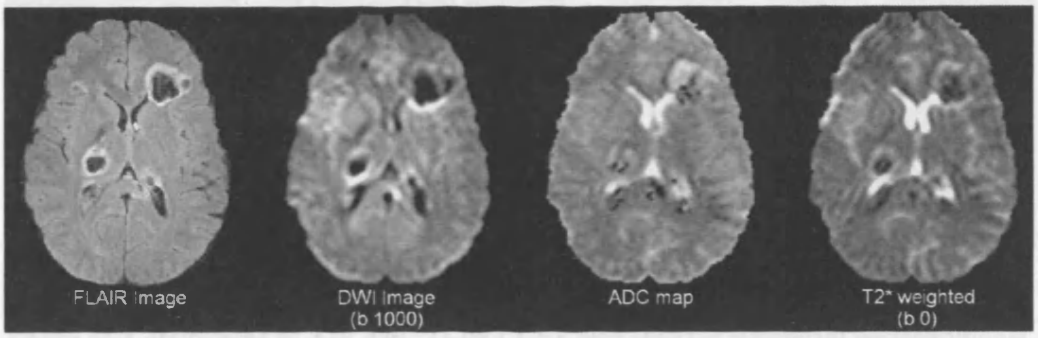

Figure 36. Co-registered images from left to right FLAIR, DWI (b=1000 sec/mm^2 EPI acquisition), ADC map and T2* weighted image (DWI, b=0 sec/mm^2 EPI acquisition)

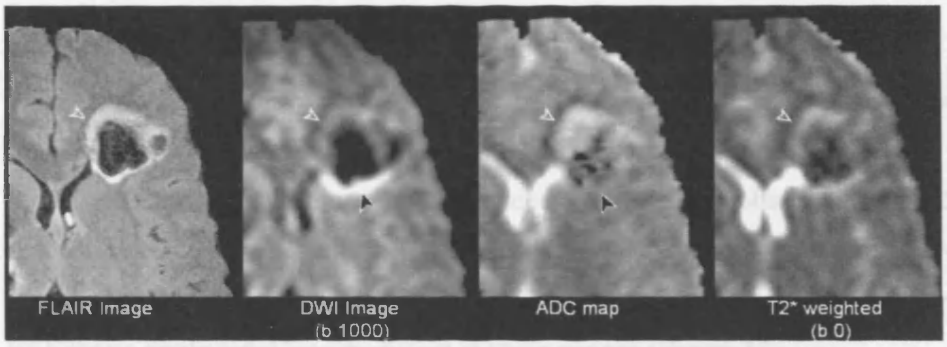

Figure 37. Detail from figure 36. Showing T2* dark back on T2* weighted image which can also be seen on DWI (co-localised open whiter arrowheads). Inspection of the area on DWI marked by the open white arrowhead, without consideration of T2* effects, would lead to the belief that diffusion in this area was increased whilst in fact the co-localised arrowhead on the ADC map shows the opposite. T2 shine-through is also present on the DWI where the ADC values are in fact normal, co-localised black arrowheads on the DWI and ADC map.

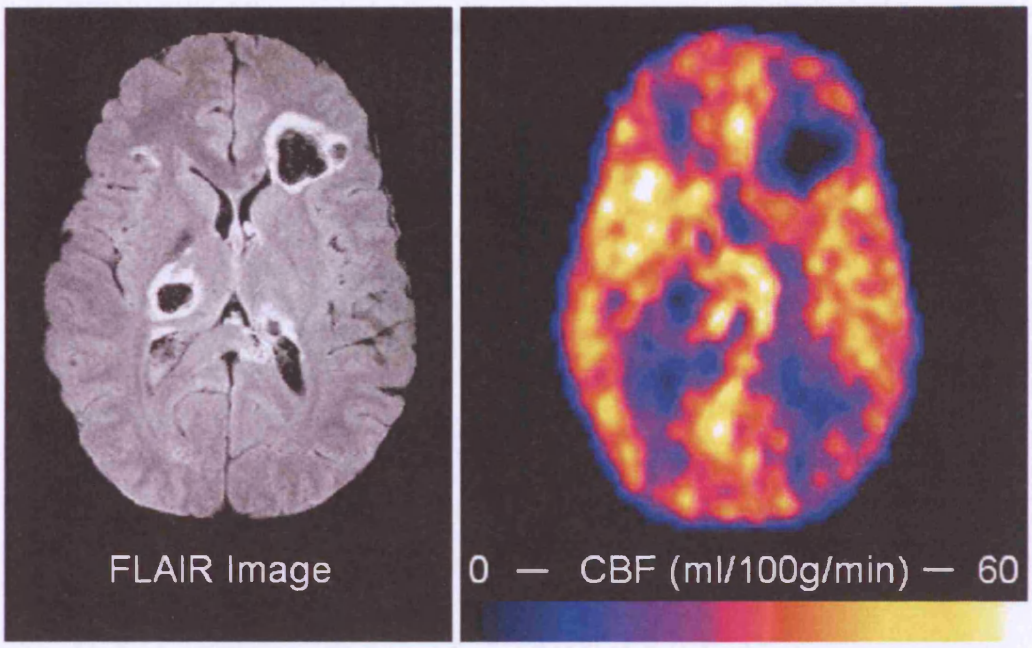

Figure 38. Coregistered FLAIR and ^{15}O-PET CBF map showing significant pericontusional hypoperfusion extending beyond areas of pericontusional hyperintensity visible on the FLAIR image.

5.3.3 Discussion

These data show that there may be discrepancy between DWI and ADC measures in some regions where T2* changes result in signal degradation on DWI.
We have termed this phenomenon "T2* shade back". We have observed these T2* shade back changes in patients following head injury, where regions of reduced ADC show little or no increase in intensity on raw DWI images, and perfusion imaging with PET shows perilesional hypoperfusion in these regions (Figure 38).

In the setting of head injury, the observed discrepancy may be due to ischaemia,[7] or to microhaemorhages that are too small to be recognised on structural imaging.[5] The T2* effects responsible for the phenomenon may be seen on gradient echo images with T2* weighting such as that obtained with EPI. The phenomenon is also likely to be important in other settings, such as acute stroke, where compensated ischaemia and haemoglobin desaturation may coexist with metabolic compromise and established infarction within a volume too small to be resolved by clinical imaging. A similar process has been cited as a possible mechanism for signal changes observed in the core of intracerebral haemorrhage,[132] but the phenomenon has not, to our knowledge, previously been described in ischaemia. This observation clearly has relevance to the interpretation of DWI changes in ischaemia and also underlines the general need to understand the basis

of signal changes in MRI in order to make rational inferences regarding underlying pathology.[133]

5.4 Can FLAIR Assess Pericontusional Oedema?

5.4.1 Introduction

FLAIR images are CSF nulled and have T2 weighting (as described in section 2.1.2). Hyperintensity on FLAIR images is generally thought to reflect increased extracellular tissue water, or in the case of pathology, vasogenic oedema. Vasogenic oedema is thought to have a high ADC. If FLAIR hyperintensity were an accurate representation of high ADC, it might be possible to use this more widely available technique to provide a useful surrogate for tissue with a high ADC. However, no direct comparison has been undertaken, and the ADC characteristics of tissue which is hyperintense on FLAIR are unknown. By comparing coregistered FLAIR and ADC images the nature of the oedema in the FLAIR hyperintensity can be investigated.

5.4.2 Methods

Images were acquired using FLAIR and DWI sequences and coregistered as previously described in section 4.4. A qualitative assessment of the congruence between the FLAIR images and the calculated ADC maps was undertaken.

5.4.3 Results

Examination of the coregistered FLAIR image and ADC map revealed substantial differences between the two (see below). These large differences preclude the use of FLAIR as an adequate modality for defining vasogenic oedema and no quantitative assessments of the degree of discrepancy were made. Specifically the ADC values within FLAIR hyperintensity showed marked heterogeneity. ADC increases, reflecting vasogenic oedema, dominated around some contusions (Figure 39) and ADC decreases, typical of cytotoxic changes, were dominant in others (Figure 40). In some contusions a mixture of ADC increases and decreases were seen (Figure 41).

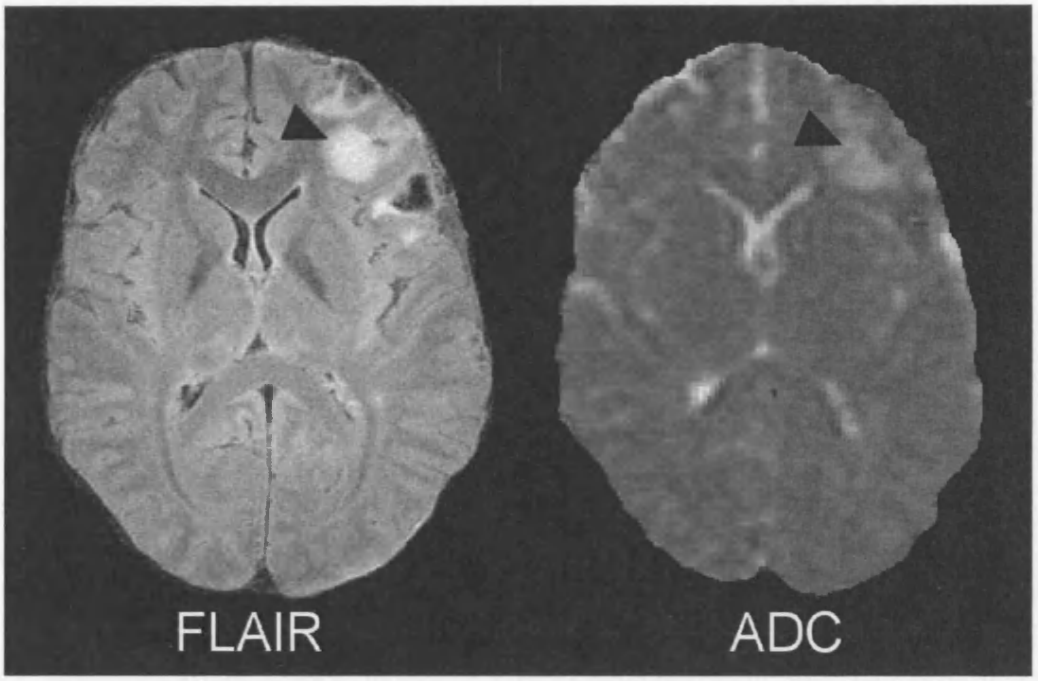

Figure 39. FLAIR hyperintensity associated with increased ADC.values.

FLAIR (left) and ADC map (right) obtained at 3 Tesla from a patient 22 hours post head injury. The T2 hyperintensity in the left frontal contusion is associated with an increased ADC, typical of vasogenic oedema.

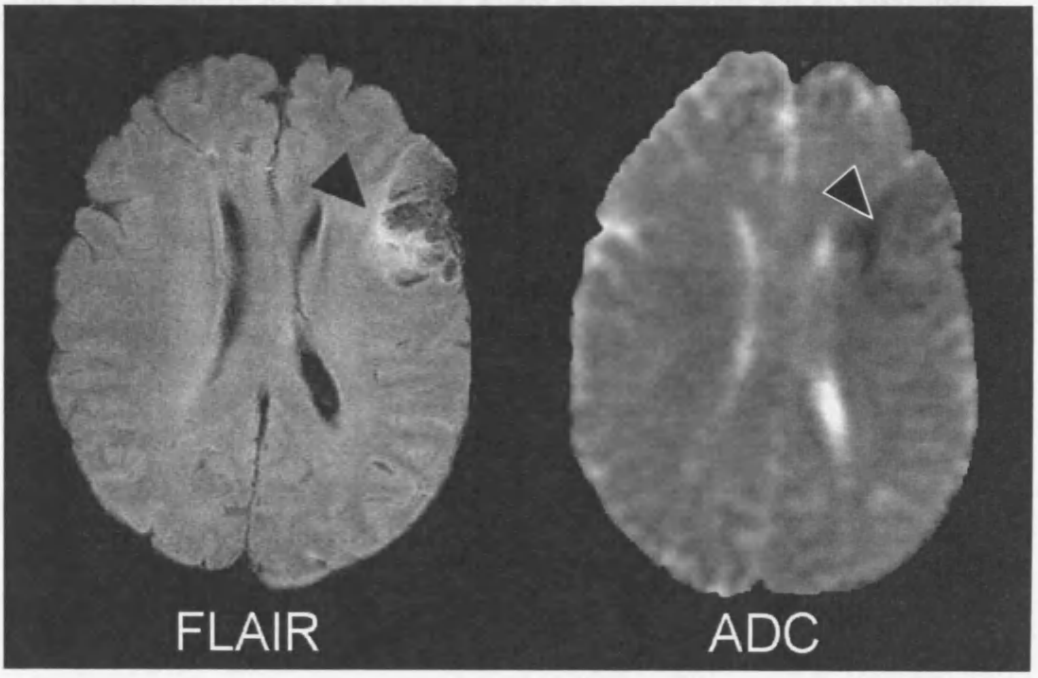

Figure 40. FLAIR hyperintensity associated with reduced ADC values

FLAIR (left) and ADC map (right) obtained at 3 Tesla from a patient 34 hours following head injury. The T2 hyperintensity in the left frontoparietal contusion is associated with a decreased ADC, typical of cytotoxic oedema.

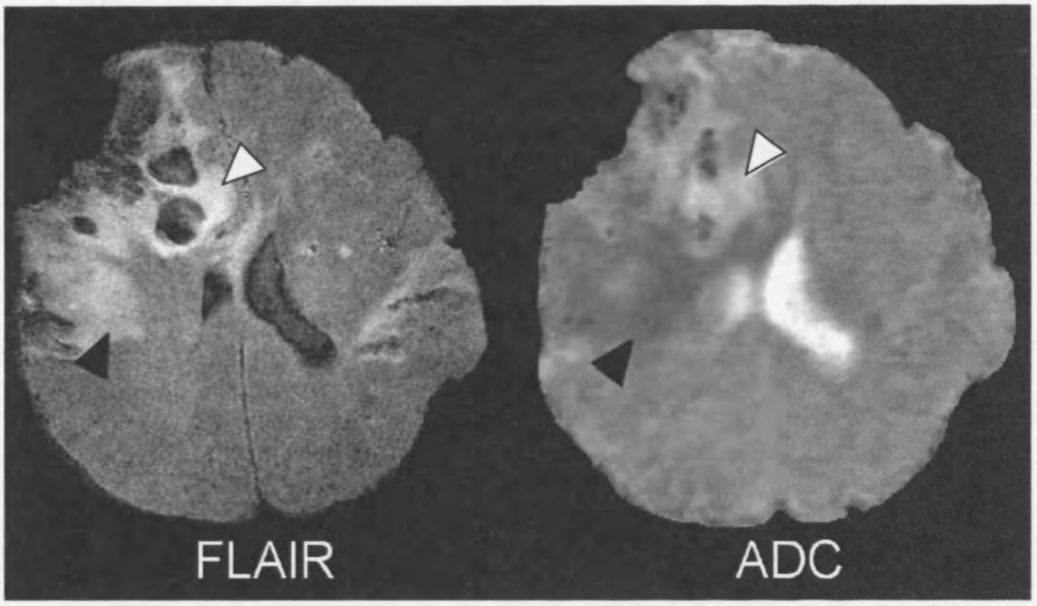

Figure 41. FLAIR hyperintensity associated with mixed ADC values

FLAIR (left) and ADC map (right) obtained at 3 Tesla from a patient 59 hours following head injury. The T2 hyperintensity in the large right sided contusion is associated with areas of both increased ADC (white arrowhead) and decreased ADC (black arrowhead). This heterogeneity of ADC, particularly within large contusions, was not uncommon.

5.4.4 Discussion

The example images (Figures 39 - 41) demonstrate hyperintensity on FLAIR cannot reliably predict the type of oedema which is present in the tissue. The coexistence of cytotoxic and vasogenic oedema within the FLAIR hyperintensity (as seen in figure 41) may be the result of two separate mechanisms of secondary damage, such as BBB disruption and ischaemia, or may reflect the same mechanism of damage at two stages during its evolution. In either case the importance of calculating the ADC map in understanding the pericontusional tissue is underlined.

6 Characterising Contusional Injury

6.1 ROI Based Characterisation of ADC Images

6.1.1 Introduction

Earlier chapters have highlighted the possible advantages of using ADC maps to characterise pathophysiology following head injury. The clinician caring for head injured patients could use these imaging data to obtain insight into the amount and type of oedema which forms around head injuries. However, the preliminary analysis of ADC values around traumatic contusions suggested that there was substantial heterogeneity in the ADC appearances of these lesions. This chapter describes the pattern of ADC change around contusions and, since they may provided clues to the underlying physiology, the mechanisms involved in the formation of these ADC changes are discussed.

The contusion and the surrounding tissue, termed the pericontusional region, has mixed composition. Contusions typically contain blood and blood breakdown products as well as injured brain tissue. The tissues in and around the contusion becomes swollen as oedema forms and inflammatory cells enter the tissue. The composition of individual contusions will vary and yet most contusions have a characteristic pattern. Contusions typically consist of a central core containing haematoma or haemorrhagic brain tissue and this core is surrounded by inflamed and swollen tissue.

On ADC maps the pattern is characteristic; contusions demonstrate a dark core of low diffusion surrounded by an area of increased diffusion which in turn is surrounded by a rim of reduced diffusion.[10 11] The terminology used in these referenced articles may require some clarification. The authors of these studies exclude the central haemorrhage from analysis and use the term "core" to describe the ADC hyperintensity around the haemorrhage. This contrasts with the of the term "core" in this thesis to define the central haemorrhage.

6.1.2 Methods

Patients were studied if they had sustained a head injury which was significant enough to require the mechanical ventilation. MRI scans were obtained on 30 patients and the ADC maps were constructed and analysed. Patient details are shown in table 6.1.

No.	Age (years)	Sex	Mechanism of Injury	Hrs. from injury	GCS	Marshall Score	Apache II Score	ISS
1	41	M	RTA	17	8	EML	16	25
2	27	M	RTA	56	10	DI 2	13	16
3	56	M	Fall	59	3	DI 3	16	29
4	41	M	Fall	71	6	DI 3	16	43
5	27	M	RTA	15	3	DI 4	19	27
6	21	F	RTA	46	7	DI 2	14	26
7	40	M	RTA	85	3	DI 3	18	38
8	39	M	RTA	9	4	DI 2	25	21
9	31	F	Fall	15	3	DI 2	18	9
10	29	M	Fall	21	10	NEML	20	26
11	27	M	Assault	15	4	NEML	28	27
12	00	M	RTA	71	8	EML	15	16
13	17	M	RTA	22	5	DI 3	18	32
14	22	M	Assault	53	3	DI 2	21	16
15	70	F	Fall	40	8	DI 2	19	16
16	20	M	Assault	57	7	DI 4	11	16
17	38	M	RTA	28	8	DI 2	16	10
18	19	M	RTA	54	8	EML	18	25
19	20	M	Assault	38	7	DI 3	20	16
20	52	F	RTA	8	4	EML	24	49
21	23	M	Assault	104	4	EML	11	26
22	37	M	Fall	30	3	DI 2	15	25
23	46	M	Fall	134	4	DI 3	20	25
24	32	M	Assault	121	12	DI 4	5	9
25	57	M	Fall	42	8	DI 4	18	48
26	38	F	Fall	38	7	DI 4	15	27
27	30	M	RTA	62	6	DI 3	19	30
28	41	F	RTA	27	5	DI 2	19	21
29	18	M	RTA	22	9	DI 3	13	14
30	35	M	RTA	22	4	DI 3	23	25

Table 6.1. Patient characteristics for the analysis of pericontusional regions. Marshall score[125] EML: evacuated mass lesion, NEML: non evacuated mass lesion, DI: diffuse injury score.

To characterise the nature of the pericontusional regions four distinctive regions of interest were defined on each ADC image. The ADC values within these regions were then analysed. The composition of the tissue in these regions was explored by comparison to other imaging sequences.

These regions were:
Region 1. The haemorrhagic contusion core.
Region 2. The pericontusional hyperintensity surrounding the core
Region 3. The hypointense rim of tissue beyond Region 2.
Region 4. An area of normal appearing brain away from the contusion.
An example of these four regions is shown in Figure 42.

In patients in whom more than one contusion was present, the regions were defined around the largest contusion in each subject. The analysis of one contusion from each patient ensured the independence of data. The four regions were outlined on the axial image slice where the selected contusion was largest and most apparent, the area and mean ADC within each region was then calculated. The brightness and contrast of the ADC images were standardised to provide a dynamic range between 4 and 10 x 10^{-4} mm^2/sec. The four regions were manually outlined without knowledge of the time from injury to imaging. The region of normal brain was identified in the contralateral hemisphere avoiding structures such as the cerebral ventricles or obviously abnormality, this region was of constant shape, and contained contributions from grey and white matter in proportions that were broadly similar to the regions sampled in the contused hemisphere.
The ADC image analysis was performed using ImageJ software (ImageJ, NIH, Bethesda, MD).

Comparison of ADC with FLAIR and GRE
The appearances on coregistered FLAIR and GRE images were compared with the ADC maps in order to obtain insights into the pathology responsible for the imaging findings. However, since T1, T2 or T2* maps were not obtained no quantitative comparisons between these images and the ADC maps were made.

6.1.3 Results

The relative areas of the four regions varied between individuals, however all sampled contusions showed the typical four regions. The mean ADC and area of each of the four regions are shown in is show in figures 42, 44 and table 6.2

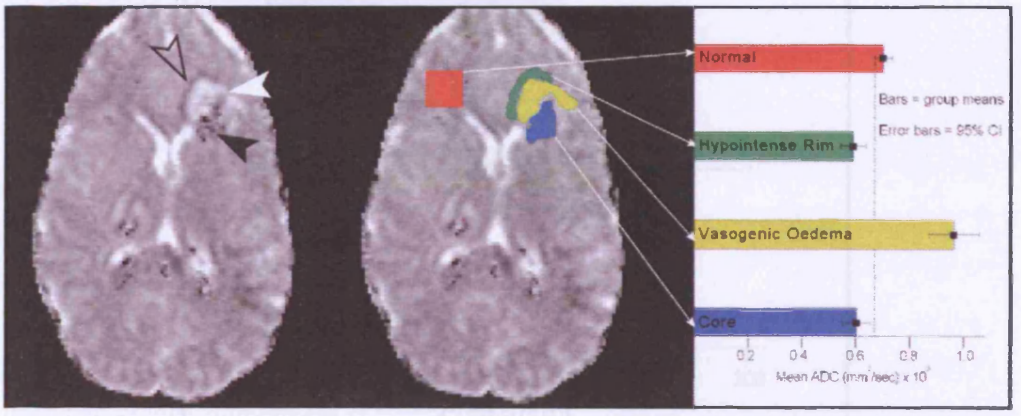

Figure 42. The ADC map from a patient showing a left frontal contusion which demonstrates a contusional core (black arrowhead), pericontusional hyperintensity (white arrowhead) and hypointense rim (open arrowhead). The image on the right shows these regions outlined. The arrows connect the regions to the bar chart. The bars indicate the mean ADC in these regions for the group of 30 patients and the 95% confidence intervals of the means are shown. The dotted line demonstrates the lower 95% confidence limit for the mean ADC in the normal regions. (n.b. There is a second smaller contusion visible in the right basal ganglia.)

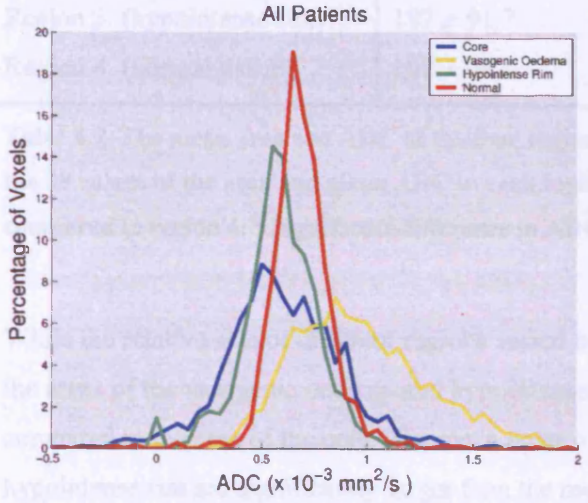

Figure 43

Histogram plots of ADC values in the four regions. These histograms represent combined data from the 30 patients. The histograms are normalised for region size between individuals and between regions.

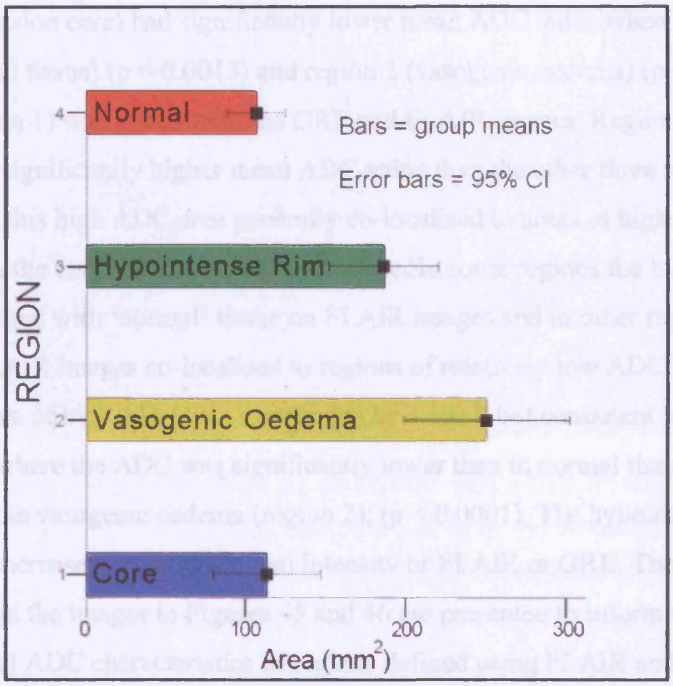

Figure 44. Bar chart showing the mean area of each of the four regions from the 30 patients. 95% confidence intervals are shown.

	Area ± SD (mm^2)	ADC ± SD (mm^2/sec x 10^{-3})
Region 1. (core)	114 ± 90.0	0.603 ± 0.136 * †
Region 2. (vasogenic oedema)	251 ± 138.7	0.963 ± 0.25 *
Region 3. (hypointense rim)	187 ± 91.7	0.591 ± 0.129 * †
Region 4. (normal tissue)	107 ± 48.5	0.701 ± 0.088 †

Table 6.2. The mean area and ADC of the four region of interest. The values are means of the 30 values of the area and mean ADC in each region. * Significant difference in ADC compared to region 4. † Significant difference in ADC compared to region 2.

While the relative size of different regions varied between subjects, it is noteworthy that the areas of the vasogenic oedema and hypointense rim were similar to each other, when compared to the area of the core. The mean areas of both the vasogenic oedema and the hypointense rim are significantly larger than the mean area of the core. Across all 30 subjects, the combined mean area of the vasogenic oedema and hypointense rim was 3.85 times the area of the core. This combined region may represent a "contusional penumbra" and a possible site of secondary ischaemic injury.

Region 1 (contusion core) had significantly lower mean ADC value when compared to region 4 (normal tissue) ($p = 0.0013$) and region 2 (vasogenic oedema) ($p < 0.0001$). This core (region 1) was hypointense on GRE and FLAIR images. Region 2 (vasogenic oedema) had a significantly higher mean ADC value than the other three regions ($p < 0.0001$). While this high ADC area generally co-localised to areas of high signal on FLAIR images, the concordance was not complete. In some regions the high ADC values co-localised with 'normal' tissue on FLAIR images and in other regions high intensity on FLAIR images co-localised to regions of relatively low ADC (Fig). In all subjects, the area of high ADC was surrounded by a small but consistent hypointense rim (region 3) where the ADC was significantly lower than in normal tissue (region 4) ($p = 0.0006$) and the vasogenic oedema (region 2); ($p < 0.0001$). The hypointense rim co-localised with increased or normal signal intensity or FLAIR or GRE. These observations and the images in Figures 45 and 46 are presented to inform the reader about the typical ADC characteristics of regions defined using FLAIR and GRE images. The FLAIR and GRE images are not quantitative maps and therefore numerical data from these regions has not been obtained.

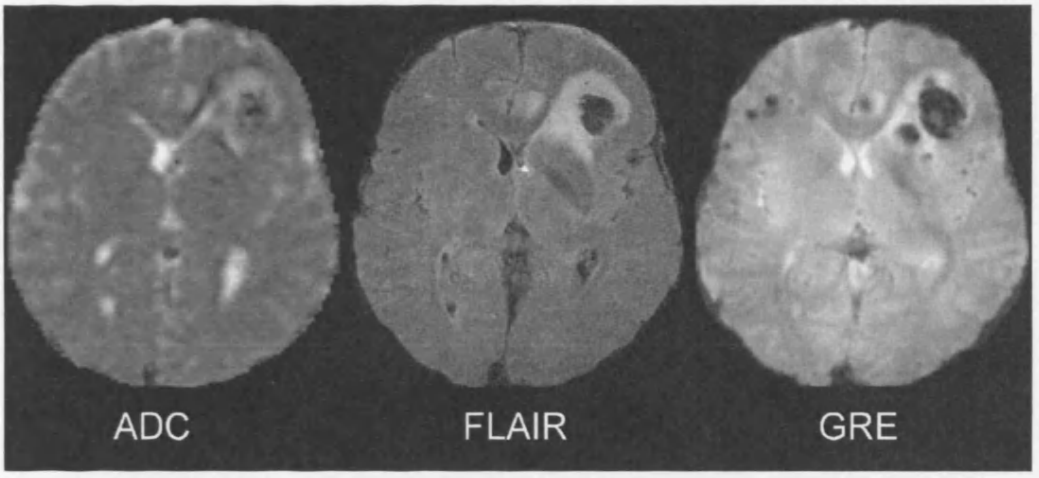

Figure 45. Coregistered image sets from a patient imaged 21 hours after injury. ADC image (left), FLAIR image (middle) and GRE image (right). A large left frontal contusion with a hypointense core is shown on all three image sequences, indicating the presence of haematoma. The hyperintensity surrounding these core regions is uniform on FLAIR images but of mixed density on the ADC images, this is a common finding and demonstrates that tissue with T2 hyperintensity may have heterogeneous diffusion characteristics. The hypointense rim of tissue outside this hyperintensity is seen on ADC but is absent on GRE, excluding haematoma as a cause of this hypointensity.

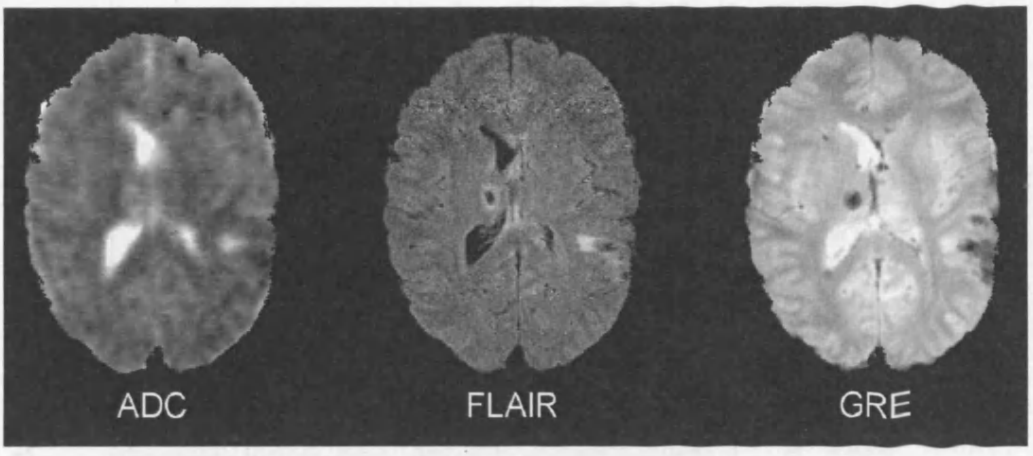

Figure 46. Coregistered image sets from a patient. ADC image (left), FLAIR image (middle) and GRE image (right). The left parietal contusion and right mid brain contusions show a hypointense core on all three image sequences. The hyperintensity surrounding the core regions is uniform on FLAIR and ADC images and demonstrates that, in this patient, the T2 hyperintensity is primarily due to vasogenic oedema. The hypointense rim of tissue outside this hyperintensity is seen on ADC but is absent on GRE, excluding haematoma as a cause of this hypointensity.

The area and ADC of each region was correlated against the interval between the injury and the MRI scan. The scatter plot of region area against time since injury is shown in Figure 47. The scatter plot of ADC against time since injury is shown in Figure 48.

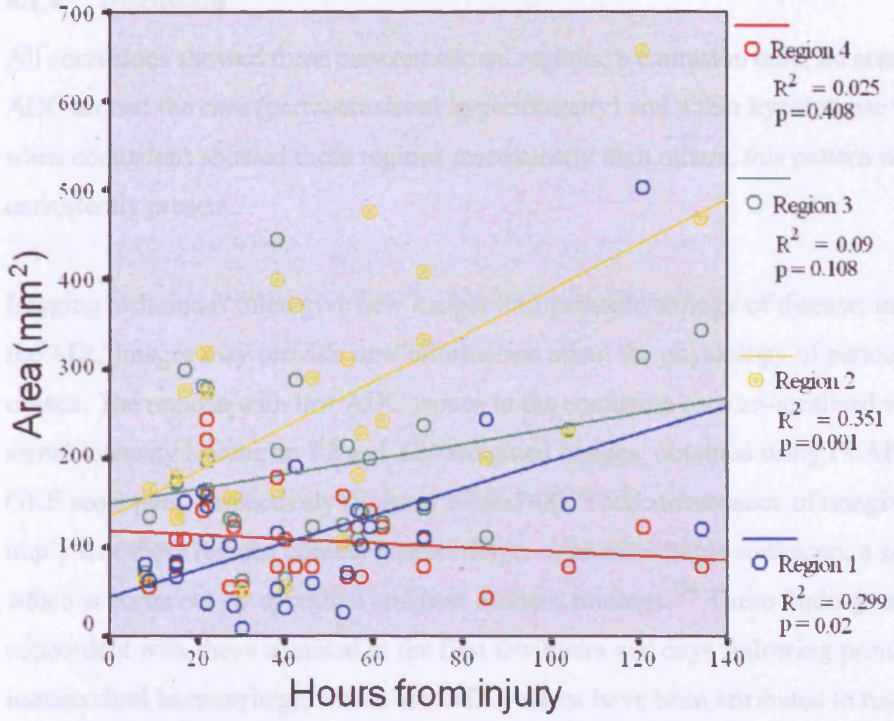

Figure 47. There was a significant correlation between area and time since injury in regions 1 and 2 ($p<0.05$). The R^2 value for this correlation is 0.29 in region 1 and 0.35 in region 2.

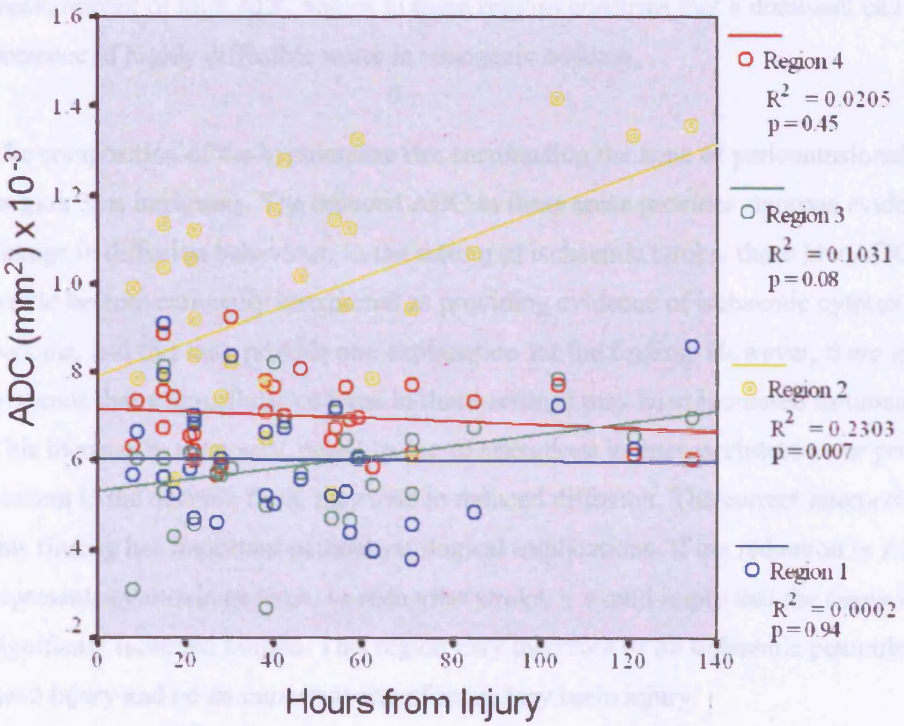

Figure 48. There was a significant correlation between ADC and time since injury in regions 2 and 3 ($p<0.05$). The R^2 value for the correlation is 0.23 in region 2 and 0.1 in region 3.

6.1.4 Discussion

All contusions showed three pericontusional regions, a contusion core, an area of raised ADC around the core (pericontusional hyperintensity) and a thin hypointense rim. While some contusions showed these regions more clearly than others, this pattern was consistently present.

Imaging techniques often give new insight into pathophysiology of disease; in this case the ADC images may provide new information about the physiology of pericontusional tissues. The regions with low ADC values in the contusion core co-localised with low signal intensity lesions on T2 and T2* weighted images, obtained using FLAIR and GRE sequences, respectively (Figures 47 and 48). This concordance of imaging findings imply that these regions contain haemorrhage, or haemorrhagic contusion, a suggestion which is borne out by operative and post mortem findings.[134] These findings are also concordant with those obtained in the first few hours and days following primary intracerebral haemorrhage, where low ADC values have been attributed to restricted diffusion within the microenvironment of the organised clot.[132 135]

The pericontusional hyperintensity on ADC maps (region 2) and the quantitative measurement of high ADC values in these regions confirms that a dominant cause is the presence of highly diffusible water in vasogenic oedema.

The composition of the hypointense rim surrounding the zone of pericontusional oedema (region 3) is intriguing. The reduced ADC in these areas provides rigorous evidence of a change in diffusion behaviour. In the setting of ischaemic stroke, these low ADC values would be conventionally interpreted as providing evidence of ischaemic cytotoxic oedema, and this may provide one explanation for the finding. However, there is some evidence that extracellular oedema in these settings may have increased tortuousity.[136] This increase in tortuosity, possibly due to alterations in microarchitecture or protein content in the oedema fluid, may lead to reduced diffusion. The correct interpretation of this finding has important pathophysiological implications. If the reduction in ADC represents cytotoxic oedema, as seen after stroke, it would imply that the tissue is under significant ischemic burden. This region may therefore be an ischaemic penumbra after head injury and be an important site of secondary brain injury.

The area of the vasogenic oedema (region 2) showed a significant correlation with the time from injury. The area and ADC values of the hypointense rim also increased with

time since injury, but to a lesser extent. This might imply that the hypointense rim exists at the edge of an expanding region of vasogenic oedema. This hypothesis would imply that ischaemia is a continuing process at the edge of a contusion; a process which continues for some days after injury.

The clinical relevance of these data may be that secondary injury continues for some days after injury. Therefore intensive care treatment of head injuries, particularly those patients in whom the hypointense rim is prominent, may need to be prolonged.

A potential source of bias, when considering the correlations between imaging findings time since injury, is that patients with larger contusions may have been less suitable for MRI scanning at early time points. This important point can only be effectively addressed by imaging the same patient at different time points. These sequential studies are planned.

It is important to emphasise that these findings highlight the issue of ongoing secondary ischaemic damage. The combined volume of the MRI characterised "contusional penumbra" was over three and a half times the volume of the contusion core. The use of ADC map findings may therefore allow us to rationally address the management this tissue.

7 Metabolic Characterisation of ADC Changes

7.1 Metabolic Correlates of DWI change defined by PET

7.1.1 Introduction

While DWI has been widely used in stroke, the metabolic correlates of regions with altered appearances on DWI remain unclear. The early literature suggested that DWI hyperintensity and ADC reductions represented cytotoxic oedema, which was thought to be irreversible. However, more recent reports have shown that such changes can be reversible. These findings suggest that DWI changes, even in the well studied setting of stroke, may reflect metabolically heterogeneous tissue, which may survive an insult or proceed to infarction. The situation in head injury is even less clear, both because of the paucity of literature and the complexity of pathophysiology. It is important to differentiate between these two categories of tissue, since the clinical judgements and scientific conclusions that are made would vary enormously in these two settings. We therefore undertook a comparison of pericontusional ADC changes with metabolic parameters derived from PET. These studies required PET and MRI to happen one after the other in order to minimise the effect of changing pathophysiology.

7.1.2 Methods

Nine patients who were eligible for study underwent imaging as soon as practically possible after injury, allowing for transfer, initial treatment and stabilisation on NCCU, assent from next of kin and scanner availability. Patients initially underwent MRI before being transferred to PET. Every effort made to maintain stable physiology between and during the two scanning procedures. Patient characteristics are shown in table 7.1.

No.	Age (years)	Sex	Mechanism of Injury	Hrs. from injury	GCS	Marshall Score	Apache II Score	ISS
1	39	M	RTA	9	4	DI 2	25	21
2	29	M	Fall	21	10	NEML	20	26
3	17	M	RTA	22	5	DI 3	18	32
4	38	M	RTA	28	8	DI 2	16	10
5	32	M	Assault	121	12	DI 4	5	9
6	38	F	Fall	38	7	DI 4		27
7	30	M	RTA	62	6	DI 3	19	30
8	18	M	RTA	22	9	DI 3	13	14
9	35	M	RTA	22	4	DI 3	23	25

Table 7.1. In all patients ADC map and FLAIR images were acquired and they then immediately underwent ^{15}O-PET scanning. Maps of CBF, CBV, $CMRO_2$, and OEF were constructed from the PET data as described in Section 4.3.

The five regions were outlined on the coregistered ADC map. (FLAIR) These regions were:

Region 1. An area of normal appearing brain away from the contusion.

Region 2. The entire pericontusional region (including core, vasogenic oedema, hypointense rim and a margin approximately 3 mm wide beyond this)

Region 3. The hypointense rim of tissue beyond the vasogenic oedema

Region 4. The vasogenic oedema surrounding the core

Region 5. The contusion core.

An example of these four regions is shown in Figure 50. The regions were then applied to the coregistered PET maps and the mean value of CBF, CBV, OEF and $CMRO_2$ in these regions were calculated for each patient.

7.1.3 Results

Figure 49 shows an example of an ADC map with coregistered CBF and OEF maps from the PET study. Summary data for the metabolic variables calculated are shown (Figures 50 and 51) and listed in Table 7.2 and 7.3. While there were some significant differences in summary data between the different categories of tissue. However, it was noteworthy that there was enormous variability in metabolic characteristics within each physiological tissue compartment, and there was substantial overlap in the range of physiological characteristics of the different compartments defined using ADC maps. In particular CBF, $CMRO_2$,, CBV and OEF in the low ADC region was highly variable and clearly overlapped values seen in the "normal" region and those obtained for mixed grey/white regions of interest (ROI)s from healthy volunteers in our centre.

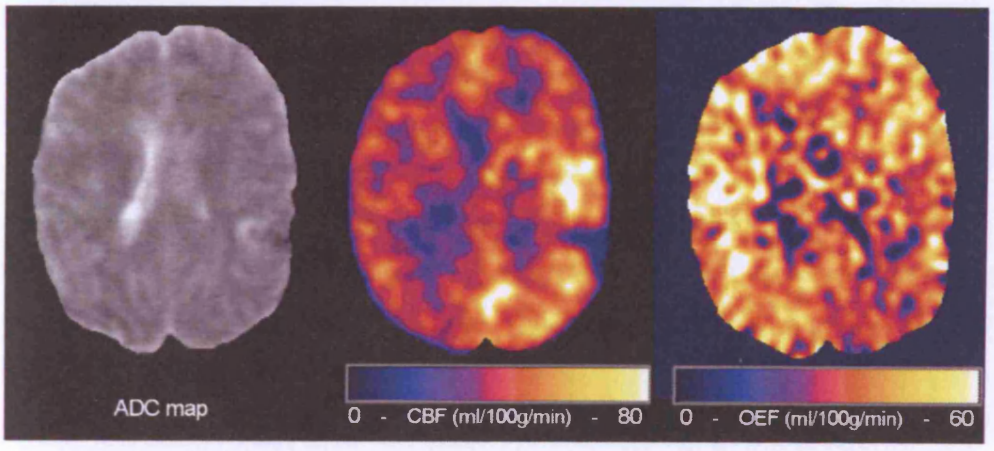

Figure 49. ADC map (left) showing left parietal contusion, CBF map (middle) with colour scale applied and OEF map (right) with colour scale applied. All images are coregistered to FLAIR.

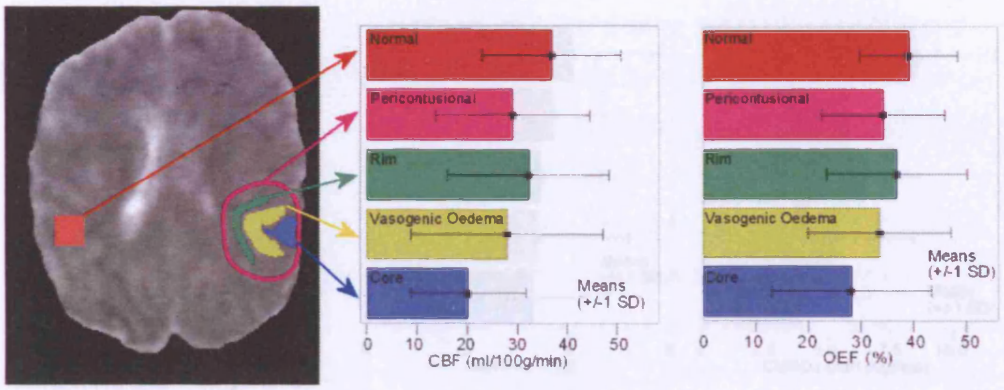

Figure 50. ADC map with examples of the regions of interest (left), bar charts of mean CBF and OEF in these regions (middle and right). Note the ADC map shows an example of the regions in one patient. The bars represent means from regions in all nine patients.

	CBF (SD)	P value	OEF (SD)	P value
Normal	36.9 (13.9)	n/a	39.2 (9.3)	n/a
Pericontusional	29.1 (15.4)	0.277	34.3 (11.8)	0.339
Hypointense Rim	32.3 (16.2)	0.526	36.8 (13.4)	0.662
Vasogenic Oedema	28.0 (19.2)	0.276	33.6 (13.6)	0.318
Core	20.2 (11.4)	0.013*	28.2 (15.2)	0.081

Table 7.2. Mean (SD) values of CBF (ml/100g/min) and OEF (%). Significant differences from mean values in normal tissue ($p<0.05$) are indicated with an asterisk.

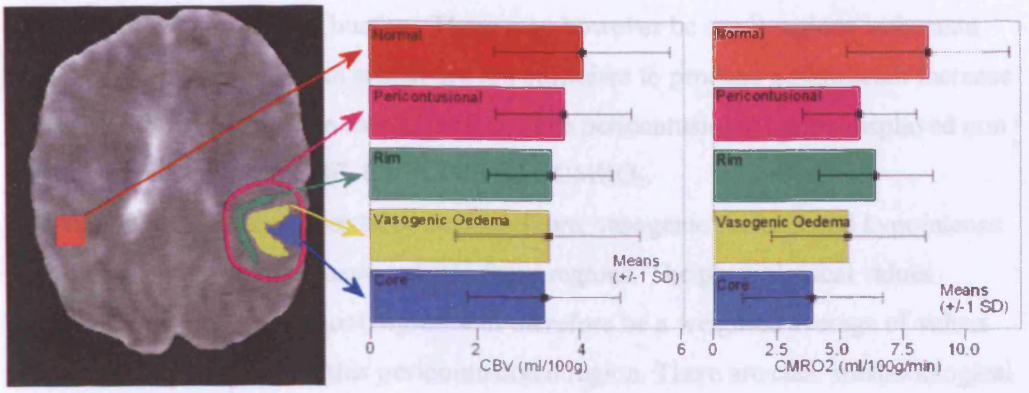

Figure 51. ADC map with examples of the regions of interest (left), bar charts of mean (SD) CBV and CMRO2 in these regions (middle and right). Note the ADC map shows an example of the regions in one patient. The bars represent means from regions in all nine patients.

	CBV (SD)	P value	CMRO2 (SD)	P value
Normal	4.1 (1.7)	n/a	8.5 (3.2)	n/a
Pericontusional	3.7 (1.3)	0.616	5.8 (2.2)	0.055
Hypointense Rim	3.4 (1.2)	0.384	6.4 (2.2)	0.133
Vasogenic Oedema	3.4 (1.8)	0.429	5.3 (3.1)	0.047*
Core	3.3 (1.5)	0.326	3.9 (2.8)	0.005*

Table 7.3. Mean (SD) values of CBV (ml/100g) and $CMRO_2$ (ml/100g/min). Significant differences from mean values in normal tissue ($p<0.05$) are indicated with an asterisk.

7.1.4 Discussion

These results describe the metabolic condition of the pericontusional regions seen on ADC maps. In this sample of nine patients the core region displayed significant reductions in CBF, OEF and $CMRO_2$. This region is likely to represent haematoma or haemorrhagic contusion as discussed in section 6.1.4. These changes in blood flow and metabolism in the core are therefore entirely understandable and the ADC reductions in this region are similar to those seen in intracerebral haematomas.[132 135] The vasogenic oedema displayed reductions in CBF, CBV, OEF and $CMRO_2$; however of these only the $CMRO_2$ was significantly reduced compared to normal tissue. These data suggest that if ischemia is causing a reduction in $CMRO_2$ in these regions it is not accompanied by an increase in OEF. Some studies have suggested microvascular compression as a physiological basis of such ischemia.[8] In this situation the oxygen carried in the arterial blood is prevented from reaching the ischemic tissue by a diffusion barrier. This barrier leads to the oxygen not being extracted from the arterial blood and therefore OEF does not rise. The hypointense rim displayed non significant reductions in CBF, CBV, OEF and $CMRO_2$. These data do not support the view that the tissue in the hypointense rim is

under significant ischaemic burden. There may however be small regions ischaemia within in the hypointense rim which are not sufficient to produce a significant increase in mean OEF or reduction in mean $CMRO_2$. The pericontusional region displayed non significant reductions in CBF, CBV, OEF and $CMRO_2$.

This region contains the other three regions (core, vasogenic oedema and hypointense rim) plus a further area of tissue outside these regions. The physiological values obtained in the pericontusional region will therefore be a weighted average of values from the tissues making up this pericontusional region. There are clear methodological reasons which may explain why the changes in physiology were heterogeneous and failed to reach significance. Firstly it must be acknowledged that the sample size was small and a type II statistical error may be present. Secondly while every effort was made to optimise the coregistration of images from PET and MRI there will always be some inaccuracies. This shortcoming is inevitable to some degree in any inter modality image comparison. Finally the in-plane resolution of PET maps was approximately 6mm and this may have been inadequate to accurately define the physiological values in some of the thin regions of pericontusional ADC change.

However, even accounting for these methodological issues, it appears that there may be significant physiological heterogeneity in tissue with homogeneous ADC characteristics. More specifically, some regions with ADC values which would normally be consistent with ischaemic cytotoxic oedema were associated with relatively normal CBF and $CMRO_2$ and hence have a high probability of containing viable tissue. Similarly some areas of vasogenic oedema contained voxels with $CMRO_2$ values suggestive of critical ischaemia, possibly representing microvascular ischaemia. In any case, these data highlight the need to approach DWI analysis without preconceived ideas based on the findings in ischaemic stroke.

8 Electron Microscopy Correlates

8.1 Introduction

Pericontusional DWI changes may represent BBB breakdown, ischaemia or a combination of such changes. The DWI changes around cerebral contusions which were seen in two small human studies,[10 11] plus the DWI findings around intracerebral haemorrhage[137] suggest that microvascular changes may be responsible for some secondary ischemic damage. Experimental data has shown that the imaging changes on T2 maps can distinguish necrosis and vasogenic oedema and these imaging findings correlate well with the histopathological location of such oedema.[138] We obtained samples of pericontusional tissue on a separate set of seven patients undergoing surgery soon after head injury and concluded that electron microscopic of this tissue may provide information about the origin of the early DWI changes around cerebral contusions head injury. Whilst the imaging finding associated with these tissue samples just prior to excision are unknown the EM images represent an attempt to understand the ultrastructural basis of the MR imaging findings that we observe.

8.1.1 Methods

ELECTRON MICROSCOPY

Pericontusional tissue obtained at the time of surgery for space occupying lesions or refractory intracranial hypertension was fixed in 4% glutaraldehyde in 0.1 M PIPES buffer at pH 7.2, containing 0.3% hydrogen peroxide as an oxygen source to optimize the speed of fixation. After primary fixation for two hours, tissues were osmicated, bulk stained in uranyl acetate, dehydrated in ethanol and embedded in Spurr's epoxy resin. Thin sections were further stained with lead citrate and uranyl acetate and viewed in a Philips CM100 electron microscope (FEI Philips, Eindhoven, Holland) operated at 80 kV. These data represent part of a bank of information used for correlation with imaging findings, and have been used to understand imaging findings in previous positron emission tomography (PET) studies,[9] but have not previously been correlated with MRI. It is important to state that while I was involved in the collection of tissue samples and analysis of the electron microscopy images the electron microscopy was conducted by Dr J. Skepper in the Department of Anatomy in the University of Cambridge.

8.1.2 Results

ELECTRON MICROSCOPY FINDINGS

Two of the seven samples of tissue were unsuitable for analysis after fixation. Tissue from the remaining five patients revealed extensive patchy perivascular oedema, with endothelial swelling resulting in microvascular obliteration. Inspection of electron microscopic images suggested an evolution of changes, as shown in Fig 52. Some samples (as shown in Fig 52a) showed a swollen basal lamina and endothelial swelling, but little overt perivascular oedema. Other samples (Fig 52b) additionally showed vacuolation of the basal lamina, and accumulation of perivascular oedema, which resulted in clefts between the astrocyte foot processes and the basal lamina. Finally, other tissue samples showed more overt vasogenic oedema (as seen in Figs 52c), with complete detachment of astrocyte foot processes from the microvessels. The lumen of many microvessels was obstructed, either due to endothelial swelling, and/or due to microvascular collapse. Adjacent neurons showed morphology of necrosis. These changes were consistent in all subjects, but varied in severity. The severity of ultrastructural abnormality was not related to time after injury.

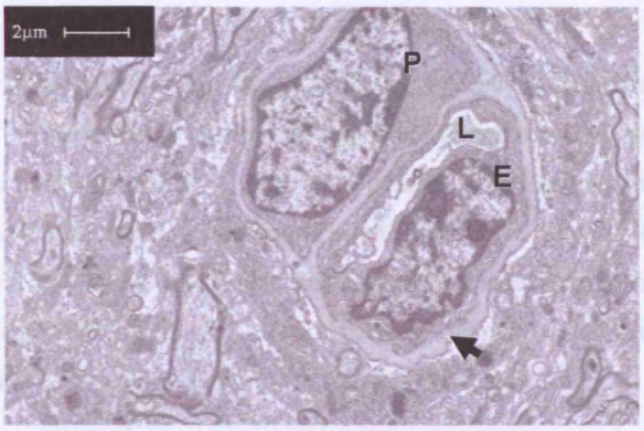

52a

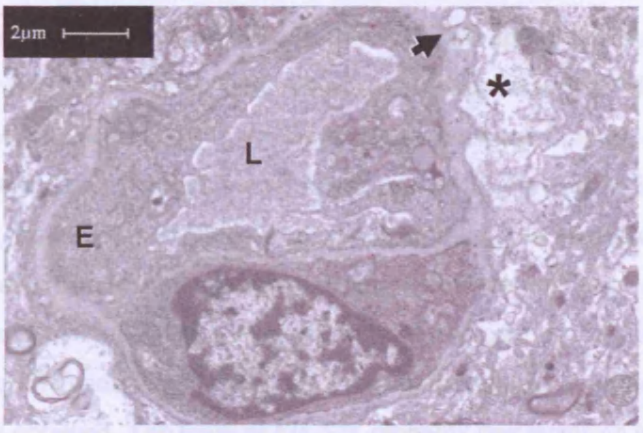

52b

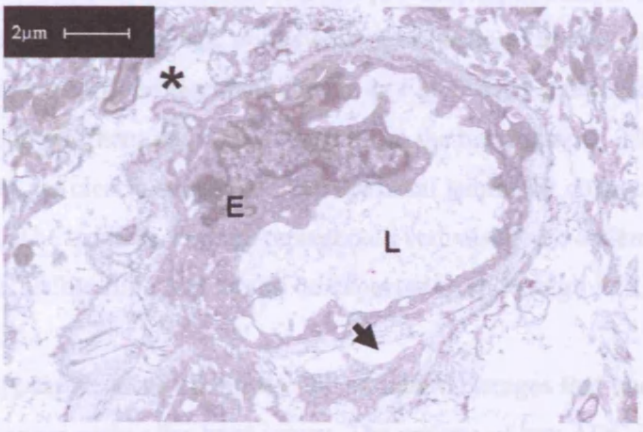

52c

Figure 52. Electron micrographs of pericontusional tissue showing evolution of pathology. Figure 52a shows a microvessel and associated pericyte (P) with a swollen basal lamina (solid arrow) and endothelial cell (E), but little overt perivascular oedema . The tissue in Figure 52b, obtained from a separate patient, additionally shows vacuolation of the basal lamina (solid arrow), and accumulation of perivascular oedema (asterisk). Finally, figure 52c shows a microvessel with large separation of astrocyte foot processes (solid arrow) and, in other places, complete detachment (asterisk) of perivascular structures, from the microvessels. The lumen (L) of microvessels is obstructed, either due to endothelial swelling, debris, and/or due to microvascular collapse.

8.1.3 Discussion

The ultrastructural findings in the tissue are not new but confirm data from other centres.[59 60] However, they provide important insights into the pathophysiology underlying DWI changes. The samples of tissue obtained were exclusively from the margins of contusions at surgery. While the corresponding DWI imaging findings are unknown, it is highly likely that the samples represent tissue that would be included either in the region of high ADC surrounding the contusion core, or the transition from this region to the rim of tissue with low ADC values.

This tissue showed a range of appearances, which do not systematically relate to time after injury. This is not altogether surprising, since lesions are likely to mature at different rates depending on the severity and location of injury, host factors, and the presence or absence of additional physiological insults such as hypoxia and hypotension. Further, the different samples are unlikely to have been obtained from strictly comparable locations in relation to distance from the contusion core, and may represent different phases of injury biology as pathophysiology expands in a dynamic fashion. However, it is possible to construct a plausible temporal sequence of events based on the findings obtained. The brain in Fig 52a probably represents an early phase of the evolution of these findings, with swelling of the basal lamina and endothelial cell, with small amounts of perivascular oedema. In Fig 52b the endothelial swelling remains prominent, but there are visible vacuoles in the basal lamina. The astrocyte foot processes are clearly separated from the basal lamina by collection of perivascular oedema. The tissue in Fig 52c represents overt vasogenic oedema, with large areas of freely diffusible fluid that would be expected to show high ADC values.

These appearances may delineate the structural changes that underpin pericontusional DWI changes early after head injury. The regions of low ADC in the peripheral rim of the lesion may contain tissue similar to that seen in Fig 52a. The increased water content in the swollen basal lamina and the endothelial swelling would represent environments with increased amounts of restricted water. Data obtained using PET and tissue pO_2 monitoring suggests that the microvascular collapse that occurs as a consequence of endothelial swelling and perivascular oedema may cause tissue ischaemia.[9] This may result in an additional cause of cytotoxic oedema in this setting. Further evolution of pathophysiology results in more overt vasogenic oedema (as seen in Figs 4b and 4c), with high ADC values, as seen in the immediate pericontusional region. It is plausible

that vasoactive substances such as thrombin and inflammatory mediators released from the contusion core may provide the biological triggers for this sequence of events.[139 140]

It appears that these regional variations in pathophysiology may provide snapshots of evolving injury in the traumatic penumbra surrounding contusions. However, there are clear limitations to the data. The most significant issue is the inability to robustly correlate imaging appearance with tissue. While there are substantial logistic and methodological difficulties in coregistering biopsy sites and preoperative imaging, this would be essential to conclusively establish the structural basis of imaging findings.

9 DWI for Assessing Therapy

9.1 Introduction

DWI is a widely used technique in acute stroke. This is by virtue of its ability to detect early ischaemic changes. This rapid detection of ischaemia raises the possibility that DWI may be used to investigate the effect of interventions on ischaemia after head injury.

The use of hyperventilation to control raised intracranial pressure is limited by concerns about cerebral vasoconstriction and ischaemia. This has created debate amongst clinicians about the safe use of hyperventilation after head injury as previously discussed in section 3.3. It has been suggested that a reduction in $CMRO_2$ following hyperventilation would provide the strongest evidence of CBF reductions that resulted in critical ischaemia; i.e. of a magnitude that made it impossible to sustain the pre-intervention level of oxygen metabolism. However, this approach is confounded by the finding that, when oxygen delivery is not a limiting factor, reductions in $PaCO_2$ have been shown to increase brain electrical activity and potentially $CMRO_2$. Given the heterogeneity of the CBF changes following head injury, this could mean that when data were averaged over a region, $CMRO_2$ could be decreased, increased or unchanged, even when some parts of the region suffered reductions in $CMRO_2$. However, an increase in the extent (and/or intensity) of restricted diffusion following hyperventilation could provide conclusive evidence of new cytotoxic oedema.
In the context of relatively short imaging sessions (< 2 hours) such changes are only likely to be seen in tissue that is already compromised, and only just maintaining cellular metabolism. Such significantly compromised tissue does exist in the injured brain and data from our research group has previously demonstrated low brain tissue pO_2 levels in regions where OEF is not critically high.[9]

These studies therefore were designed to assess the effect of a short period of hyperventilation on DWI changes in patients with head injury.

9.1.1 Methods

Nine patients underwent two DWI sequences during the same scanning session. The DWI sequences were separated by a mean of 43 minutes during which time the patients were hyperventilated. The hyperventilation was performed to test the experimental hypothesis and not because it was clinically indicated at the time. The hyperventilation produced a fall in mean $PaCO_2$ from 4.81kPa to of 3.55kPa (Table 9.1). A control group of six patients, who had also suffered severe head injury, underwent two DTI sequences

without intervention The scans in the control group of patients were separated by 28 minutes and the mean $PaCO_2$ change was 0.02kPa. The data from this control group were also presented in section 5.2 as part of the test-retest methodological development. Patient details for the two groups are shown in table 9.1. The need to limit imaging times to ~ 1 hour meant that it was impossible to acquire the test retest data as well as perform the hyperventilation intervention within individual patients.

The ADC maps were constructed for each of the two DWI scans in each patients. These ADC maps were coregistered to one another as described in the Image processing section (section 4.4). The change in ADC between the two scans was assessed by subtracting the first ADC map from the second ADC map to create the ΔADC map. (this process is described in more detail in the test-retest section (section 3.3) Regions of interest were developed from the first ADC map. The region were as follows:

Region 1. Whole volume of brain (non-brain structures excluded).

Region 2. Two or three slices which clearly demonstrate the contusion (non-brain structures excluded).

Region 3. The whole pericontusional region on the slice most clearly showing the contusion. This region includes the core, the surrounding oedema and an area of tissue 3-4 mm wide beyond this.

Region 4. The hyperintense vasogenic oedema surrounding the core of the contusion.

Region 5. The hypointense rim of tissue lying just beyond the vasogenic oedema.

Region 6. A normal area of mixed grey and white matter in the contralateral hemisphere (avoiding areas of contusion or ventricles)

The regions are illustrated in figures 53 and 54

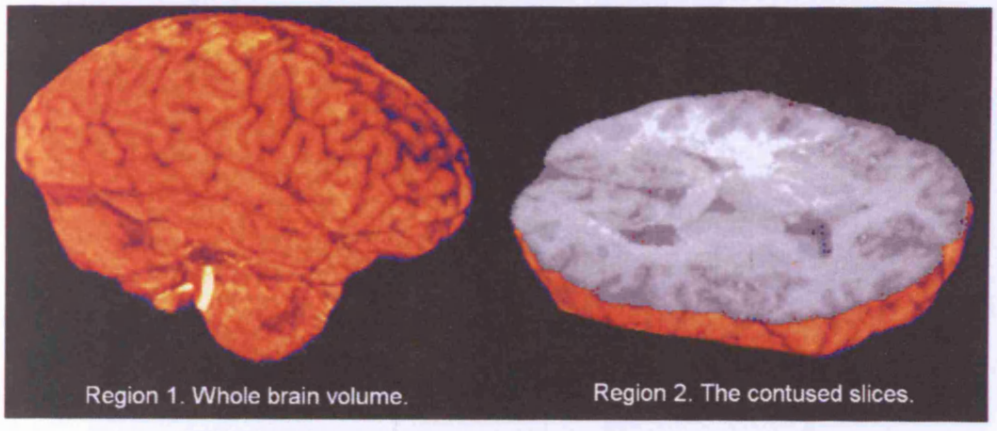

Figure 53. Example of region 1. (left) and region 2. (right)

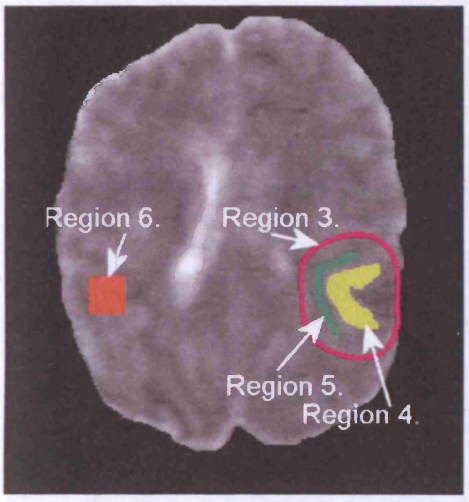

Figure 54. Examples of regions 3, 4, 5 and 6.

These six regions were applied to the ΔADC map for analysis. The overall change was assessed by defining the 50th centile ΔADC in each region. However, it was recognised that hyperventilation might result in changes that affected only a small proportion of voxels, without a significant change in summary values. Consequently, the extreme changes were assessed by defining the 2.5 and 97.5 centiles of ΔADC in each region. The effect of hyperventilation was assessed by comparison of these mean centile thresholds in each of these three categories in the intervention and non-intervention groups.

	Patients	Age (yrs)	Sex	Mechanism of Injury	Hrs. from Injury	GCS	Marshall Score	Apache II Score	ISS	Interscan Interval (min)	CPP (mmHg)	Baseline ICP (mmHg)	ICP Change (mmHg)	Baseline CO_2 (kPa)	CO_2 Change (kPa)
Intervention	1	27	M	RTA	15	3	DI 4	19	27	39	72	19	-1	4.71	-1.25
	2	37	M	Fall	30	3	DI 2	15	25	40	74	18	-2	4.5	-1.24
	3	70	F	Fall	40	8	DI 2	19	16	55	75	16	0	4.72	-1.57
	4	21	F	RTA	46	7	DI 3	14	26	30	80	19	-2	5.03	-1.02
	5	20	M	Assault	57	7	DI 4	11	16	35	67	24	-7	4.39	-1.11
	6	56	M	Fall	59	3	EML	16	29	48	70	18	-1	4.52	-1.38
	7	40	M	RTA	85	3	DI 2	18	38	50	71	21	-3	5.33	-1.16
	8	29	M	RTA	90	5	DI 2	13	50	40	79	9	0	4.39	-1.15
	9	46	M	Fall	134	4	DI 3	20	25	54	76	14	-2	5.71	-1.49
	Mean	38.4			61.7					43.4	73.7	17.5	-2.0	4.81	-1.26
	Median					4		16	26						
Non-Intervention	10	52	F	RTA	8	4	EML	24	49	17	78	7	0	4.21	-0.03
	11	41	F	RTA	27	5	DI 2	19	21	50	70	15	0	4.23	-0.08
	12	19	M	RTA	54	8	EML	19	25	25	70	22	-2	4.57	-0.02
	13	30	M	RTA	62	6	DI 3	19	30	20	78	15	1	4.71	0.11
	14	41	M	Fall	71	6	DI 3	16	43	17	73	26	-1	4.84	-0.05
	15	36	M	RTA	71	8	EML	15	16	39	71	21	2	4.91	-0.06
	Mean	36.50			48.8					28	73.3	17.6	0.0	4.5	0.02
	Median					6		19	27.5	*			*		*
	p-value	0.807			0.465	0.151		0.186	0.812	0.018	0.839	0.969	0.030	0.295	<0.001

Table 9.1. Patient characteristics for the intervention analysis. Marshall score [125] EML: evacuated mass lesion, NEML: non evacuated mass lesion, DI: diffuse injury score. Means and medians shown for the intervention (upper) and non-intervention (lower) groups . Significant differences between the groups are shown by the p-values marked with an asterisk.

9.1.2 Results

Patients in the two groups had similar demographics. However there was a significant difference in the interval from the first to second DWI scans (p=0.018). This interval was significantly shorter in the control group than in the intervention group. The degree of change in CO_2 in the intervention group, while similar in all patients, was not constant, and was not associated with change in ICP. These are difficult factors to control in a clinical study of this kind. The mean $PaCO_2$ changed from 4.81kPa to 3.55kPa, resulting in a significantly greater change (1.26 kPa) than in the control group (0.02 kPa; $p<0.001$). This degree of hyperventilation is similar to that used clinically in some centres. The volume of each region was similar in the two groups.

There was no significant difference in the median ΔADC values between the control and intervention groups in any of the six regions of interest, suggesting that the overall changes in ADC associated with hyperventilation were no more than that attributable to the variability of the technique ($p > 0.05$). Analysis of ΔADC cut off points for the 2.5th and 97.5th centile also showed no significant differences between the control and intervention groups ($p > 0.05$). When data from individual patients were considered, none showed a change in median ΔADC outside the 99% CI for test-retest variability, as defined in section 3.3. However, individual ROIs in some subjects showed changes that fell outside these confidence intervals. While the statistical significance of these individual findings is difficult to interpret, it would appear that some regions (often the hypointense rim) may show further reductions in ADC with hyperventilation (Fig 55)

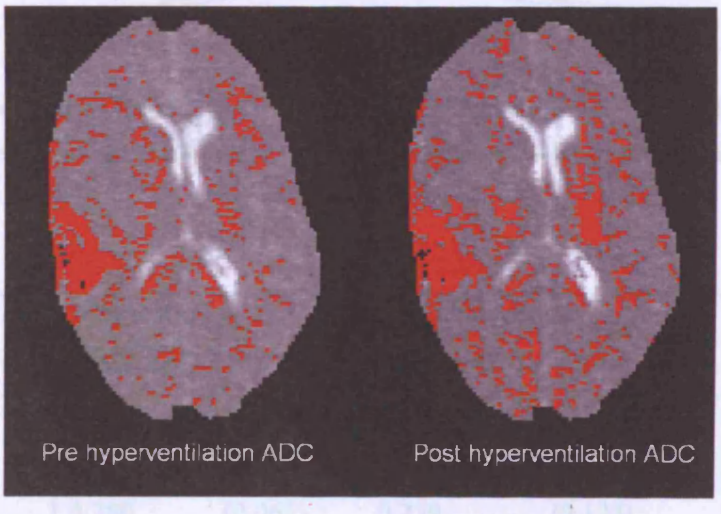

Figure 55. ADC maps pre hyperventilation (left) and post hyperventilation. Voxels with an ADC value below 0.55 x 10^{-3} mm^2/sec are highlighted in red. The post hyperventilation ADC shows an increase in voxels below this threshold both around the contusion and in other diffuse areas.

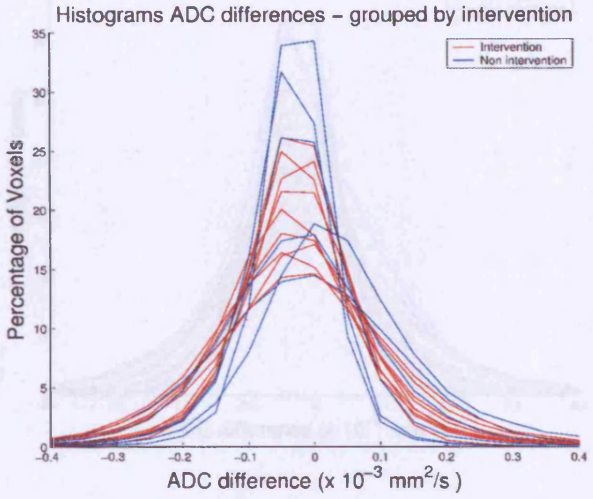

Figure 56a.

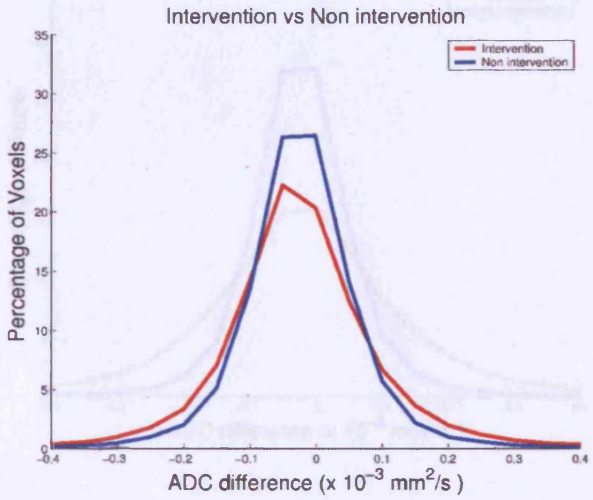

Figure 56. 56a. (upper) individual data, 56b.(lower) grouped data Normalised histograms of ΔADC values from the combined whole brain volume in the intervention and control groups.

ΔADC Centile	Intervention		Non Intervention		p-value
	Mean ΔADC (SD)		Mean ΔADC (SD)		
2.5	-0.266	(0.055)	-0.218	(0.067)	0.157
50	-0.002	(0.009)	0.009	(0.024)	0.409
97.5	0.280	(0.061)	0.239	(0.123)	0.289
Vol (ml)	943.34	(258.87)	993.39	(175.74)	0.81

Table 9.2. ADC changes (mm^2/sec x 10^{-4}) in whole volume of brain following hyperventilation.

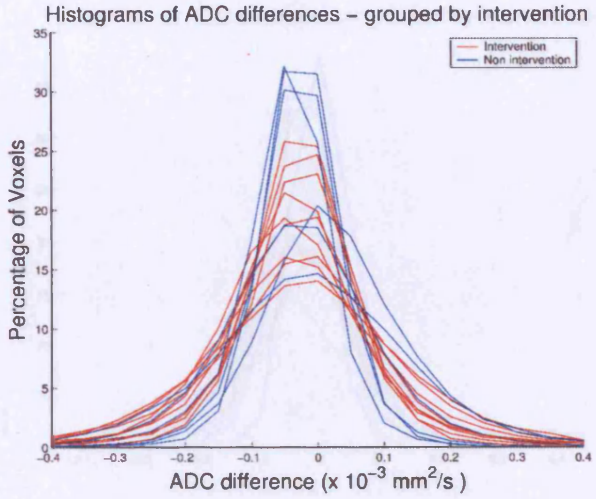

Figure 57a.

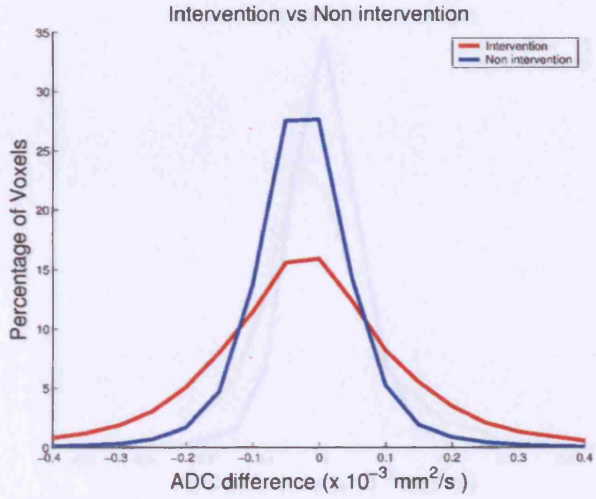

Figure 57b

Figure 57. 57a. (upper) individual data, 57b.(lower) grouped data .Normalised histograms of ΔADC values from the combined axial slices displaying the most obvious contusion for the intervention and control groups. Mean difference non significant (p>0.05).

ΔADC Centile	Intervention Mean ΔADC (SD)		Non Intervention Mean ΔADC (SD)		p-value
2.5	-0.276	(0.067)	-0.206	(0.072)	0.099
50	-0.002	(0.009)	0.006	(0.023)	0.724
97.5	0.289	(0.069)	0.222	(0.113)	0.195
Volume (ml)	210.17	(96.30)	220.54	(61.78)	0.91

Table 9.3. ADC changes (mm^2/sec x 10^{-4}) in the contused slices following hyperventilation.

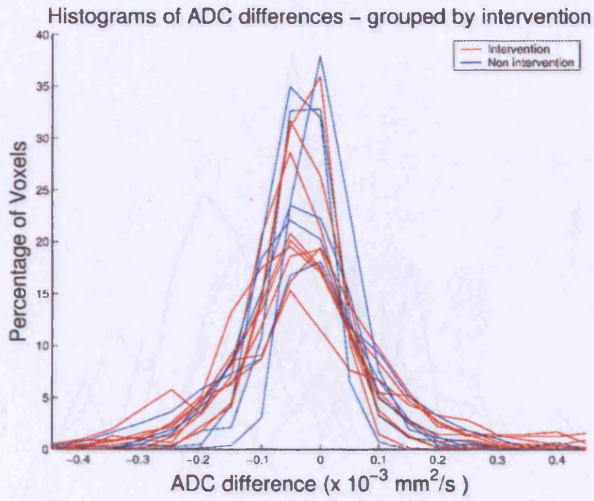

Figure 58a.

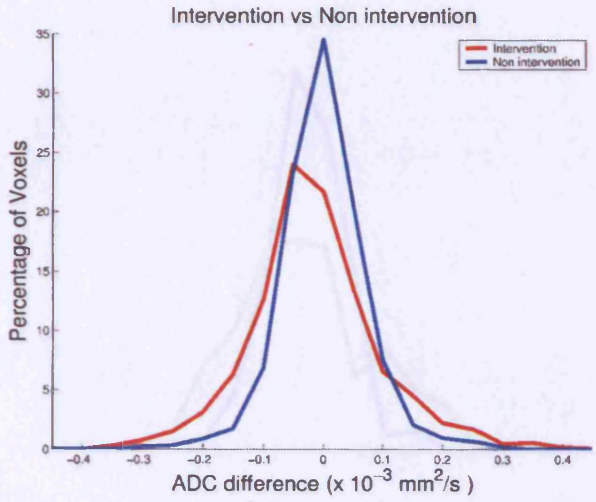

Figure 58b.

Figure 58. 58a. (upper) individual data, 58b.(lower) grouped data. Normalised histograms of ΔADC values from the combined pericontusional regions for the intervention and control groups. Mean difference non significant (p>0.05).

ΔADC Centile	Intervention		Non Intervention		p-value
	Mean ΔADC (SD)		Mean ΔADC (SD)		
2.5	-0.301	(0.164)	-0.183	(0.087)	0.157
50	-0.007	(0.015)	0.000	(0.017)	0.409
97.5	0.318	(0.197)	0.174	(0.071)	0.157
Volume (ml)	6.46	(3.15)	7.10	(2.04)	0.41

Table 9.4. ADC changes (mm^2/sec x 10^{-4}) in the pericontusional region following hyperventilation.

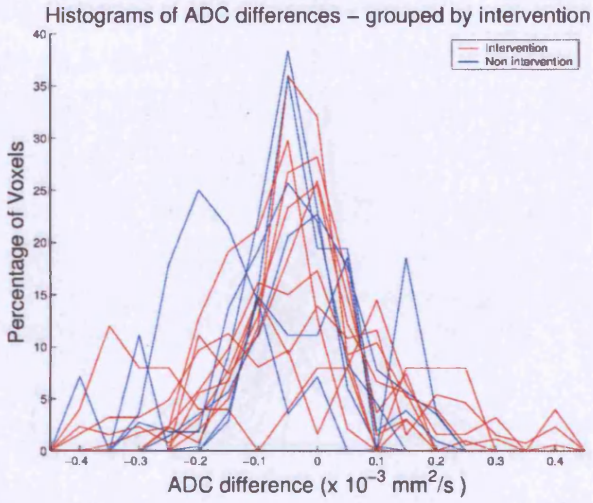

Figure 59a.

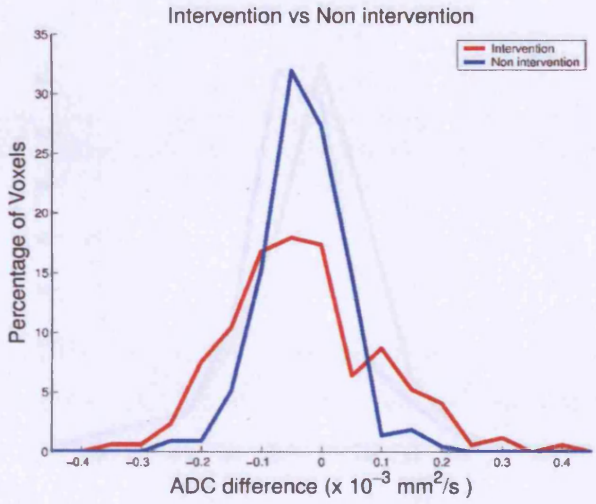

Figure 59b.

Figure 59. 59a. (upper) individual data, 59b.(lower) grouped data. Normalised histograms of ΔADC values from the combined regions of contusional oedema for the intervention and control groups. Mean difference non significant (p>0.05).

ΔADC Centile	Intervention		Non Intervention		p-value
	Mean ΔADC (SD)		Mean ΔADC (SD)		
2.5	-0.358	(0.266)	-0.249	(0.141)	0.409
50	-0.024	(0.046)	-0.030	(0.062)	0.814
97.5	0.280	(0.194)	0.138	(0.074)	0.157
Vol (ml)	0.96	(0.56)	1.15	(0.79)	0.52

Table 9.5. ADC changes (mm^2/sec x 10^{-4}) in vasogenic oedema following hyperventilation.

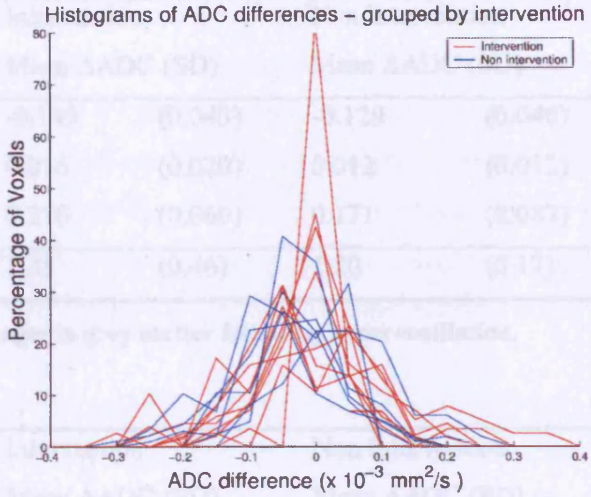

Figure 60a.

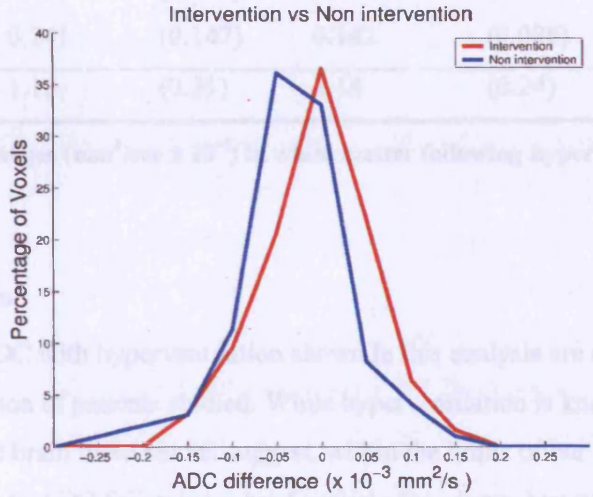

Figure 60b.

Figure 60. 60a. (upper) individual data, 60b.(lower) grouped data. Normalised histograms of ΔADC values from the combined pericontusional hypointense rims for the intervention and control groups. Mean difference non significant (p>0.05).

ΔADC Centile	Intervention		Non Intervention		p-value
	Mean ΔADC (SD)		Mean ΔADC (SD)		
2.5	-4.643	(13.412)	-0.155	(0.062)	0.289
50	3.534	(10.576)	-0.001	(0.038)	0.239
97.5	7.152	(20.681)	0.151	(0.060)	0.195
Vol (ml)	0.50	(0.13)	0.72	(0.32)	0.13

Table 9.6. ADC changes (mm^2/sec x 10^{-4}) in the hypointense rim following hyperventilation.

ΔADC Centile	Intervention		Non Intervention		p-value
	Mean ΔADC (SD)		Mean ΔADC (SD)		
2.5	-0.149	(0.043)	-0.129	(0.046)	0.409
50	0.016	(0.020)	0.012	(0.012)	0.637
97.5	0.210	(0.060)	0.171	(0.087)	0.346
Vol (ml)	1.35	(0.46)	1.20	(0.17)	0.14

Table 9.7.ADC changes in grey matter following hyperventilation.

ΔADC Centile	Intervention		Non Intervention		p-value
	Mean ΔADC (SD)		Mean ΔADC (SD)		
2.5	-0.192	(0.052)	-0.164	(0.074)	0.409
50	0.013	(0.030)	-0.004	(0.020)	0.157
97.5	0.241	(0.147)	0.142	(0.086)	0.126
Vol (ml)	1.18	(0.31)	1.18	(0.24)	1.00

Table 9.8. ADC changes ($mm^2/sec \times 10^{-4}$) in white matter following hyperventilation.

9.1.3 Discussion

The changes in ADC with hyperventilation shown in this analysis are non-significant across the population of patients studied. While hyperventilation is known to reduce CBF in the injured brain these results suggest, within the limits of our sample size, no significant change in ADC following a brief period of moderate hyperventilation across the patient population. It is important to consider whether we may have missed changes either because of our experimental design or analysis techniques.

The centile thresholds used in these analyses were selected prospectively, and showed no overall significant changes. It is possible that significant differences may have been detected if we had selected other centile thresholds, but this would seem unlikely. This type of re-analysis would involve multiple comparisons, increasing the risk of a type 1 statistical error or requiring a compensation for multiple comparisons. Clinical interpretation of a significant difference found by this type of post hoc data dredging would be difficult.

Inspection of the histograms suggests there may be some systematic changes. These changes are best appreciated on the grouped data histograms (for instance figure 57b)

where the intervention group has a greater spread of ΔADC values (both positive and negative changes of ADC). This spread may be due to a lower signal to noise ratio in the data from the intervention group or these findings may represent a real effect of hyperventilation on ADC values. If the effect is due to a real effect of hyperventilation the data suggest that there are both increases and decreases in ADC in the injured brain following hyperventilation. This interpretation would suggest that both cytotoxic and vasogenic oedema increase as a consequence of hyperventilation.

However there maybe some time bias in our data, since the intervention patients were studied before the control group. While the technique was (to the best of our knowledge) constant it is possible that the earlier (intervention) data was, for some reason, more "noisy" than our later (control) data, or some other bias may have occurred over time.

The lack of a significant change in ADC after hyperventilation should not reassure clinicians that hyperventilation is safe. It may be that we did not hyperventilate patients for long enough to induce significant ischaemia. The duration of hyperventilation used in these studies exceeded the 15-20 minute duration of hyperventilation which has been shown to consistently produce significant increases in regional OEF in earlier PET studies from our group. However the duration and degree of hyperventilation may have been too short to produce ischaemia which could be seen as a change in ADC. Clinicians should therefore be cautious about extrapolating our results to support the safety of more prolonged periods of hyperventilation, since ischaemic burden is dependent on both the duration and severity of CBF reduction. It is important to note that other studies from our group have shown that CBF reductions, produced by hypocapnia in head injured patients, do not rapidly normalise and may even worsen over the first hour of hyperventilation. Finally, it must be acknowledged that our sample size was relatively small. The changes that we see in some patients with hyperventilation (Fig 55), while difficult to assess statistically, do not allow us to declare that the intervention is safe in all subjects.

9.1.4 Conclusion

The findings do not suggest that brief periods of hyperventilation after head injury cause ischaemia which is detectable as a change in ADC.
However due to the sample size and short duration of hyperventilation we remain cautious about the safety of hyperventilation. Further, it appears that individual patients can show increases in the volume of brain with low ADC values (suggestive of ischaemia) following hyperventilation (for example see figure 55).

10 Summary and Conclusions

10.1 Chapter Summaries

The data presented in this thesis represent a series of experiments conducted on severely head injured patients. The purpose of these studies was to gain insight into the process of secondary brain injury. However these studies are not easy to conduct; patient safety, coexisting injuries, physiological instability and the heterogeneity of patients are all significant obstacles. Theses obstacles must be either overcome, or at least accommodated, when undertaking such studies and when analysing the results.

In Chapter 3 the sensitivity of the brain to ischaemic injury and the formation of cytotoxic and vasogenic oedema was outlined. The data from experimental imaging studies after head injury have shown that DWI is capable of defining areas of vasogenic and cytotoxic oedema after head injury and that these areas show reduced perfusion. While animal data such as these are important, clinical studies are the only way of answering the question of how oedema and ischaemia interact in humans to produce secondary brain injury. Previous clinical studies after head injury have shown that vasogenic and cytotoxic oedema both occur around contusions, however these studies are small and generally observational. Importantly theses studies have not correlated these MRI findings with physiological evidence of ischaemia such as cerebral blood flow, metabolism and oxygen extraction.

In Chapter 5 methodological issues were examined.
Section 5.1 describes the testing of two infusion pumps in an MR environment as part of the development of the studies. Recommendations are made for the safe use of such equipment.
Section 5.2 reports the first data on the test-retest variability of ADC measurements. These data are important both as a general reference and also to provide a context for assessing the significance of any ADC change following a therapeutic intervention.
Sections 5.3 demonstrates the effect of T2 shine through and T2* shade back on DWI. This underlines the importance of calculating ADC maps from DWI data.
Section 5.4 demonstrates the superiority of ADC maps over FLAIR when defining vasogenic or cytotoxic oedema.

Chapter 6 describes the characteristic pattern of changes around contusions on ADC maps. These changes are corroborated with images obtained using FLAIR and GRE sequences to characterise the nature of the tissue present. The regions that were defined in these studies include a contusion core (with very low ADC values), an area of raised

ADC around the core (pericontusional hyperintensity) and a thin rim of reduced ADC. The imaging findings suggest that the core consists of haemorrhage, or haemorrhagic contusion, and the pericontusional hyperintensity suggests the presence of vasogenic oedema. Inferences regarding the composition of the hypointense rim are more speculative but this region could represent ischaemic cytotoxic oedema and therefore be an important site of secondary injury. The area of the pericontusional hyperintensity showed a positive correlation with time from injury and this may reflect evolution of the secondary injury. The section concludes by making the point that the "contusional penumbra" is over three times larger than the contusion core. This clearly underlines the potential to improve clinical outcome if this penumbral tissue can be salvaged by clinical interventions.

Chapter 7 describes the metabolic correlation of the pericontusional ADC changes. These correlations were made using PET to obtain maps of CBF, OEF and $CMRO_2$ In this sample of nine patients the core region (likely to represent haemorrhage), unsurprisingly displayed significant reductions in CBF, OEF and $CMRO_2$. The vasogenic oedema seen on ADC maps displayed a significant reduction in $CMRO_2$ compared to normal tissue, however CBF and OEF were not significantly reduced. These data suggest that the pericontusional reduction in mean $CMRO_2$ is not accompanied by an increase in mean OEF. This could be interpreted as demonstrating the lack of true ischaemia in these regions. However, microvascular compression may result in ischaemia despite apparently non-ischaemic values of CBF and OEF. This possibility is further discussed in section 8. The hypointense rim and entire pericontusional region displayed non significant reductions in CBF, CBV, OEF and $CMRO_2$. These data do not support the view that these tissue regions as a whole are under a significant ischaemic burden. It is important to remember that regional analysis may overlook very small areas of ischaemia which are not sufficient to produce a significant change in mean OEF or $CMRO_2$ within the entire region. This section also discusses some methodological reasons why changes in physiology may have failed to reach significance.

Chapter 8 describes the EM findings in pericontusional brain tissue both as a correlate and possible explanation of the ADC changes after head injury. The patients had not undergone MRI prior to their surgery and it is therefore unknown what the MRI appearance of this tissue would have been. The samples of tissue were however obtained exclusively from the margins of contusions and are likely to represent tissue from either areas of vasogenic oedema (ADC hyperintensity) or the hypointense rim seen on ADC

maps. The EM images show a range of endothelial swelling and perivascular oedema. These findings are discussed in relation to the MRI and PET data presented previously. The particular the mechanisms by which this microvascular ischaemia may bring about secondary injury are outlined.

Chapter 9 presents the results of experiments investigating the dynamic nature of the pericontusional ADC changes after hyperventilation, a well known therapeutic intervention in head injured patients. Hyperventilation is a double edged sword after head injury, reducing ICP, but also reducing CBF and potentially producing ischaemia. In these experiments $PaCO_2$ was reduced from a mean of 4.8 to 3.5kPa, a significant and clinically relevant reduction. These data showed no significant change in ADC across the study population, following a relatively brief period of hyperventilation, in any of the regions studied. This section discusses the potential reasons why a significant change in ADC after hyperventilation may have gone undetected. It should be concluded that while no significant ADC change could be detected these results do not demonstrate that routine hyperventilation is safe.

10.2 Applicability of the Results to Patient Care

These studies considered the nature of pericontusional brain tissue. The research focused on the imaging findings; in particular the diffusion weighted MRI findings, but also the physiological parameters from PET. Imaging such as this will not be appropriate or available in most head injured patients in the UK for many years however these results allow the clinician to gain some generalisable insights. The volume of the pericontusional tissue has been shown to be large and associated with reduced blood flow and oxygen metabolism in some regions. The pericontusional swelling has been shown to be made of heterogenous regions each likely to be under different pathophysiological conditions

11 Future Directions

11.1 Introduction

This research has highlighted the use of DWI, and particularly ADC map analysis, in the investigation of pericontusional changes after head injury. While this research has attempted to characterise the nature of the ADC changes there are further areas of investigation which are worth considering.

11.1.1 Sequential Imaging Studies

The temporal evolution of the ADC changes after human head injury is unknown. In section 6 the size of some of the pericontusional regions was associated with time from injury. However, since these patients were only imaged once, these associations could be due to a confounding variable or selection bias. Future studies should be undertaken to address the evolution of these changes. Sequential imaging of acute head injuries with DWI would avoid selection bias in the time of imaging. Such studies would address the change in the pericontusional regions over time.

11.1.2 Quantification of CBF & OEF with MRI

MRI techniques such as perfusion weighted imaging with contrast agents and arterial spin labelling[14 141] may allow CBF quantification using MRI. These techniques provide higher resolution than PET but their reliability is still debated.[142] Their higher resolution combined with the ability to obtain intra-modality structural images, DWI and CBF maps would greatly assist the analysis of small regions. The quantification of OEF by MRI has also been reported however it is still a research technique. If OEF could be quantified with MRI, as with CBF, it would significantly assist analysis of regional physiology.

11.1.3 Localisation Of Structural Correlates

The EM images of pericontusional tissue offer a tantalising insight into the nature of ADC changes. However the appearance of this tissue on DWI is not known. The tissue samples are obtained at surgery from tissue which is removed for clinical reasons. The location of these samples on presurgical imaging is therefore unknown. There are likely to be significant logistical problems in accurately determining the location of the samples however this is essential if correlations are to be made between the imaging and EM appearance.

11.1.4 Correlation Of DWI Changes With Clinical Outcome

Although a systematic attempt was made to obtain outcome data in the patients recruited to these studies, the overall numbers of patients was too small to allow useful correlations between the burden of ischaemia (as addressed by ADC restriction) and outcome. The recruitment of larger numbers of patients with early MR and late follow up would provide important information on the clinical significance of the changes that were observed.

11.1.5 Correlation Between Clinical Outcome And Overall Burden Of Axonal Injury

Diffusion weighted MR allows the construction of diffusion tensor images (DTI), which provide an excellent way of detecting and quantifying axonal injury. It would be possible to develop methods of quantifying the overall burden of axonal injury from such images. Correlation of such variables with clinical outcome would help to confirm the widely held view that diffuse axonal injury (rather than focal injury) may be the most important determinant of clinical outcome.

11.1.6 Correlation Of DWI Changes With Local Neuronal Outcome

While ischaemic injury is likely to be an important determinant of outcome, this effect will be substantially modulated by other influences such as age, extracranial injury, and comorbitity. Consequently, the correlations described in 10.1.4 would require relatively large numbers of patients. However, the biological significance of the DWI changes observed could be more easily studied by obtaining a readout of local neuronal survival. Follow up imaging with structural MRI (T2 weighted, FLAIR) shows that much of the high ADC lesion resolves with no residual abnormality. The fate of the low ADC rim remains ambiguous. However, structural MRI cannot detect selective neuronal loss. Techniques such as ^{1}H MR spectroscopy and ^{11}C-flumazenil PET can provide a more direct measure of local neuronal loss. These techniques represent an exciting way of understanding the outcome implications of local DWI changes.

12 Appendix

12.1 Appendix 1

12.1.1 Derivation of The Stejskal-Tanner Equation

Diffusion weighted imaging depends upon the irrecoverable phase shift which occurs with moving spins. The phase shift caused by the application of a gradient field (along direction z in this example can be calculated by Equation 11:

$$\varphi_1 = \gamma \int_0^{\delta} G z_1 dt = \gamma G \delta z_1$$

Equation 11. γ denotes the gyromagnetic ratio, G the gradient strength, δ the gradient duration, $\phi 1$ the phase shift of the spin transverse magnetization, and z1 the spin position in z direction.

After the second pulse z2 is the spin position in direction z. With phase shift ϕ_2 occurring between time Δ and $\Delta+\delta$.

$$\varphi_2 = \gamma \int_{\Delta}^{\Delta+\delta} G z_2 dt = \gamma G \delta z_2$$

Equation 12. γ denotes the gyromagnetic ratio, G the gradient strength, δ the gradient duration, Δ the time interval between the pulses, ϕ_2 the phase shift of the spin transverse magnetization after the second gradient pulse, and z_2 the spin position in z direction

The resulting net dephasing (ϕ_δ) after the paired gradient pulses is therefore calculated by Equation 13:

$$\varphi_\delta = \varphi_2 - \varphi_1 = \gamma G \delta (z_1 - z_2)$$

Equation 13 From Equation 11 and 12. The net dephasing (ϕ_δ) is given by subtracting the phase shift after the second gradient pulse (ϕ_2) from the phase shift after the first gradient pulse (ϕ_1). Since the 180^0 refocusing pulse occurs between these two gradients, for static spins, the net dephasing should be zero (since $z_1 = z_2$). However if the spins have moved (i.e. $z_1 \neq z_2$) a net dephasing will occur.

It can be seen that for static spins, (molecules which do not diffuse) that $z_1=z_2$ and that the net dephasing (ϕ_δ) is therefore zero. For moving spins there is a net dephasing which reduces the transverse magnetization and therefore the signal.

This attenuation of the signal is given by the Stejskal Tanner Equation (Equation 14).

$$S_b = S_0 e^{-\gamma^2 G^2 \delta^2 \Delta D}$$

Equation 14. Where S_b is the signal with the diffusion gradients applied, S_0 the signal without diffusion effect, γ denotes the gyromagnetic ratio, G the gradient strength, δ the gradient duration, Δ the time interval between the pulses, D is the diffusion coefficient (which has dimensions of length^2.time^{-1}, usually given as mm^2/sec).

and since the diffusion can be summarised by a constant (the b value) (Equation 15)

$$b = \gamma^2 G^2 \delta^2 \Delta$$

Equation 15. Where b is a summary constant of the gradient field strength and duration, γ denotes the gyromagnetic ratio, G the gradient strength, δ the gradient duration, Δ the time interval between the pulses

Equation 14. can therefore be simplified to the familiar form of the Stejskal-Tanner (Equation 16).

$$S_b = S_0 e^{-bD}$$

Equation 16. Where S_b is the signal with the diffusion gradients applied, S_0 the signal without diffusion effect, b the constant summarising gradient strength and duration, D is the diffusion coefficient (which has dimensions of length^2.time^{-1}, usually given as mm^2/sec).

12.1.2 The equation for fractional anisotropy

$$FA = \frac{\sqrt{3}}{\sqrt{2}} \frac{\sqrt{(\lambda_1 - \lambda)^2 + (\lambda_2 - \lambda)^2 + (\lambda_3 - \lambda)^2}}{\sqrt{\lambda_1^2 + \lambda_2^2 + \lambda_3^2}}$$

Equation 17. Fractional anisotropy (FA). Where λ1, λ2, λ3 are the first, second and third eigen values and λ is the mean diffusion. An FA of 0 describes isotropy (a spherical tensor) and an FA of 1 would be complete anisotropy (the tensor of FA = 1 would be an infinitely long tube).

12.2 Appendix 2 – Patient Characteristics

The 30 patients who underwent imaging studies were recruited between August 2002 and May 2004. Three patients who were eligible for study were not enrolled because their relatives declined to give assent they were not studied and no data is kept on them. In addition one patient was enrolled but developed severe intracranial hypertension prior to imaging and who died before any studies could be performed. Details of this patient has not been included and no further data was kept on them.

Outcome data for the patients forms part of an ongoing study including, at least in some patients, repeat imaging studies however this data was not part of my work and is not therefore included in this manuscript. Whilst follow up data will be important for interpretation of the initial imaging findings the results of this ongoing study are not yet available.

Table of. patient characteristics for the 30 paients undergoing imaging. Marshall score[125] EML: evacuated mass lesion, NEML: non evacuated mass lesion, DI: diffuse injury score

No.	Age (years)	Sex	Mechanism of Injury	Hrs. from injury	GCS	Marshall Score	Apache II Score	ISS
1	41	M	RTA	17	8	EML	16	25
2	27	M	RTA	56	10	DI 2	13	16
3	56	M	Fall	59	3	DI 3	16	29
4	41	M	Fall	71	6	DI 3	16	43
5	27	M	RTA	15	3	DI 4	19	27
6	21	F	RTA	46	7	DI 2	14	26
7	40	M	RTA	85	3	DI 3	18	38
8	39	M	RTA	9	4	DI 2	25	21
9	31	F	Fall	15	3	DI 2	18	9
10	29	M	Fall	21	10	NEML	20	26
11	27	M	Assault	15	4	NEML	28	27
12	00	M	RTA	71	8	EML	15	16
13	17	M	RTA	22	5	DI 3	18	32
14	22	M	Assault	53	3	DI 2	21	16
15	70	F	Fall	40	8	DI 2	19	16
16	20	M	Assault	57	7	DI 4	11	16
17	38	M	RTA	28	8	DI 2	16	10
18	19	M	RTA	54	8	EML	18	25

19	20	M	Assault	38	7	DI 3	20	16
20	52	F	RTA	8	4	EML	24	49
21	23	M	Assault	104	4	EML	11	26
22	37	M	Fall	30	3	DI 2	15	25
23	46	M	Fall	134	4	DI 3	20	25
24	32	M	Assault	121	12	DI 4	5	9
25	57	M	Fall	42	8	DI 4	18	48
26	38	F	Fall	38	7	DI 4	15	27
27	30	M	RTA	62	6	DI 3	19	30
28	41	F	RTA	27	5	DI 2	19	21
29	18	M	RTA	22	9	DI 3	13	14
30	35	M	RTA	22	4	DI 3	23	25

12.3 Appendix 3 APACHE II and Marshall scores

APACHE II Score

The Acute Physiology And Chronic Health Evaluation II (APACHE II) scoring system is a widely used system for evaluating severity of illness. A higher score has been associated with worse outcome in a wide range of medical and surgical conditions. It takes the worst recorded variables in the first 24 hours of treatment and scores them as follows. The APACHE II score is the sum of points in the following 12 categories

Age in years

under 44 (0 points)

45-54 (2 points)

55-64 (3 points)

65-74 (5 points)

over 74 (6 points)

History of severe organ insufficiency or immunocompromised?

Yes, and non-operative or emergency post-operative patient (5 points)

Yes, and elective post-operative patient (2 points)

No (0 points)

Rectal Temperature (Celsius)

over 40.9 (4 points)

39-40.9 (3 points)

38.5-38.9 (1 points)

36-38.4 (0 points)

34-35.9 (1 points)

32-33.9 (2 points)

30-31.9 (3 points)

below 30 (4 points)

Mean arterial pressure (mmHg)

over 159 (4 points)

130-159 (3 points)

110-129 (2 points)

70-109 (0 points)

50-69 (2 points)

below 50 (4 points)

Heart rate (ventricular response)

over 179 (4 points)

140-179 (3 points)

110-139 (2 points)

70-109 (0 points)

55-69 (2 points)

40-54 (3 points)

below 40 (4 points)

Respiratory Rate (non-ventilated or ventilated)

over 49 (4 points)

35-49 (3 points)

25-34 (1 points)

12-24 (0 points)

10-11 (1 points)

6-9 (2 points)

below 6 (4 points)

Oxygenation (mmHg) (use PaO2 if FiO2 < 50%, otherwise use A-a gradient)

A-a gradient over 499 (4 points)

A-a gradient 350-499 (3 points)

A-a gradient 200-349 (2 points)

A-a below 200(if FiO2 over 49%) or pO2 > than 70 (if FiO2 less than 50%) (0 points)

pO2 = 61-70 (1 points)

pO2 = 55-60 (3 points)

pO2 below 55 (4 points)

Arterial pH

over 7.69 (4 points)

7.60-7.69 (3 points)

7.50-7.59 (1 points)

7.33-7.49 (0 points)

7.25-7.32 (2 points)

7.15-7.24 (3 points)

below 7.15 (4 points)

Serum sodium (mMol/L)

over 179 (4 points)

160-179 (3 points)

155-159 (2 points)

150-154 (1 points)

130-149 (0 points)

120-129 (2 points)

111-119 (3 points)

below 111 (4 points)

Serum potassium (mMol/L)

over 6.9 (4 points)

6-6.9 (3 points)

5.5-5.9 (1 points)

3.5-5.4 (0 points)

3-3.4 (1 points)

2.5-2.9 (2 points)

below 2.5 (4 points)

Serum Creatinine (mg/100 mL)

over 3.4 and ACUTE renal failure (8 points)

2.0-3.4 and ACUTE renal failure (6 points)

over 3.4 and chronic (4 points)

1.5-1.9 and ACUTE renal failure (4 points)

2.0-3.4 and chronic (3 points)

1.5-1.9 and chronic (2 points)

0.6-1.4 (0 points)

below 0.6 (2 points)

Hematocrit (%)

over 59.9 (4 points)

50-59.9 (2 points)

46-49.9 (1 points)

30-45.9 (0 points)

20-29.9 (2 points)

below 20 (4 points)

White blood count (total/cubic mm in 1000's)

over 39.9 (4 points)

20-39.9 (2 points)

15-19.9 (1 points)

3.0-14.9 (0 points)

1.0-2.9 (2 points)

below 1.0 (4 points)

Glasgow Coma Scale Score

Points equal 15 minus the Glasgow Coma Scale Score

Marshall Score (CT criteria)

The Marshall score is used to classify the severity of head injury based on the initial CT findings following head injury.

I: normal head CT scan

II (Diffuse Injury II): lesions, cisterns open, no shift

III (Diffuse Injury III): cisterns effaced, no shift

IV (Diffuse Injury IV): Midline shift >5mm, no clot >25ml

V (EML): Evacuated mass lesion >25ml

VI (NEML): Non-evacuated mass lesion >25ml

VII: lethal head injury

13 References

1. Graham DI, Ford I, Adams JH, Doyle D, Teasdale GM, Lawrence AE, et al. Ischaemic brain damage is still common in fatal non-missile head injury. *J Neurol Neurosurg Psychiatry* 1989;52(3):346-50.

2. Jones PA, Andrews PJ, Midgley S, Anderson SI, Piper IR, Tocher JL, et al. Measuring the burden of secondary insults in head-injured patients during intensive care. *J Neurosurg Anesthesiol* 1994;6(1):4-14.

3. Chesnut RM. Secondary brain insults after head injury: clinical perspectives. *New Horiz* 1995;3(3):366-75.

4. Bouma GJ, Muizelaar JP, Choi SC, Newlon PG, Young HF. Cerebral circulation and metabolism after severe traumatic brain injury: the elusive role of ischemia. *J Neurosurg* 1991;75(5):685-93.

5. Schroder ML, Muizelaar JP, Bullock MR, Salvant JB, Povlishock JT. Focal ischemia due to traumatic contusions documented by stable xenon-CT and ultrastructural studies. *J Neurosurg* 1995;82(6):966-71.

6. von Oettingen G, Bergholt B, Gyldensted C, Astrup J. Blood flow and ischemia within traumatic cerebral contusions. *Neurosurgery* 2002;50(4):781-8; discussion 788-90.

7. Coles JP, Fryer TD, Smielewski P, Chatfield DA, Steiner LA, Johnston AJ, et al. Incidence and mechanisms of cerebral ischemia in early clinical head injury. *J Cereb Blood Flow Metab* 2004;24(2):202-11.

8. Coles JP FT, Gupta AK, Smielewski PS, Matthews JC, Aigbirhio FI, et al. Diffusion limited oxygen delivery following head injury. *J Neurotrauma* 2001;18(10):1186.

9. Menon DK, Coles JP, Gupta AK, Fryer TD, Smielewski P, Chatfield DA, et al. Diffusion limited oxygen delivery following head injury. *Crit Care Med* 2004;*In Press.*

10. Kawamata T, Katayama Y, Aoyama N, Mori T. Heterogeneous mechanisms of early edema formation in cerebral contusion: diffusion MRI and ADC mapping study. *Acta Neurochir Suppl* 2000;76:9-12.

11. Maeda T, Katayama Y, Kawamata T, Koyama S, Sasaki J. Ultra-early study of edema formation in cerebral contusion using diffusion MRI and ADC mapping. *Acta Neurochir Suppl* 2003;86:329-31.

12. Mallett BL, Veall N. Investigation of cerebral blood-flow in hypertension, using radioactive-xenon inhalation and extracranial recording. *Lancet* 1963;1:1081-2.

13. Yonas H, Gur D, Latchaw R, Wolfson SK, Jr. Stable xenon CT/CBF imaging: laboratory and clinical experience. *Adv Tech Stand Neurosurg* 1987;15:3-37.

14. Calamante F, Thomas DL, Pell GS, Wiersma J, Turner R. Measuring cerebral blood flow using magnetic resonance imaging techniques. *J Cereb Blood Flow Metab* 1999;19(7):701-35.

15. Slichter CP. *Principles of magnetic resonance*. 3rd ed. Berlin: Springer-Verlag, 1990:16-17.

16. Stejskal EO, Tanner JE. Spin diffusion measurements: spin echoes in the presence of a time dependent field gradient. *J Chem Physics* 1965;42:288-292.

17. Phelps ME, Huang SC, Hoffman EJ, Kuhl DE. Validation of tomographic measurement of cerebral blood volume with C-11-labeled carboxyhemoglobin. *J Nucl Med* 1979;20(4):328-34.

18. Lammertsma AA, Wise RJ, Heather JD, Gibbs JM, Leenders KL, Frackowiak RS, et al. Correction for the presence of intravascular oxygen-15 in the steady-state technique for measuring regional oxygen extraction ratio in the brain: 2. Results in normal subjects and brain tumour and stroke patients. *J Cereb Blood Flow Metab* 1983;3(4):425-31.

19. Frackowiak RS, Lenzi GL, Jones T, Heather JD. Quantitative measurement of regional cerebral blood flow and oxygen metabolism in man using 15O and positron emission tomography: theory, procedure, and normal values. *J Comput Assist Tomogr* 1980;4(6):727-36.

20. Baron JC, Frackowiak RS, Herholz K, Jones T, Lammertsma AA, Mazoyer B, et al. Use of PET methods for measurement of cerebral energy metabolism and hemodynamics in cerebrovascular disease. *J Cereb Blood Flow Metab* 1989;9(6):723-42.

21. Frackowiak RS, Jones T, Lenzi GL, Heather JD. Regional cerebral oxygen utilization and blood flow in normal man using oxygen-15 and positron emission tomography. *Acta Neurol Scand* 1980;62(6):336-44.

22. Lammertsma AA, Baron JC, Jones T. Correction for intravascular activity in the oxygen-15 steady-state technique is independent of the regional hematocrit. *J Cereb Blood Flow Metab* 1987;7(3):372-4.

23. Erecinska M, Silver IA. ATP and brain function. *J Cereb Blood Flow Metab* 1989;9(1):2-19.

24. Nallet H, MacKenzie ET, Roussel S. The nature of penumbral depolarizations following focal cerebral ischemia in the rat. *Brain Research* 1999;842(1):148-158.

25. Nicholls D, Attwell D. The release and uptake of excitatory amino acids. *Trends Pharmacol Sci* 1990;11(11):462-8.

26. Astrup J, Siesjo BK, Symon L. Thresholds in cerebral ischemia - the ischemic penumbra. *Stroke* 1981;12(6):723-5.

27. Davis SM, Donnan GA. Advances in penumbra imaging with MR. *Cerebrovasc Dis* 2004;17 Suppl 3:23-7.

28. Warach S. Measurement of the ischemic penumbra with MRI: it's about time. *Stroke* 2003;34(10):2533-4.

29. Davis SM, Donnan GA. Ischemic penumbra: MRI or PET. *Stroke* 2003;34(10):2536.

30. Phan TG, Wright PM, Markus R, Howells DW, Davis SM, Donnan GA. Salvaging the ischaemic penumbra: more than just reperfusion? *Clin Exp Pharmacol Physiol* 2002;29(1-2):1-10.

31. Warach S. Tissue viability thresholds in acute stroke: the 4-factor model. *Stroke* 2001;32(11):2460-1.

32. Rohl L, Ostergaard L, Simonsen CZ, Vestergaard-Poulsen P, Andersen G, Sakoh M, et al. Viability thresholds of ischemic penumbra of hyperacute stroke defined by perfusion-weighted MRI and apparent diffusion coefficient. *Stroke* 2001;32(5):1140-6.

33. Ringer TM, Neumann-Haefelin T, Sobel RA, Moseley ME, Yenari MA. Reversal of early diffusion-weighted magnetic resonance imaging abnormalities does not necessarily reflect tissue salvage in experimental cerebral ischemia. *Stroke* 2001;32(10):2362-9.

34. Sharp FR, Lu A, Tang Y, Millhorn DE. Multiple molecular penumbras after focal cerebral ischemia. *J Cereb Blood Flow Metab* 2000;20(7):1011-32.

35. Guadagno JV, Donnan GA, Markus R, Gillard JH, Baron JC. Imaging the ischaemic penumbra. *Curr Opin Neurol* 2004;17(1):61-67.

36. von Kummer R. Effect of training in reading CT scans on patient selection for ECASS II. *Neurology* 1998;51(3 Suppl 3):S50-2.

37. Grotta JC, Chiu D, Lu M, Patel S, Levine SR, Tilley BC, et al. Agreement and variability in the interpretation of early CT changes in stroke patients qualifying for intravenous rtPA therapy. *Stroke* 1999;30(8):1528-33.

38. Wintermark M, Bogousslavsky J. Imaging of acute ischemic brain injury: the return of computed tomography. *Curr Opin Neurol* 2003;16(1):59-63.

39. Wintermark M, Reichhart M, Thiran JP, Maeder P, Chalaron M, Schnyder P, et al. Prognostic accuracy of cerebral blood flow measurement by perfusion computed tomography, at the time of emergency room admission, in acute stroke patients. *Ann Neurol* 2002;51(4):417-32.

40. Heiss WD. Best measure of ischemic penumbra: positron emission tomography. *Stroke* 2003;34(10):2534-5.

41. Kohno K, Hoehn-Berlage M, Mies G, Back T, Hossmann KA. Relationship between diffusion-weighted MR images, cerebral blood flow, and energy state in experimental brain infarction. *Magn Reson Imaging* 1995;13(1):73-80.

42. Busza AL, Allen KL, King MD, van Bruggen N, Williams SR, Gadian DG. Diffusion-weighted imaging studies of cerebral ischemia in gerbils. Potential relevance to energy failure. *Stroke* 1992;23(11):1602-12.

43. Hossmann KA, Fischer M, Bockhorst K, Hoehn-Berlage M. NMR imaging of the apparent diffusion coefficient (ADC) for the evaluation of metabolic suppression and recovery after prolonged cerebral ischemia. *J Cereb Blood Flow Metab* 1994;14(5):723-31.

44. Kidwell CS, Saver JL, Mattiello J, Starkman S, Vinuela F, Duckwiler G, et al. Thrombolytic reversal of acute human cerebral ischemic injury shown by diffusion/perfusion magnetic resonance imaging. *Ann Neurol* 2000;47(4):462-9.

45. Fiehler J, Foth M, Kucinski T, Knab R, von Bezold M, Weiller C, et al. Severe ADC decreases do not predict irreversible tissue damage in humans. *Stroke* 2002;33(1):79-86.

46. Burdette J, Ricci P, Petitti N, Elster A. Cerebral infarction: time course of signal intensity changes on diffusion-weighted MR images. *Am. J. Roentgenol.* 1998;171(3):791-795.

47. Fiebach JB JO, Schellinger PD, Heiland S, Hacke W, Sartor K. Serial analysis of the apparent diffusion coefficient time course in human stroke. *Neuroradiology* 2002;44(4):294-8.

48. Li F, Silva MD, Liu KF, Helmer KG, Omae T, Fenstermacher JD, et al. Secondary decline in apparent diffusion coefficient and neurological outcomes after a short period of focal brain ischemia in rats. *Ann Neurol* 2000;48(2):236-44.

49. Schlaug G, Benfield A, Baird AE, Siewert B, Lovblad KO, Parker RA, et al. The ischemic penumbra: Operationally defined by diffusion and perfusion MRI. *Neurology* 1999;53(7):1528-.

50. Gaetz M. The neurophysiology of brain injury. *Clin Neurophysiol* 2004;115(1):4-18.

51. Bramlett HM, Dietrich WD. Pathophysiology of cerebral ischemia and brain trauma: similarities and differences. *J Cereb Blood Flow Metab* 2004;24(2):133-50.

52. Arundine M, Tymianski M, Bramlett HM, Dietrich WD, Gaetz M, Huisman TA. Molecular mechanisms of glutamate-dependent neurodegeneration in ischemia and traumatic brain injury. *Cell Mol Life Sci* 2004;61(6):657-68.

53. Huisman TA. Diffusion-weighted imaging: basic concepts and application in cerebral stroke and head trauma. *Eur Radiol* 2003;13(10):2283-97. Epub 2003 Mar 6.

54. Nordstrom CH, Reinstrup P, Xu W, Gardenfors A, Ungerstedt U. Assessment of the lower limit for cerebral perfusion pressure in severe head injuries by bedside monitoring of regional energy metabolism. *Anesthesiology* 2003;98(4):809-14.

55. Menon DK. Procrustes, the traumatic penumbra, and perfusion pressure targets in closed head injury. *Anesthesiology* 2003;98(4):805-7.

56. Graham DI, McIntosh TK, Gennarelli TA. Trauma. In: Graham DI, Lantos PL, editors. *Greenfield's Neuropathology*. 7th ed. London: Hodder Arnold, 2002:821-898.

57. Martin NA, Patwardhan RV, Alexander MJ, Africk CZ, Lee JH, Shalmon E, et al. Characterization of cerebral hemodynamic phases following severe head trauma: hypoperfusion, hyperemia, and vasospasm. *J Neurosurg* 1997;87(1):9-19.

58. Bullock R. Injury and cell function. In: Reilly P, Bullock R, editors. *Head Injury*. London: Chapman and Hall Medical, 1997:121-140.

59. Bullock R, Maxwell WL, Graham DI, Teasdale GM, Adams JH. Glial swelling following human cerebral contusion: an ultrastructural study. *J Neurol Neurosurg Psychiatry* 1991;54(5):427-34.

60. Vaz R, Sarmento A, Borges N, Cruz C, Azevedo I. Ultrastructural study of brain microvessels in patients with traumatic cerebral contusions. *Acta Neurochir (Wien)* 1997;139(3):215-20.

61. Bouma GJ, Muizelaar JP, Stringer WA, Choi SC, Fatouros P, Young HF. Ultra-early evaluation of regional cerebral blood flow in severely head-injured patients using xenon-enhanced computerized tomography. *J Neurosurg* 1992;77(3):360-8.

62. McLaughlin MR, Marion DW. Cerebral blood flow and vasoresponsivity within and around cerebral contusions. *J Neurosurg* 1996;85(5):871-6.

63. Hanstock CC, Faden AI, Bendall R, Vink R. Diffusion-Weighted Imaging Differentiates Ischemic Tissue from Traumatized Tissue. *Stroke* 1994;25(4):843-848.

64. Cortez SC, McIntosh TK, Noble LJ. Experimental fluid percussion brain injury: vascular disruption and neuronal and glial alterations. *Brain Res* 1989;482(2):271-82.

65. Barzo P, Marmarou A, Fatouros P, Corwin F, Dunbar J. Magnetic resonance imaging monitored acute blood-brain barrier changes in experimental traumatic brain injury. *Journal of Neurosurgery* 1996;85(6):1113-1121.

66. Barzo P, Marmarou A, Fatouros P, Hayasaki K, Corwin F. Contribution of vasogenic and cellular edema to traumatic brain swelling measured by diffusion-weighted imaging. *J Neurosurg* 1997;87(6):900-7.

67. Ito J, Marmarou A, Barzo P, Fatouros P, Corwin F. Characterization of edema by diffusion-weighted imaging in experimental traumatic brain injury. *Journal of Neurosurgery* 1996;84(1):97-103.

68. Assaf Y, Beit-Yannai E, Shohami E, Berman E, Cohen Y. Diffusion- and T2-weighted MRI of closed-head injury in rats: a time course study and correlation with histology. *Magn Reson Imaging* 1997;15(1):77-85.

69. Assaf Y, Holokovsky A, Berman E, Shapira Y, Shohami E, Cohen Y. Diffusion and perfusion magnetic resonance imaging following closed head injury in rats. *J Neurotrauma* 1999;16(12):1165-76.

70. Albensi BC, Knoblach SM, Chew BG, O'Reilly MP, Faden AI, Pekar JJ. Diffusion and high resolution MRI of traumatic brain injury in rats: time course and correlation with histology. *Exp Neurol* 2000;162(1):61-72.

71. Tsuchida E, Alessandri B, Corwin F, Fatouros P, Bullock R. Detection of ultra-early brain damage after acute subdural hematoma in the rat by magnetic resonance imaging. *J Neurotrauma* 1999;16(7):595-602.

72. Schneider G, Fries P, Wagner-Jochem D, Thome D, Laurer H, Kramann B, et al. Pathophysiological changes after traumatic brain injury: comparison of two experimental animal models by means of MRI. *Magma* 2002;14(3):233-41.

73. Hendrich KS, Kochanek PM, Williams DS, Schiding JK, Marion DW, Ho C. Early perfusion after controlled cortical impact in rats: quantification by arterial spin-labeled MRI and the influence of spin-lattice relaxation time heterogeneity. *Magn Reson Med* 1999;42(4):673-81.

74. Bendszus M, Burger R, Vince GH, Solymosi L. A reproducible model of an epidural mass lesion in rodents. Part II: Characterization by in vivo magnetic resonance imaging. *J Neurosurg* 2002;97(6):1419-23.

75. Kampfl A, Schmutzhard E, Franz G, Pfausler B, Haring HP, Ulmer H, et al. Prediction of recovery from post-traumatic vegetative state with cerebral magnetic-resonance imaging. *Lancet* 1998;351(9118):1763-7.

76. Wieshmann UC. Blunt-head trauma associated with widespread water-diffusion changes. *Lancet* 1999;353(9160):1242.

77. Liu AY, Maldjian JA, Bagley LJ, Sinson GP, Grossman RI. Traumatic Brain Injury: Diffusion-Weighted MR Imaging Findings. *AJNR Am J Neuroradiol* 1999;20(9):1636-1641.

78. Takayama H, Kobayashi M, Sugishita M, Mihara B. Diffusion-weighted imaging demonstrates transient cytotoxic edema involving the corpus callosum in a patient with diffuse brain injury. *Clinical Neurology and Neurosurgery* 2000;102(3):135-139.

79. Rugg-Gunn FJ, Symms MR, Barker GJ, Greenwood R, Duncan JS. Diffusion imaging shows abnormalities after blunt head trauma when conventional magnetic resonance imaging is normal. *J Neurol Neurosurg Psychiatry* 2001;70(4):530-533.

80. Chan JH, Tsui EY, Peh WC, Fong D, Fok KF, Leung KM, et al. Diffuse axonal injury: detection of changes in anisotropy of water diffusion by diffusion-weighted imaging. *Neuroradiology* 2003;45(1):34-8.

81. Arfanakis K, Haughton VM, Carew JD, Rogers BP, Dempsey RJ, Meyerand ME. Diffusion Tensor MR Imaging in Diffuse Axonal Injury. *AJNR Am J Neuroradiol* 2002;23(5):794-802.

82. Hergan K, Schaefer PW, Sorensen AG, Gonzalez RG, Huisman TA. Diffusion-weighted MRI in diffuse axonal injury of the brain. *Eur Radiol* 2002;12(10):2536-41.

83. Kidwell CS, Saver JL, Mattiello J, Warach S, Liebeskind DS, Starkman S, et al. Diffusion-perfusion MR evaluation of perihematomal injury in hyperacute intracerebral hemorrhage. *Neurology* 2001;57(9):1611-7.

84. Huisman TAGM, Sorensen AG, Hergan K, Gonzalez RG, Schaefer PW. Diffusion-Weighted Imaging for the Evaluation of Diffuse Axonal Injury in Closed Head Injury. *Journal of Computer Assisted Tomography January/February* 2003;27(1):5-11.

85. Lin DD, Filippi CG, Steever AB, Zimmerman RD. Detection of intracranial hemorrhage: comparison between gradient-echo images and b(0) images obtained from diffusion-weighted echo-planar sequences. *AJNR Am J Neuroradiol* 2001;22(7):1275-81.

86. Tong KA, Ashwal S, Holshouser BA, Shutter LA, Herigault G, Haacke EM, et al. Hemorrhagic shearing lesions in children and adolescents with posttraumatic diffuse axonal injury: improved detection and initial results. *Radiology* 2003;227(2):332-9.

87. McAllister TW, Sparling MB, Flashman LA, Guerin SJ, Mamourian AC, Saykin AJ. Differential working memory load effects after mild traumatic brain injury. *Neuroimage* 2001;14(5):1004-12.

88. The Brain Trauma Foundation. The American Association of Neurological Surgeons. The Joint Section on Neurotrauma and Critical Care. Trauma systems. *J Neurotrauma* 2000;17(6-7):457-62.

89. Maas AI, Dearden M, Teasdale GM, Braakman R, Cohadon F, Iannotti F, et al. EBIC-guidelines for management of severe head injury in adults. European Brain Injury Consortium. *Acta Neurochir (Wien)* 1997;139(4):286-94.

90. The Brain Trauma Foundation. The American Association of Neurological Surgeons. The Joint Section on Neurotrauma and Critical Care. Indications for intracranial pressure monitoring. *J Neurotrauma* 2000;17(6-7):479-91.

91. Miller JD, Butterworth JF, Gudeman SK, Faulkner JE, Choi SC, Selhorst JB, et al. Further experience in the management of severe head injury. *J Neurosurg* 1981;54(3):289-99.

92. Marshall LF, Smith RW, Shapiro HM. The outcome with aggressive treatment in severe head injuries. Part I: the significance of intracranial pressure monitoring. *J Neurosurg* 1979;50(1):20-5.

93. Robertson CS, Valadka AB, Hannay HJ, Contant CF, Gopinath SP, Cormio M, et al. Prevention of secondary ischemic insults after severe head injury. *Crit Care Med* 1999;27(10):2086-95.

94. Juul N, Morris GF, Marshall SB, Marshall LF. Intracranial hypertension and cerebral perfusion pressure: influence on neurological deterioration and outcome in severe head injury. The Executive Committee of the International Selfotel Trial. *J Neurosurg* 2000;92(1):1-6.

95. The Brain Trauma Foundation. The American Association of Neurological Surgeons. The Joint Section on Neurotrauma and Critical Care. Critical pathway for the treatment of established intracranial hypertension. *J Neurotrauma* 2000;17(6-7):537-8.

96. Update notice, The Brain Trauma Foundation Guidelines for the management of severe traumaticbrain injury: cerebral perfusion pressure, 2003.

97. Madden JA. The effect of carbon dioxide on cerebral arteries. *Pharmacol Ther* 1993;59(2):229-50.

98. The Brain Trauma Foundation. The American Association of Neurological Surgeons. The Joint Section on Neurotrauma and Critical Care. Hyperventilation. *J Neurotrauma* 2000;17(6-7):513-20.

99. Marion DW, Firlik A, McLaughlin MR. Hyperventilation therapy for severe traumatic brain injury. *New Horiz* 1995;3(3):439-47.

100. Yundt KD, Diringer MN. The use of hyperventilation and its impact on cerebral ischemia in the treatment of traumatic brain injury. *Crit Care Clin* 1997;13(1):163-84.

101. Coles JPF, Minhas PSF, Fryer TDP, Smielewski PP, Aigbirihio FP, Donovan TB, et al. Effect of hyperventilation on cerebral blood flow in traumatic head injury: Clinical relevance and monitoring correlates *. *Critical Care Medicine September* 2002;30(9):1950-1959.

102. Marion DW, Darby J, Yonas H. Acute regional cerebral blood flow changes caused by severe head injuries. *J Neurosurg* 1991;74(3):407-14.

103. Marion DW, Puccio A, Wisniewski SR, Kochanek P, Dixon CE, Bullian L, et al. Effect of hyperventilation on extracellular concentrations of glutamate, lactate, pyruvate, and local cerebral blood flow in patients with severe traumatic brain injury. *Crit Care Med* 2002;30(12):2619-25.

104. Muizelaar JP, Marmarou A, Ward JD, Kontos HA, Choi SC, Becker DP, et al. Adverse effects of prolonged hyperventilation in patients with severe head injury: a randomized clinical trial. *J Neurosurg* 1991;75(5):731-9.

105. The Brain Trauma Foundation. The American Association of Neurological Surgeons. The Joint Section on Neurotrauma and Critical Care. Computed tomography scan features. *J Neurotrauma* 2000;17(6-7):597-627.

106. Diringer MN, Videen TO, Yundt K, Zazulia AR, Aiyagari V, Dacey RG, Jr., et al. Regional cerebrovascular and metabolic effects of hyperventilation after severe traumatic brain injury. *J Neurosurg* 2002;96(1):103-8.

107. Diringer MN, Dacey RG, Jr. Traumatic brain injury and hyperventilation. *J Neurosurg* 2002;96(1):155-7.

108. Overgaard J, Tweed WA. Cerebral circulation after head injury. 1. Cerebral blood flow and its regulation after closed head injury with emphasis on clinical correlations. *J Neurosurg* 1974;41(5):531-41.

109. Cold GE, Jensen FT. Cerebral autoregulation in unconscious patients with brain injury. *Acta Anaesthesiol Scand* 1978;22(3):270-80.

110. Czosnyka M, Smielewski P, Kirkpatrick P, Menon DK, Pickard JD. Monitoring of cerebral autoregulation in head-injured patients. *Stroke* 1996;27(10):1829-34.

111. Steiner LA, Czosnyka M. Should we measure cerebral blood flow in head-injured patients? *Br J Neurosurg* 2002;16(5):429-39.

112. Czosnyka M, Smielewski P, Piechnik S, Steiner LA, Pickard JD. Cerebral autoregulation following head injury. *J Neurosurg* 2001;95(5):756-63.

113. Rosner MJ, Rosner SD, Johnson AH. Cerebral perfusion pressure: management protocol and clinical results. *J Neurosurg* 1995;83(6):949-62.

114. Eker C, Asgeirsson B, Grande PO, Schalen W, Nordstrom CH. Improved outcome after severe head injury with a new therapy based on principles for brain volume regulation and preserved microcirculation. *Crit Care Med* 1998;26(11):1881-6.

115. The Brain Trauma Foundation. The American Association of Neurological Surgeons. The Joint Section on Neurotrauma and Critical Care. Guidelines for cerebral perfusion pressure. *J Neurotrauma* 2000;17(6-7):507-11.

116. Asgeirsson B, Grande PO, Nordstrom CH. A new therapy of post-trauma brain oedema based on haemodynamic principles for brain volume regulation. *Intensive Care Med* 1994;20(4):260-7.

117. Menon DK. Cerebral protection in severe brain injury: physiological determinants of outcome and their optimisation. *Br Med Bull* 1999;55(1):226-58.

118. Kinahan PE, Rogers JG. Analytic 3D image reconstruction using all detected events. *IEEE Transactions on Nuclear Science* 1989; vol. 36:964-968.

119. Menon DK, Peden CJ, Hall AS, Sargentoni J, Whitwam JG. Magnetic resonance for the anaesthetist. Part I: Physical principles, applications, safety aspects. *Anaesthesia* 1992;47(3):240-55.

120. Peden CJ, Menon DK, Hall AS, Sargentoni J, Whitwam JG. Magnetic resonance for the anaesthetist. Part II: Anaesthesia and monitoring in MR units. *Anaesthesia* 1992;47(6):508-17.

121. A Primer on Medical Device Interactions with Magnetic Resonance Imaging Systems: Food and Drug Administration, Center for Devices and Radiological Health, 1997.

122. Provision of Anaesthetic Services in Magnetic Resonance Units: The Association of Anaesthetists of Great Britain and Ireland, 2002.

123. Kanal E, Borgstede JP, Barkovich AJ, Bell C, Bradley WG, Felmlee JP, et al. American College of Radiology White Paper on MR Safety. *Am. J. Roentgenol.* 2002;178(6):1335-1347.

124. Williams EJ, Tam YC, Kendall IV, Carpenter TA, Menon DK. Infusion pump performance in an MR environment. *Eur J Anaesthesiol* 1999;16(7):468-72.

125. Marshall LF, Marshall SB, Klauber MR, Clark MV, Eisenberg H, Jane JA, et al. The Diagnosis of Head-Injury Requires a Classification Based on Computed Axial-Tomography. *Journal of Neurotrauma* 1992;9:S287-S292.

126. Lee LJ, Kidwell CS, Alger J, Starkman S, Saver JL. Impact on stroke subtype diagnosis of early diffusion-weighted magnetic resonance imaging and magnetic resonance angiography. *Stroke* 2000;31(5):1081-9.

127. Schaefer PW, Hassankhani A, Putman C, Sorensen AG, Schwamm L, Koroshetz W, et al. Characterization and evolution of diffusion MR imaging abnormalities

in stroke patients undergoing intra-arterial thrombolysis. *AJNR Am J Neuroradiol* 2004;25(6):951-7.

128. Eastwood JD, Engelter ST, MacFall JF, Delong DM, Provenzale JM, Geijer B, et al. Quantitative assessment of the time course of infarct signal intensity on diffusion-weighted images

The value of b required to avoid T2 shine-through from old lucunar infarcts in diffusion-weighted imaging

Acute cerebral infarction: quantification of spin-density and T2 shine-through phenomena on diffusion-weighted MR images. *AJNR Am J Neuroradiol* 2003;24(4):680-7.

129. Geijer B, Sundgren PC, Lindgren A, Brockstedt S, Stahlberg F, Holtas S. The value of b required to avoid T2 shine-through from old lucunar infarcts in diffusion-weighted imaging. *Neuroradiology* 2001;43(7):511-7.

130. Burdette JH, Elster AD, Ricci PE. Acute cerebral infarction: quantification of spin-density and T2 shine-through phenomena on diffusion-weighted MR images. *Radiology* 1999;212(2):333-9.

131. Heiss WD, Graf R, Grond M, Rudolf J. Quantitative neuroimaging for the evaluation of the effect of stroke treatment. *Cerebrovasc Dis* 1998;8 Suppl 2:23-9.

132. Kang BK, Na DG, Ryoo JW, Byun HS, Roh HG, Pyeun YS. Diffusion-weighted MR imaging of intracerebral hemorrhage. *Korean J Radiol* 2001;2(4):183-91.

133. Nitz WR, Reimer P. Contrast mechanisms in MR imaging. *Eur Radiol* 1999;9(6):1032-46.

134. Blumbergs P. Pathology. In: Reilly P, Bullock R, editors. *Head Injury*. London: Chapman & Hall Medical, 1997:39-66.

135. Atlas SW, DuBois P, Singer MB, Lu D. Diffusion measurements in intracranial hematomas: implications for MR imaging of acute stroke. *AJNR Am J Neuroradiol* 2000;21(7):1190-4.

136. Kumura E, Dohmen C, Graf R, Yoshimine T, Heiss WD. Significant shrinkage of extracellular space during global cerebral ischemia: differences in gray and white matter ischemia. *Acta Neurochir Suppl* 2003;86:67-70.

137. Forbes KP, Pipe JG, Heiserman JE. Diffusion-weighted imaging provides support for secondary neuronal damage from intraparenchymal hematoma. *Neuroradiology* 2003;45(6):363-7.

138. Stoffel M, Blau C, Reinl H, Breidt J, Gersonde K, Baethmann A, et al. Identification of Brain Tissue Necrosis by MRI: Validation by Histomorphometry. *J Neurotrauma* 2004;21(6):733-40.

139. Suo Z, Citron BA, Festoff BW. Thrombin: a potential proinflammatory mediator in neurotrauma and neurodegenerative disorders. *Curr Drug Targets Inflamm Allergy* 2004;3(1):105-14.

140. Coughlin SR. Thrombin signalling and protease-activated receptors. *Nature* 2000;407(6801):258-64.

141. Ostergaard L, Smith DF, Vestergaard-Poulsen P, Hansen SB, Gee AD, Gjedde A, et al. Absolute cerebral blood flow and blood volume measured by magnetic resonance imaging bolus tracking: comparison with positron emission tomography values. *J Cereb Blood Flow Metab* 1998;18(4):425-32.

142. Carroll TJ, Teneggi V, Jobin M, Squassante L, Treyer V, Hany TF, et al. Absolute quantification of cerebral blood flow with magnetic resonance, reproducibility of the method, and comparison with H2(15)O positron emission tomography. *J Cereb Blood Flow Metab* 2002;22(9):1149-56.